FRACTURE TOUGHNESS AND CRACK GROWTH BEHAVIOR IN NiTi AND NiTiHf

SHAPE MEMORY ALLOYS

A Dissertation

by

BEHROUZ HAGHGOUYAN

Submitted to the Office of Graduate and Professional Studies of
Texas A&M University
in partial fulfillment of the requirements for the degree of

DOCTOR OF PHILOSOPHY

Chair of Committee,	Dimitris C. Lagoudas
Co-Chair of Committee,	Ibrahim Karaman
Committee Members,	Alan Needleman
	Vikram Kinra
Head of Department,	Ibrahim Karaman

August 2020

Major Subject: Materials Science & Engineering

ABSTRACT

Shape memory alloys (SMAs) are capable of recovering large deformations through martensitic phase transformation, a reversible transformation between austenite and martensite, driven by stress and/or temperature variations. Owing to their superior properties, SMAs like NiTi are increasingly being utilized in various applications where the successful integration of components requires a comprehensive understanding of their crack growth behavior and fracture mechanics. Investigating the fracture of SMAs is often posed with significant challenges because of the transformation-induced complexities in their thermomechanical response. In this study, a new test methodology for measuring the fracture toughness of SMAs using J-integral as the fracture criterion is proposed that accounts for the transformation/reorientation-induced changes in the apparent elastic properties. A comprehensive set of experiments is carried out to measure the fracture toughness of NiTi and NiTiHf SMAs. To investigate different microstructural phases, various testing temperatures are considered: below the martensite finish temperature, M_f; above the martensite start temperature, M_s; and above the austenite finish temperature, A_s. At these temperatures, the material either remains in the martensite state throughout the loading, or transforms from austenite to martensite close to the crack tip, or remains always in the austenite state. Fracture toughness values are obtained and conclusions concerning their temperature dependence are drawn. For NiTi specimens, stable crack growth is observed, and the critical J-values result in extrapolated stress intensity factors that are much higher than the corresponding values reported in literature on the basis of linear elastic fracture mechanics. Unstable crack growth is observed in NiTiHf specimens due to the limited presence of dissipation mechanisms acting near the crack tip. Crack growth under mechanical and actuation loading (thermal cycling under bias load) is investigated via finite element analysis. Crack growth simulations are run in a three-dimensional model in Abaqus finite element suite using the virtual crack closure technique and the experimentally determined fracture toughness values. The numerical results provide a quantitative description of the observed stable crack growth in terms of thermomechanical response and evolution of the

transformation zone. A unified methodology is proposed for fatigue crack growth in SMAs under mechanical and actuation loading paths by employing the range of J-integral as the driving force for crack growth. The methodology is applied to understand the mechanisms contributing to crack growth in the presence of thermal and mechanical induced phase transformation in NiTiHf. The resistance of the material to crack growth is characterized by measuring the crack growth rates corresponding to the range of the applied driving force. The actuation crack growth rates under actuation loading are compared to those of the mechanical crack growth.

DEDICATION

To my father.

ACKNOWLEDGMENTS

I would like to thank my family. I am grateful to my wife, Shahrzad, for her endless love and continuous support throughout my PhD. I am forever indebted to all of the sacrifices that she has made. My gratitude towards my mother and my sister, for their unconditional love and moral support from across the oceans, without which I would not succeed in this endeavor.

Finally, recognition goes to all who directly or indirectly helped me complete my PhD studies, although not mentioned in this brief acknowledgment.

CONTRIBUTORS AND FUNDING SOURCES

Contributors

Funding Sources

NOMENCLATURE

ASTM	American Society for Testing and Materials
CMOD	Crack Mouth Opening Displacement
COD	Crack Opening Displacement
CT	Compact Tension Specimen
DCT	Disk Shaped Compact Tension Specimen
DIC	Digital Image Correlation
DSC	Differential Scanning Calorimetry
EDM	Electrical Discharge Machining
EPFM	Elastic Plastic Fracture Mechanics
FEA	Finite Element Analysis
FOV	Field of View
HTSMA	High Temperature Shape Memory Alloy
LCT	Lower Cycle Temperature
LEFM	Linear Elastic Fracture Mechanics
ROI	Region of Interest
SMA	Shape Memory Alloy
TRIP	Transformation Induced Plasticity
UCT	Upper Cycle Temperature
VCCT	Virtual Crack Closure Technique
a	Crack Size
a_0	Initial Crack Size
A_f	Austenite Finish Temperature

A_f^σ	Austenite Finish Temperature under Applied Stress
A_s	Austenite Start Temperature
A_s^σ	Austenite Start Temperature under Applied Stress
A^{el}	Elastic Components of the Area Under the Load–Displacement Curve
A^{in}	Inelastic Components of the Area Under the Load–Displacement Curve
b	Length of Unbroken Ligament
B	Specimen Thickness
$\mathbf{C}$	Effective Stiffness Tensor
c	Effective Specific Heat Coefficient
C	Elastic Compliance
C	Paris Equation Coefficient
C_A	Stress Influence Coefficient of Austenite
C_M	Stress Influence Coefficient of Martensite
da/dN	Fatigue Crack Growth Rate
$\boldsymbol{e}$	Deviatoric Part of the Strain Tensor
E	Young's Modulus
E_A	Young's Modulus of Austenite
E_M	Young's Modulus of Martensite
f	Hardening Function
f^{fwd}	Hardening Function during Forward Transformation
f^{rev}	Hardening Function during Reverse Transformation
g^t	Transformation Hardening Energy
G	Energy Release Rate
G_I	Mode-I Energy Release Rate

G_{Ic}	Critical Mode-I Energy Release Rate
H^{cur}	Uniaxial Transformation Strain Magnitude for Complete Transformation
H_{sat}	Maximum Transformation Strain
J	J-integral
J_c	Critical J-integral
J_{Ic}	Fracture Toughness
J^{el}	Elastic Component of J-integral
J^{in}	Inelastic Component of J-integral
J_{max}	Maximum J-integral Value
J_{min}	Minimum J-integral Value
k	Control Parameter for Evolving Transformation Strain
K	Stress Intensity Factor
K_c	Critical Stress Intensity Factor
K_{Jc}	Extrapolated Stress Intensity Factor
K_Q	Interim Critical Stress Intensity Factor
M_f	Martensite Finish Temperature
M_f^σ	Martensite Finish Temperature under Applied Stress
M_s	Martensite Start Temperature
M_s^σ	Martensite Start Temperature under Applied Stress
m	Paris Equation Exponent
n_1, n_2, n_3, n_4	Smooth Hardening Parameters
N	Number of Cycles
P	Applied Load
P_{bias}	Applied Bias Load
P_{max}	Maximum Load

P_{min}	Minimum Load
P^i	Nodal Force at the Crack Tip
R	Load Ratio
s_0	Effective Specific Entropy at the Reference State
$\mathbf{S}$	Effective Compliance Tensor
T	Temperature
T_0	Reference Temperature
u_0	Effective Specific Internal Energy at the Reference State
v	Applied Displacement
v^l	Opening Displacement of the Upper Crack Surface
v^{l*}	Opening Displacement of the Lower Crack Surface
W	Specimen Width
Y	Critical Value of the Thermodynamic Force
Y^{fwd}	Critical Value of the Thermodynamic Force to Initiate and Sustain Forward Transformation
Y^{rev}	Critical Value of the Thermodynamic Force to Initiate and Sustain Reverse Transformation
$\boldsymbol{\alpha}$	Effective Thermal Expansion Tensor
α_A	Thermal Expansion Coefficient of Austenite
α_M	Thermal Expansion Coefficient of Martensite
γ^{el}	Elastic Geometry Factor for Crack Growth Correction
γ^{in}	Inelastic Geometry Factor for Crack Growth Correction
δ	Applied Displacement
δ^{el}	Elastic Component of Displacement
δ^{in}	Inelastic Component of Displacement
Δa	Crack Extension

ΔJ	J-integral Range
ΔJ_{th}	Threshold J-integral Range
ΔK	Stress Intensity Factor Range
ΔK_{th}	Threshold Stress Intensity Factor Range
ΔP	Applied Load Range
ΔS	Virtually Closed Crack Tip Area
ε_{eq}	Equivalent Strain
ε_f	Failure Strain
$\boldsymbol{\varepsilon}^t$	Transformation Strain
ε_{xx}	In-Plane Normal Strain in x Direction
ε_{xy}	In-Plane Shear Strain
ε_{yy}	In-Plane Normal Strain in y Direction
η^{el}	Elastic Geometry-Dependent Factor
η^{in}	Inelastic Geometry-Dependent Factor
$\boldsymbol{\Lambda}$	Transformation Tensor
$\boldsymbol{\Lambda}^{fwd}$	Transformation Tensors during Forward Transformation
$\boldsymbol{\Lambda}^{rev}$	Transformation Tensors during Reverse Transformation
ν_A	Poisson's Ratio of Austenite
ν_M	Poisson's Ratio of Martensite
ξ	Martensitic Volume Fraction
π	Thermodynamic Force Conjugated to Martensitic Volume Fraction
π^{fwd}	Thermodynamic Driving Force for Forward Transformation
π^{rev}	Thermodynamic Driving Force for Reverse Transformation
ρ	Mass Density
$\boldsymbol{\sigma}$	Stress Tensor

$\boldsymbol{\sigma}'$	Deviatoric Part of the Stress Tensor
$\bar{\sigma}$	Mises Equivalent Stress
σ^{cr}	Transformation/Detwinning/Yield Stress
σ_f	Detwinning Finish Stress
σ_s	Detwinning Start Stress
σ^{Af}	Reverse Transformation Finish Stress
σ^{As}	Reverse Transformation Start Stress
σ^{Mf}	Forward Transformation Finish Stress
σ^{Ms}	Forward Transformation Start Stress
σ^{TS}	Ultimate Tensile Strength
σ^{Y}	Effective Yield Strength
σ_{zz}	Out-of-Plane Normal Stress
Φ	Transformation Function

TABLE OF CONTENTS

xix

xx

LIST OF TABLES

1. INTRODUCTION

1.1 Shape Memory Alloys

Shape memory alloys (SMAs) are a unique class of active materials that are capable of re-covering large strains by undergoing martensitic phase transformation [1]. This is a first order, reversible, and solid-to-solid transformation with displacive nature between austenite, the high-temperature parent phase, and martensite, the low-temperature product phase [2]. The transfor-mation progresses by the movement of the interface between austenite and martensite, referred to as the habit plane (Figure 1.1). The transformation between austenite and martensite can be trig-gered by applying a sufficient mechanical load (stress-induced transformation), and/or temperature variation (temperature-induced transformation). The transformation from austenite to martensite is called the forward transformation, and the transformation from martensite to austenite is called the reverse transformation. There are four characteristic temperatures associated with the phase transformation. During cooling under zero applied load, the forward transformation begins at the martensitic start temperature, M_s, while it ends at the martensitic finish temperature, M_f. During heating, the reverse transformation starts at the austenitic start temperature, A_s, and finishes at the austenitic finish temperature A_f.

Martensite can exist in two forms: twinned (a.k.a. self-accommodated), and detwinned (a.k.a. reoriented). If the twinned martensite is subjected to sufficiently large mechanical load, detwin-ning process takes place resulting in a shape change and the production of associated transforma-tion strain. The required stress values to initiate and complete the detwinning process are termed the detwinning start stress (σ_s) and detwinning finish stress (σ_f), respectively. When the load is released, the deformed configuration is retained. Heating the material to a temperature above A_f leads to the reverse transformation from detwinned martensite to austenite, and the SMA recovers its original shape. Cooling back to a temperature below M_f results in the forward transformation and the formation of twinned martensite with no macroscopic shape change. This process is called
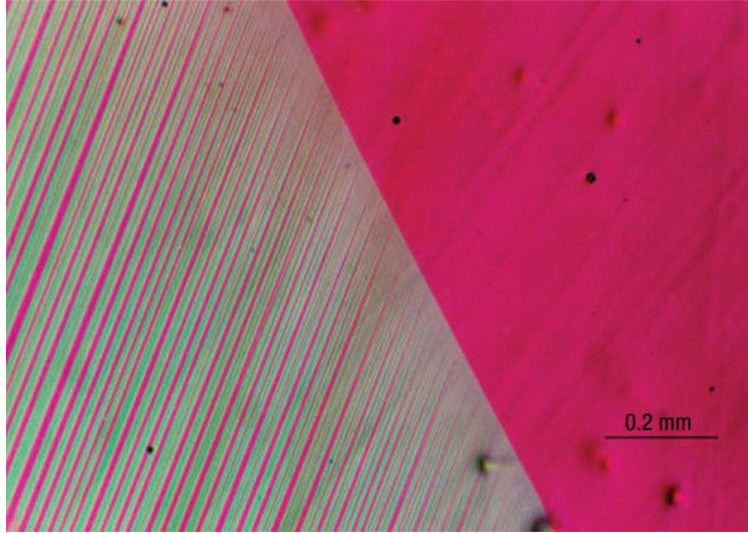
Figure 1.1: Microstructure of twinned martensite meeting a homogeneous region of austenite in a Cu-Al-Ni alloy; after Cui et al. [3].

the *shape memory effect*. If the cooling from austenite to martensite takes place under an applied stress larger than σ_s, the forward transformation leads to the formation of detwinned martensite, generating a shape change. If the applied load is maintained, reheating to austenite leads to shape recovery. Figure 1.2a shows a schematic of the aforementioned loading path, referred to as isobaric or actuation loading path, on a stress-temperature diagram called the *phase diagram*. Note that the transformation temperatures increase with an increase in the applied stress. An example of the corresponding strain-temperature response is given in Figure 1.2b.

As mentioned earlier, martensitic phase transformation can also take place by applying a mechanical load. When the material is in the austenitic phase, a sufficiently high mechanical load can transform austenite to detwinned martensite. The generated shape change during transformation can be recovered by transforming back to austenite upon unloading, if the temperature is above A_f. This process is called the *pseudoelastic effect*. During loading, the stress values at which the forward phase transformation initiates and completes are denoted by σ^{Ms} and σ^{Mf}, respectively. Upon unloading, the stress values at which the reverse phase transformation initiates and

2
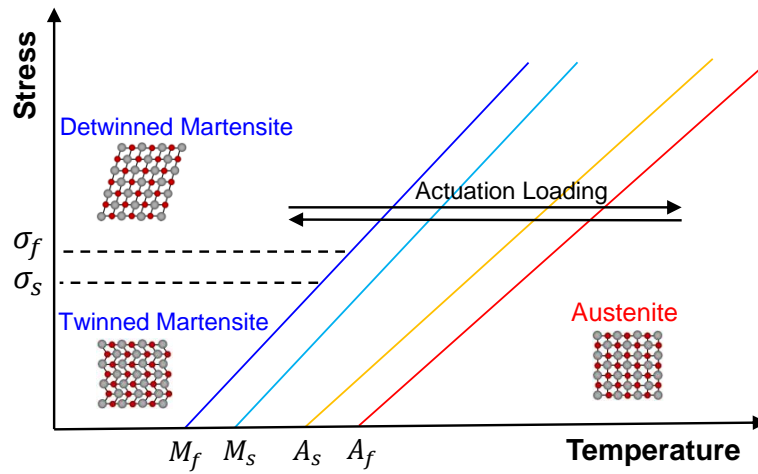
(a)
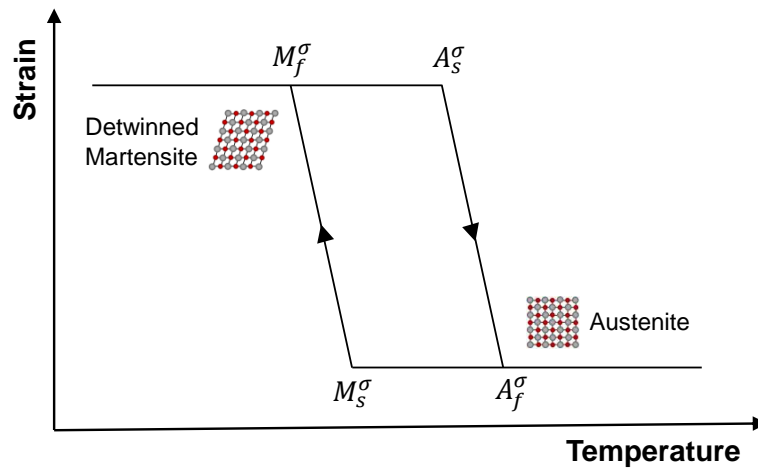
(b)

Figure 1.2: Temperature-induced phase transformation: (a) an actuation loading path represented on stress-temperature phase diagram; (b) schematic of a corresponding strain-temperature response.

completes are denoted by σ^{As} and σ^{Af}, respectively. A schematic of the pseudoelastic loading path, also referred to as isothermal loading path, is demonstrated in Figure 1.3a). Note that the transformation stresses increase with temperature. An example of the corresponding stress-strain response is shown in Figure 1.3b. It is important to note that if the austenitic material is tested below the A_f, but above the M_s, the shape recovery upon unloading either is partial or doesn't occur, depending on wether the temperature is above or below the A_s, respectively. Moreover, if the temperature is above the martensite desist temperature, M_d, no transformation takes place and the austenite behaves like a conventional elastic-plastic material.

Because of these unique characteristics, alongside high energy density [1], superior mechanical properties [4], biocompatibility [5], and corrosion resistance [6], SMAs like nickel-titanium (NiTi) [7] have found applications in various fields such as biomedical [8], civil engineering [9], automotive [10], and aerospace [11]. Driven mainly by the latter, the demand for lighter and stronger solid-state actuators capable of operating in extreme conditions, has led to a recent growth of interest in SMAs. SMA actuators are preferable to conventional actuators (e.g. hydraulic) in aerospace applications where reduction in weight, volume, and complexity is desired. The relatively low transformation temperatures of NiTi SMAs has propelled the discovery of high temperature SMAs (HTSMAs) by alloying of NiTi with ternary elements such as Hf [12], with desired transformation temperature range for such applications. Although the phenomenology of phase transformation and constitutive behavior of SMAs has been studied in extent, there is a lack of knowledge on their failure mechanisms, and specifically their fatigue and fracture behavior. This has hindered the successful integration of SMAs into commercialized applications despite their huge potential. Therefore, fulfilling the necessary reliability and safety requirements in such applications, requires understanding of their crack growth behavior and practice of fracture mechanics concepts under various thermomechanical loadings.

1.2 Literature Review

By expanding the applications of SMAs in various fields beyond the early implementations in biomedical products, investigating their crack growth and fracture response has gained momen-

4
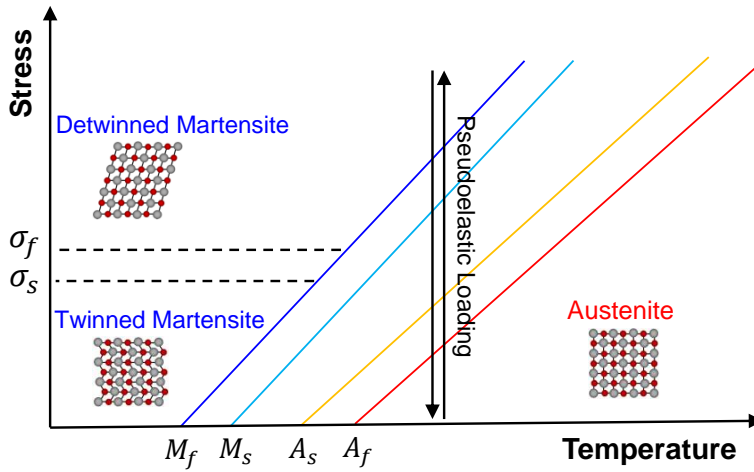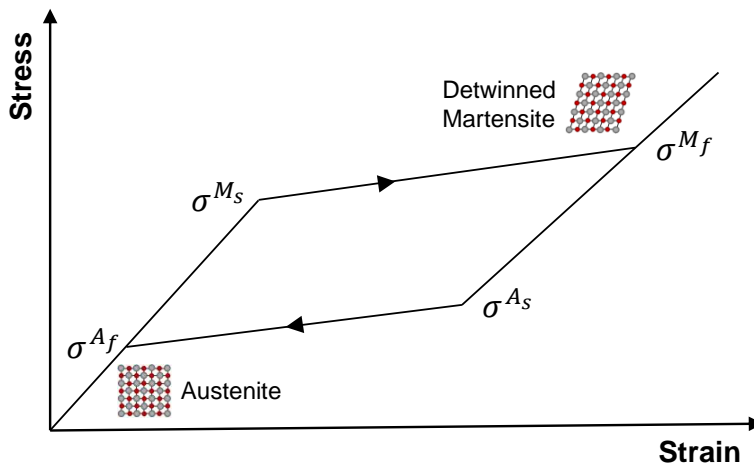
Figure 1.3: Stress-induced phase transformation: (a) a pseudoelastic loading path represented on a stress-temperature phase diagram; (b) schematic of a corresponding stress-strain response.

tum in recent years. In the biomedical applications, the emphasis is placed on preventing crack initiation rather than controlling its growth. Consequently, assessment of properties without the intentional introduction of a flaws is desired. This approach, referred to as total life approach, involves monitoring the lifetime of a defect-free sample as a function of the applied stress or strain. Because these experiments are relatively easy to conduct, the literature is relatively rich. The total life approaches may be sufficient for applications where the products are geometrically small (e.g. stents). However, in actuation, vibration damping and energy absorption applications where the relatively large SMA components can sustain crack growth, the successful implementation of SMA components requires a comprehensive understanding of crack growth behavior (damage tolerance approach).

Although the phenomenology of phase transformation and constitutive behavior of SMAs has been studied extensively, there is a lack of knowledge on their fracture mechanics, perhaps because applying the conventional fracture mechanics theories to SMAs is not straightforward. The fracture behavior of SMAs is relatively complex compared to conventional metals mostly due to the presence of the phase transformation/detwinning zone near the crack tip. The presence of transformation zone has been observed using various experimental techniques such as synchrotron X-ray diffraction [13, 14], IR thermography [15], digital image correlation (DIC) [16], and optical microscopy [17], as shown in Figures 1.4a, 1.4b, 1.4c, and 1.4d, respectively. Figure 1.4a shows phase fractions of the austenite and martensite in a pseudoelastic NiTi CT specimen at a high stress intensity obtained by in situ synchrotron measurements [14]. Figure 1.4b presents the infrared (IR) thermographic image obtained during dynamic loading of a pseudoelastic NiTi CT specimen near the maximum load; the arrows indicate the initial crack tip position prior to crack growth (1), the current crack position (2) and the region ahead of the crack tip (3) [15]. Figure 1.4c, shows the full field normal strains in the vicinity of the crack tip obtained via DIC for $K_I = 44$ MPa$\sqrt{m}$ [16]. Finally, in Figure 1.4d, the progression of transformation during stable crack growth in a single crystal NiTi [100] is presented; the image is taken with a 5x objective at a load level of 548 N, applied in the vertical direction [17]. In addition to the presence of phase

6
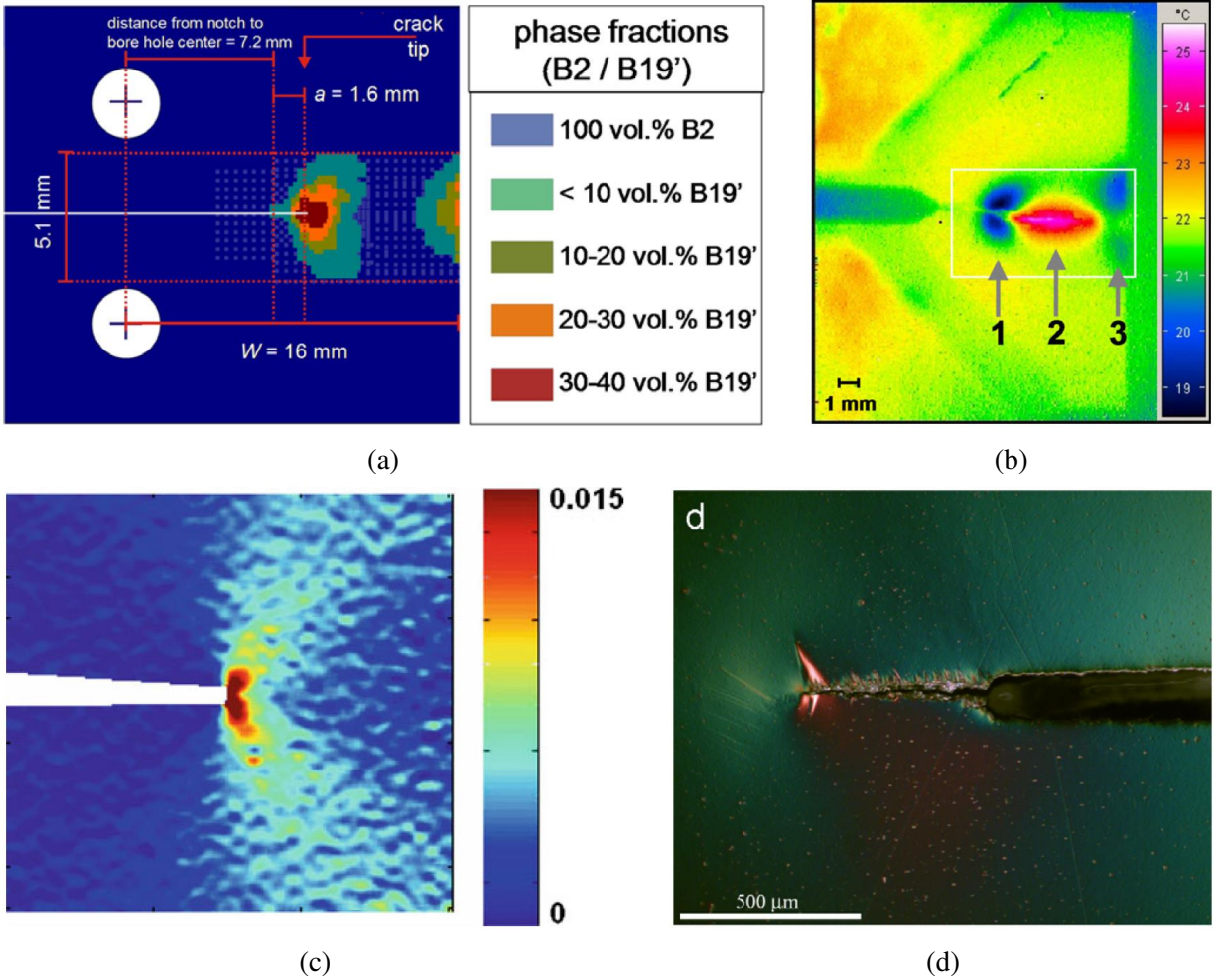
Figure 1.4: Presence of phase transformation zone near the crack tip observed using various experimental techniques: (a) synchrotron X-ray diffraction; after Gollerthan et al. [14], (b) infrared (IR) thermography; after Gollerthan et al. [15], (c) digital image correlation (DIC); after Daly et al. [16], and (d) optical microscopy; after Creuziger et al. [17].

transformation, thermo-mechanical coupling, and the possibility of transformation induced plasticity causes additional complexity [18]. Moreover, the thermomechanical behavior of SMAs is extremely sensitive to chemical composition, processing history, temperature, and adopted loading path. Modifying these variables results in various microstructures and phases, and therefore, a slight change in these variables introduces new challenges into the interpretation of data from an already complicated behavior. Consequently, assessing the crack growth characteristics and fracture properties of SMAs is challenging [19].

Most of the existing studies found in the literature on damage tolerance of SMAs implement conventional fracture mechanics theories, acknowledging that the underlying assumptions for such theories may be violated by the unconventional SMA response. These studies, although limited in their implementation, provide a valuable foundation for understanding crack growth mechanisms. However, understanding fracture in SMAs require more sophisticated methodologies, especially under more complex thermomechanical loading paths. Following section provides a brief review of the existing literature on fracture of SMAs.

1.2.1 Fracture Toughness Measurement

There is a limited number of experimental investigations on the fracture of SMAs, and fracture toughness of the NiTi, the most widely used SMA, has been reported in a few papers [14, 16, 20–27]. Fracture toughness values ranging from 18 to 65 MPa$\sqrt{\text{m}}$ has been reported. As mentioned earlier, the mechanical behavior of SMAs is extremely sensitive to the microstructural phase and hence the temperature. Therefore, understanding the temperature dependence of fracture behavior is of great importance. To address this, the effect of temperature on fracture toughness of NiTi has been investigated in few papers [14, 20, 23–26, 28]. Holtz et al. [20] reported an increase in the fracture toughness of NiTi with temperature in the temperature range M_f–A_f. Gollerthan et al. [14] found similar fracture toughness values for martensitic and pseudoelastic NiTi (31 and 34 MPa$\sqrt{\text{m}}$, respectively), and substantially higher value (53 MPa$\sqrt{\text{m}}$) for stable austenite, i.e. above M_d (Figure 1.5). Maletta et al. [23] reported an increase of the critical stress intensity factor with increasing the testing temperature. Haghgouyan et al. [25] observed that the maximum stress intensity factor of the transforming NiTi is higher than that of the transformation-suppressed material, suggesting transformation toughening. Luo et al. [26] found that above room temperature, NiTi superelastic NiTi showed enhanced ductility with the increase of temperature. There seems to be a lack of consensus over the effect of temperature and phase transformation on fracture properties.

The effect of grain size and mix-mode loading is also investigated. Ahadi et al. [29] studied grain size dependence of fracture toughness and crack-growth resistance of a superelastic NiTi.
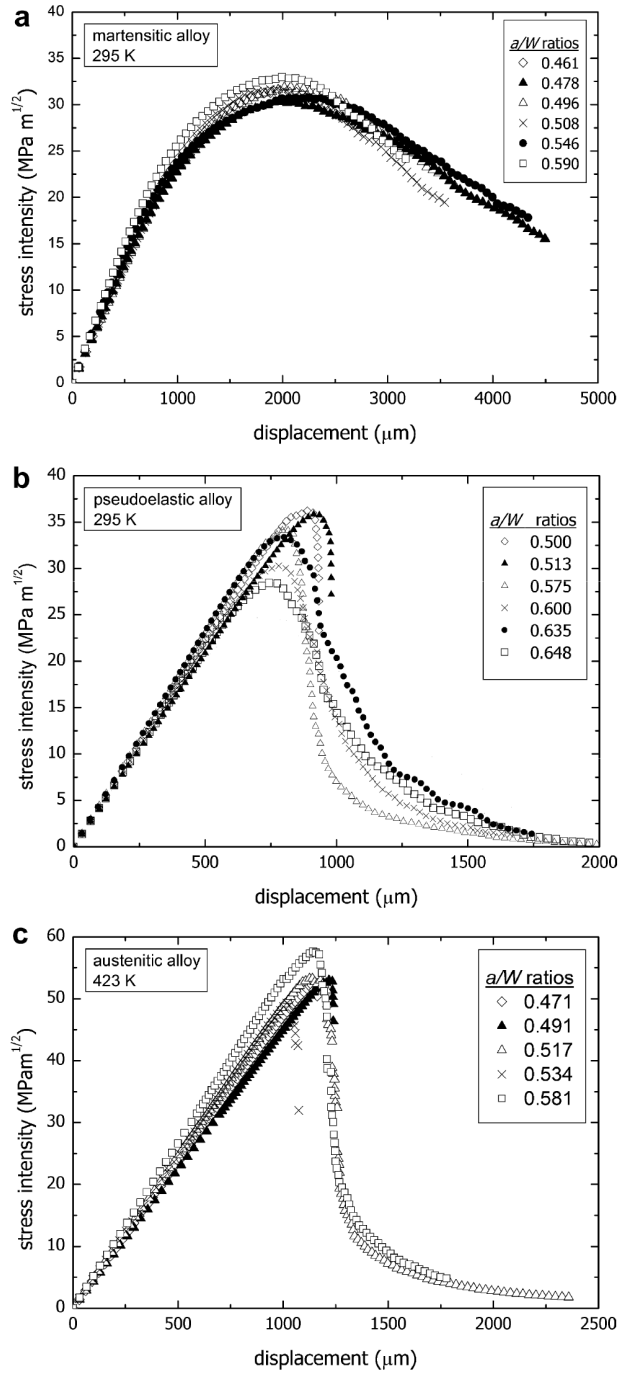
Figure 1.5: Stress intensity (K^*) vs. displacement curves of the (a) martensitic NiTi SMA at 295 K, (b) pseudoelastic NiTi SMA at 295 K and (c) austenitic NiTi SMA at 423 K (temperature above M_d) with varying a/W ratios; after Gollerthan et al. [14].

They reported a monotonic decrease in fracture toughness and crack tip transformation zone by reducing the grain size down to nanoscale. Katanchi et al. [27] investigated the fracture of a superelastic NiTi under mix-mode using butterfly-shaped specimens and specific loading fixture, and measured the fracture toughness for mode-I and mode-II. The fracture toughness values measured were 31.15 MPa$\sqrt{m}$ and 24.67 MPa$\sqrt{m}$ MPa under mode-I and mode-II loading, respectively.

In some of the aforementioned studies, e.g. Ref [28], the fracture toughness was determined from the unstable growth regime of a fatigue crack growth experiment, which is a non-standard method for evaluating fracture toughness values. There have also been efforts [24, 25] to measure the fracture properties of SMAs using the full-field displacement data obtained from DIC. Unlike the standard testing methods which calculate the fracture toughness from load–displacement data, the aforementioned method requires more sophisticated testing setup (imaging equipment) and rigorous post processing of the full-field data. Moreover, the measurements are restricted on the specimen's surface where the level of stress triaxiality is lower than that in the interior. Most of the published fracture toughness data reported in literature for NiTi is measured using ASTM E399 [30] which is established based on the premise of linear elastic fracture mechanics (LEFM).

1.2.2 Fatigue Crack Growth

Most of the studies in literature on fatigue of SMAs have adopted a total life approach. As mentioned earlier, this is because early application of NiTi SMAs was mostly on biomedical devices with geometrically small feature sizes, and therefore the emphasis was placed on preventing crack nucleation rather than controlling its growth. Consequently, fewer studies have been devoted to study fatigue crack growth. The effect of various parameters on crack growth rate and fatigue threshold has been investigated, a brief review of which is presented here.

Melton and Mercier [31] studied crack growth in NiTi with different M_s values, achieved by slight compositional changes. They found no influence of M_s on crack growth rate, and cited the small volume change accompanying the transformation as the possible reason. Holtz et al. [20] investigated fatigue threshold at various temperatures (from room temperature to 150°C with $M_s = 80$°C), and with different load ratios, R (from 0.1 to 0.9). They found that the thresh-

old stress intensity range, ΔK_{th}, increases linearly with temperature, and decreases linearly with R. They also reported the existence of crack closure in the stable martensite regime below 100°C, however, little or no crack closure in the stress-induced martensite regime above 100°C. McKelvey and Ritchie [32] studied the effect of environment on crack growth resistance of a superelastic NiTi by performing experiments in air, aerated deionized water, and aerated Hank's solution. They reported nearly identical crack growth rates and threshold values in all testing environments, suggesting minimal environmentally assisted contributions to crack growth. Compared to other metallic alloys used for implant applications NiTi was found to have lowest fatigue crack growth resistance. In another study [33], McKelvey and Ritchie investigated the effect of loading ratio R on fatigue crack growth rates of a superelastic NiTi at 37°C and found that fatigue thresholds were decreased and growth rates were increased as R raised from 0.1 to 0.7 (Figure 1.6a). They also studied the effect of stress-induced martensitic transformation by characterizing fatigue crack growth at different temperatures: 120°C (stable austenite), 37°C (superelastic austenite), -65°C and -196°C (martensite). In contrast to the findings of Holtz et al. [20], they obtained higher fatigue thresholds and slower growth rates in martensite compared to stable austenite and superelastic austenite. In other words, fatigue crack growth resistance was found to increase with decreasing temperature (Figure 1.6b). Vaidyanathan et al. [28] examined fatigue crack growth characteristics of NiTi reinforced with 10 and 20 vol.% of TiC particles at room temperature. Overall, they found similar crack growth characteristics for the unreinforced and reinforced materials, with a slight increase in the threshold value for the composites. Robertson and Ritchie [21] studied fatigue crack growth behavior of thin-walled superelastic NiTi tube as a function of load ratio and frequency. In agreement to the results by McKelvey and Ritchie [33], increasing growth rates and decreasing fatigue thresholds were obtained with increasing load ratio. Moreover, the crack growth rates at 1 and 50 Hz were found to be identical, suggesting that the crack growth behavior at high frequencies represents a reasonable estimate of the behavior at low frequencies. Gall et al. [34] examined the effect of microstructure on the fatigue of hot-rolled and cold-drawn NiTi. They reported significantly smaller threshold values in cold-drawn material compared to the hot-rolled material. They

11

attributed this difference to the significant residual stresses in the cold-drawn material. The grain size effects on fatigue crack growth of NiTi was studied by Lepage et al. [35] by testing samples with average grain sizes of 10, 18, 42, 80, and 1500 nm. The macroscopic crack growth rates, measured by DIC technique, were related to microscopic crack opening displacement, measured by SEM. The sample with 1500 nm grain size showed the slowest crack growth rate and the largest fatigue threshold value at macroscale, and the smallest crack opening displacements at the microscale. The sample with 80 nm, on the other hand, showed the fastest crack growth rate and the largest crack opening displacements. Sgambitterra et al. [36] studied fatigue crack growth in [0 1 2] NiTi single crystal alloy at two different temperatures: 20°C and 80°C, resulting in stable martensite and stable asutenite phases, respectively. They implemented DIC techniqueto find the effective stress intensity factor. The stable austenite showed a lower threshold value and a higher crack growth rate. In another study [37], they investigated the effect of temperature on fatigue crack growth in a pseudoelastic NiTi. They found that in the pseudoelastic regime, increasing the temperature resulted in higher cycles to failure and lower crack growth rate. Comparison of the proposed DIC regression method with the LEFM solution revealed that while the crack growth curves obtained by LEFM significantly affected by the temperature, those obtained from the regression method was found to be temperature independent.

1.2.3 Crack Growth under Actuation Loading

The literature on fatigue and fracture of SMAs has been almost entirely within the purview of mechanical (isothermal) loading path. It has been observed that SMAs subjected to actuation loading path can fail at load levels much lower than the corresponding isothermal strength of the material. This is of great importance because this loading path is an idealization of typical loading paths these alloys undergo as actuators. There have been only a handful of experimental investigations on thermomechanically-assisted fracture in SMAs.

Baxevanis and Lagoudas [18] observed that a double notched $Ni_{60}Ti_{40}$ (wt%) specimen subjected to thermal actuation failed during cooling and under a constant applied bias tensile load as low as 60% of the failure load. They attributed this behavior to global phase transformation

12
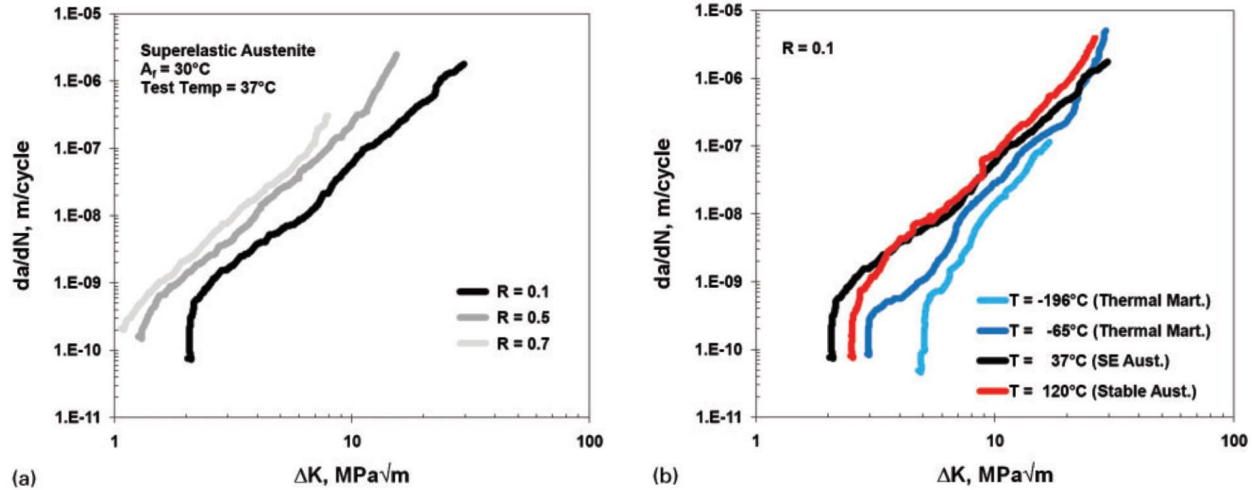
Figure 1.6: Fatigue crack growth rates da/dN as a function of the stress intensity range ΔK in NiTi: (a) the effect of load ratio; and (b) the relative crack growth resistance of the stable austenite, superelastic austenite and thermal martensite; after McKelvey and Ritchie [33].

interacting with the resulting stress field near the notches. As a follow up study, Iliopoulos et al. [38] reported similar observation where double notched NiTi specimens experienced unstable failure within a few thermal cycles under constant load values as low as 50% of the failure load. They also attributed this response to the large scale phase transformation that resulted in stress redistribution, increasing the driving force for crack initiation and abrupt growth. Following these intriguing observations, Hayrettin [39] performed experiments on pre-cracked NiTi CT specimens under actuation loading. Stable crack growth was observed through multiple cycles where the crack advanced during cooling for every thermal cycle and stopped once the phase transformation was completed. Jape et al. [40] explained that the stable crack growth resulted from the shielding effect provided by the transformed material left in the wake of the crack. Figure 1.7 shows the in-plane normal strains, ε_{xx} (top row) and ε_{yy} (bottom row), in the NiTi CT specimen showing stable crack growth during the last thermal cycle before failure at 100°C, 85°C, 70°C, and 35°C obtained using DIC.

Numerical analyses of crack growth in SMAs subjected to actuation loading path have been
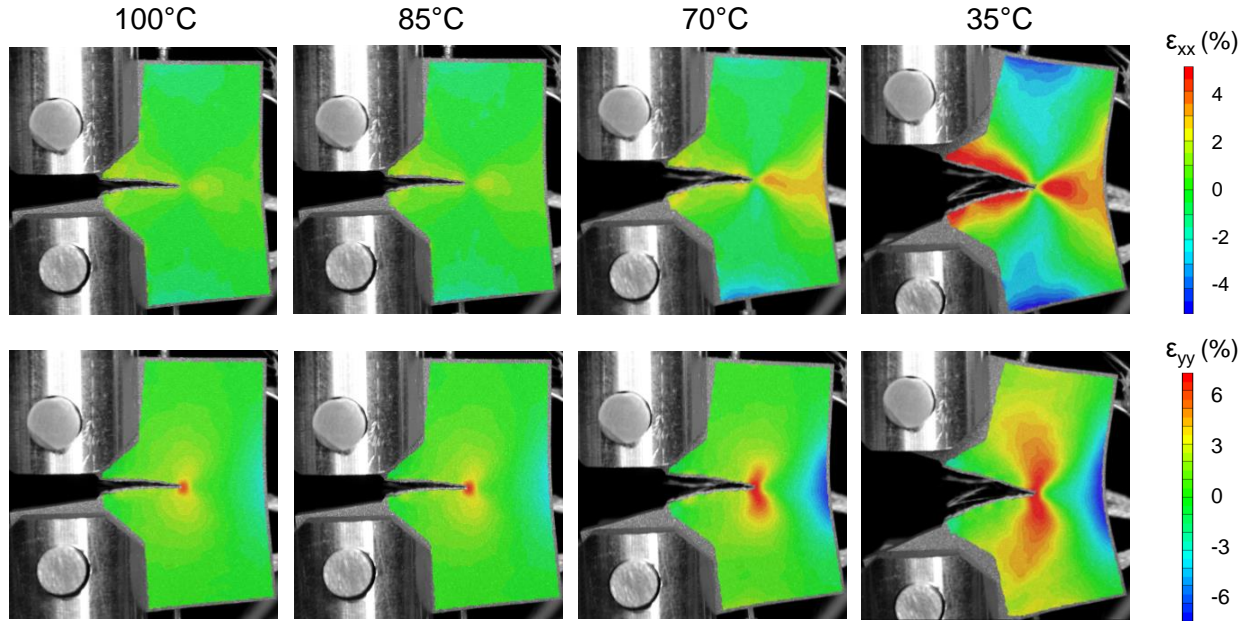
Figure 1.7: In-plane normal strains, ε_{xx} (top row) and ε_{yy} (bottom row), in a compact tension NiTi specimen during the last thermal cycle before failure at 100°C, 85°C, 70°C, and 35°C obtained using DIC.

carried out to unravel some of the factors responsible for this intriguing response which is reviewed in the following section.

1.2.4 Finite Element Analysis of Crack Growth

Most of the theoretical and numerical studies on fracture of SMAs consider static cracks [41–50]. As mentioned earlier, based on experimental observations and numerical calculations [51–53], loading of an SMA specimen with a pre-existing crack results in formation of a transformation/detwinning zone near the crack tip. This zone, acting as a energy dissipation mechanism, can lead to stable crack growth under mechanical or actuation loading [54–58]. Crack growth behavior in SMAs is investigated numerically in a few papers. Stam and van der Giessen [59] investigated the effect of reversible phase transformations on the size and shape of the crack tip transformation zone, and the toughness development during crack growth. Finite element analysis revealed that the phase transformations tend to give rise to a substantial toughening of the material.

14

This increase in toughness, can be significantly reduced by the reversibility of the transformation. Freed and Banks-Sills [60] studied crack growth resistance in SMAs using a cohesive zone model, assuming small scale transformation. It was found that the choice of the cohesive strength has a significant effect on the toughening behavior and that the reversibility of the phase transformation can reduce the toughening. Baxevanis et al. [54] studied stable crack growth in SMAs using virtual crack closure technique (VCCT) and presented the effect of phase transformation on the near-tip mechanical fields. They investigated the dependence of transformation toughening, measured by the ratio of the far-field to the crack-tip energy release rate, to the transformation metrics. It was also found that the dissipation due to plastic deformation during crack propagation is only a small fraction of the dissipation due to the phase transformation. Finite Element Analysis (FEA) of steady-state crack growth in pseudoelastic SMAs have been reported for plane strain, mode-I loading under isothermal [61, 62] and adiabatic [55] conditions. The effect of phase transformation on the mechanical fields near the crack tip for a range of thermomechanical parameters was studied. A substantial fracture toughness enhancement was observed associated with the energy dissipated by the transformed material in the wake of the growing crack. The level of this enhancement was found to be lower under adiabatic conditions than under isothermal conditions. Yan et al. [63] have shown that transformation-induced volume contraction is expected to reduce the fracture toughness enhancement associated with the inelastic deformation processes in SMAs. Ardakani et al. [64] used extended finite element method (XFEM) to study crack growth in SMAs considering thermomechanical coupling. They showed that the near-tip stress field, temperature and size of the phase transformation region depend on the loading rate. Recently, Lu et al. [65] modeled crack propagation in polycrystalline NiTi across scales by combining cohesive zone model and molecular dynamics. The stress intensify factor of compact tension specimens was predicted, establishing a relationship between the microstructure and fracture toughness.

For SMAs subjected to thermal cycling, Xiong and Liu [66] showed that the primary reason for the thermally induced fracture of ferromagnetic SMAs is the increase in the crack tip stress-intensity factor due to stress redistribution around the crack tip as a result of stress-induced marten-

15

sitic transformation. Baxevanis et al. [56] also reported stress redistribution induced by large scale phase transformation during thermal variations under mechanical load that increases the energy release rate substantially which may result in crack propagation when the crack-tip energy release rate reaches a critical value. Figure 1.8 plots the normalized energy release rate, G_I/G_∞, versus normalized temperature $C_M(T - M_s)/\sigma_\infty$ during an actuation cycle, and shows martensite volume fraction ξ at the beginning and end of cooling. Following this, Jape et al. [57] observed stable crack extension through multiple cycles when the applied mechanical load is sufficiently low so that the resultant crack-tip energy release rate is less than the critical value but sufficiently high so that during the first thermal cycle the critical value is reached. It was found that for smaller the applied bias loads more thermal cycles are required for the crack to attain steady-state condition. The authors also investigated the effect of transformation-induced plasticity (TRIP) and found that accumulation of TRIP strains over the cycles results in higher energy release rates and magnitude of the TRIP strains has a dual effect on crack growth response: larger TRIP strains lead to triggering of crack growth at higher temperatures (earlier during actuation cycles) but also results in larger toughening effect during stable crack growth [58].

1.3   Significance of the Research

The reported data for the fracture toughness of SMAs has been entirely based on LEFM. Most of the tests, however, do not comply with the small-scale yielding assumption which is a prerequisite for the validity of LEFM. The small-scale yielding condition requires the zone of non-linear deformation close to the crack tip, regardless of the mechanism, to be just a small fraction of the characteristic dimensions of the specimen. Performing LEFM analysis to study the fracture of a material and assuming that it is valid could be risky. LEFM gives no indication when it becomes invalid, and therefore the user must be cautious to consider the nonlinear effects that might be involved. A more rigorous methodology is proposed in this study that spans a wider range of materials and can be applied to various fracture behavior is necessary. Such analysis would simplify to LEFM for a brittle material, while taking into account the nonlinear effects for ductile behavior. This is of great importance in SMAs where the material response is extremely sensitive to the small
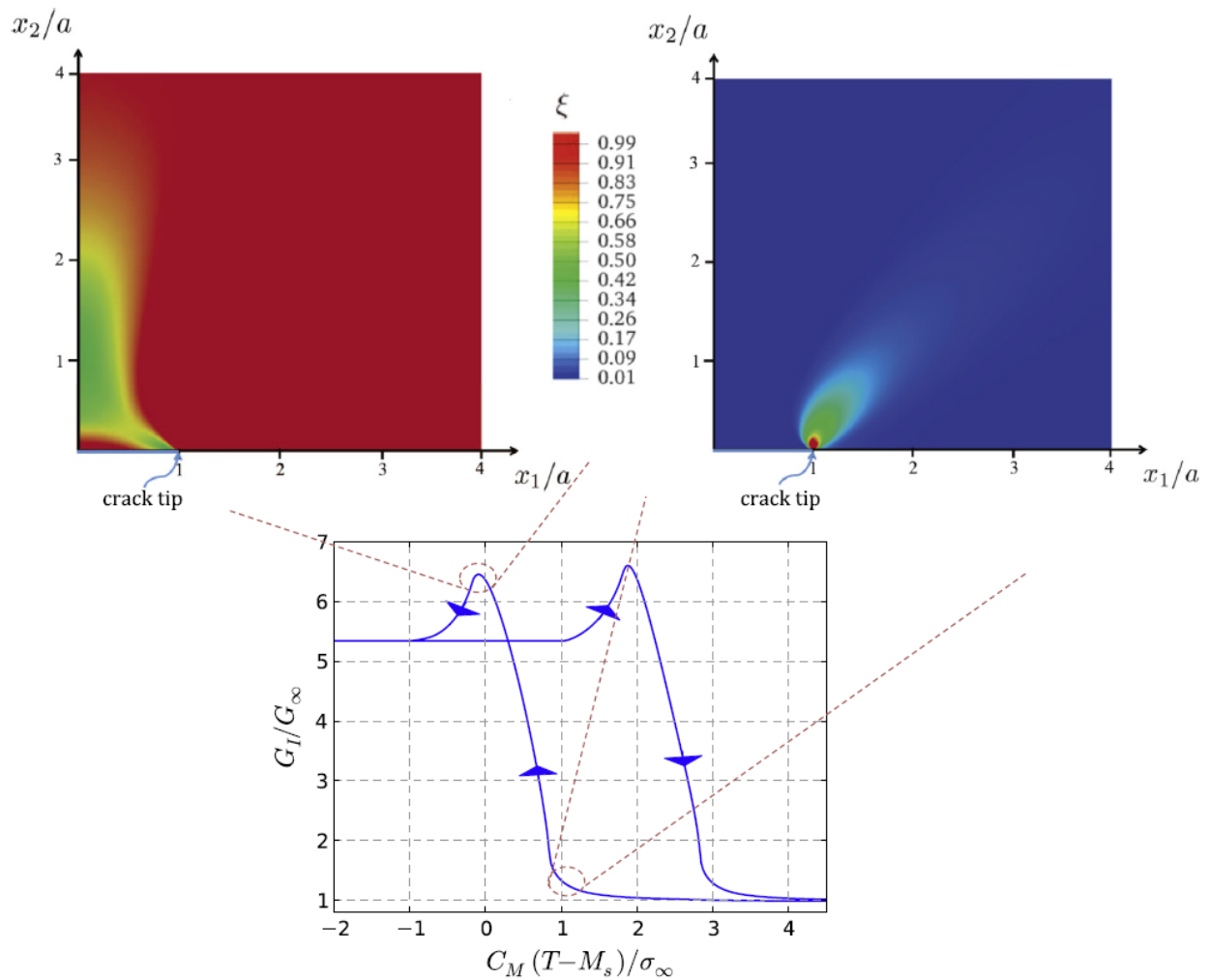
Figure 1.8: Normalized energy release rate, G_I/G_∞, versus normalized temperature $C_M(T - M_s)/\sigma_\infty$ during an actuation cycle, and martensite volume fraction ξ at the beginning and end of cooling; after Baxevanis et al. [56].

changes in the composition, processing history, and service condition. Another advantage of the proposed methodology is the attempt to circumvent the difficulties associated with elastic modulus determination, which in SMAs adopts different values for different phases.

From the modeling aspect, most of the studies on numerical investigation of fracture in SMAs consider 2D SMA plates under plane strain or plane stress condition. These studies provide a valuable foundation for understanding fracture and crack growth in SMAs, however, plane strain or plane stress assumption is an idealization of the real problem. Moreover, regardless of the crack growth scheme being used, the choice of the critical fracture parameters has a substantial effect on the crack growth behavior [60]. Any assumption on the value of a critical fracture parameter, as opposed to an experimentally determined value, makes it difficult to validate the methodology by comparing the results to experimental data. The number of studies that compare FEA against fracture experiments are very limited [25, 67–69], all of which consider static cracks. Although there are various methods for modeling crack growth in SMAs, there is no study on validating such approaches against experimental data.

Regarding actuation crack growth, the existing knowledge is very limited, and only few studies have been devoted to investigate this important phenomenon. There are only a handful of numerical studies [56–58, 66] that has tackled this intriguing problem, and the existing experimental works [18, 38–40] are mostly an observation, rather an attempt to quantify crack growth parameters, and the literature has remained elusive about quantifying the deriving force for crack growth under thermal actuation. Moreover, no relationships, if any, has been established to connect mechanical and actuation crack growth, perhaps because employing the methodologies developed for crack growth under mechanical loading to study crack growth under actuation loading is not straight forward. Therefore, the knowledge acquired from this work could be employed to design damage tolerant SMA actuators where the material often encounters complex thermomechanical loading paths at service.

This study could be considered a step towards establishing standard test methods for measuring the fatigue and fracture properties of SMAs under complex thermomechanical loading conditions.

Moreover, the developed methodologies have the potential to be applied to other phase transforming materials beyond SMAs.

1.4 Objectives

Followings are identified as the objectives of this dissertation.

1. Developing a methodology to measure the fracture toughness of SMAs that takes into account the inherent transformation-induced complexities in their thermomechanical response.

2. Applying the developed methodology to measure fracture toughness of NiTi and NiTiHf SMAs at different testing temperatures.

3. Implementing a 3D finite element model to investigate crack growth under mechanical and actuation loading paths.

4. Developing a methodology to unify fatigue crack growth in SMAs under various thermomechanical loading conditions.

1.5 Outline

The remainder of the dissertation is structured as follows. In Chapter 2, a methodology for measuring the fracture toughness of SMAs from a single load–displacement record is proposed. The methodology is applied to measure the fracture toughness of a near-equiatmic NiTi SMA at various temperatures. In Chapter 3, an SMA constitutive model is validated against experimental results for growing cracks in NiTi compact tension specimen subjected to mode-I isothermal loading by employing the fracture toughness measured in Chapter 2 as the critical crack growth parameter. In, Chapter 4 fracture behavior of a Ni-rich NiTiHf is investigated with conducting mode-I fracture toughness experiment on disk-shaped compact tension specimens at various temperatures. Chapter 5 numerically investigates crack growth under actuation loading in a DCT specimen. The parameters used to calibrate the model and and the critical crack growth parameters is adopted from experiments on a NiTiHf high temperature SMA. In Chapter 6, a unified methodology is proposed for fatigue crack growth in SMAs under two main loading paths, i.e. mechanical and

actuation. The methodology is applied to understand the mechanisms contributing to crack growth in the presence of thermal and mechanical induced phase transformation in a Ni-rich NiTiHf high-temperature SMA under mode-I loading. The resistance of the material to crack growth under both loading paths is characterized by measuring the crack growth rates corresponding to the range of the applied driving force. Chapter 7 concludes the dissertation with a summary of key findings.

2. FRACTURE TOUGHNESS OF NiTi[*]

2.1 Introduction

In this chapter, a methodology for measuring the fracture toughness of SMAs from a single compact tension (CT), isothermal load–displacement record is proposed. It is based on concepts of elastic plastic fracture mechanics (EPFM), employing the J-integral as the fracture criterion, for which the requirements on specimen sizes are much less strict compared to those for the critical stress intensity factor value according to LEFM. The proposed method relies on the ASTM E1820 [71] developed for conventional ductile materials but differs from it in that it takes into account the mismatch among the apparent elastic properties of austenite, self-accomodated, and oriented martensite in SMAs. The chapter is structured as follows. The test method to calculate the fracture toughness of SMAs is described in Section 2.2. Further details on some derivations and calculations are given in the Appendices. In Section 2.3, the material characterization and the experimental procedure are discussed. In Section 2.4, the experimental fracture toughness measurement results are presented and discussed. The chapter concludes with a summary of key findings given in Section 2.5.

2.2 Methodology

In this section, the proposed test method for measuring fracture resistance curves and fracture toughness values in SMAs from a single CT specimen is described. The method accounts for the stress-induced changes in the apparent elastic properties in contrast to the standard test method for ductile materials (ASTM E1820). For plotting the resistance curves, the J-values and crack size values during the loading history are needed and are measured with the aid of partial unloading/reloading sequences during the experiments as described below. To

---

2.2.1 Measurement of J-integral

The expression utilized for the measurement of the J-values during the loading history for stationary cracks is presented first and its modification for advancing cracks subsequently. Both expressions need the elastic compliance slope measured during the partial unloading paths (Figure 2.1b)for distinguishing between their elastic and inelastic components.

2.2.1.1 Stationary Cracks

For stationary cracks, the J-value is calculated from the load–displacement record of a CT specimen as the sum of elastic and inelastic components

$$J = J^{el} + J^{in} = \frac{\eta^{el} A^{el}}{Bb} + \frac{\eta^{in} A^{in}}{Bb}, \tag{2.1}$$

where B is the specimen thickness, W is the specimen width, and $b = W - a$ is the length of the unbroken ligament where a is the crack size (Figure 2.1a). A^{el} and A^{in} are the elastic and inelastic components of the area under the load–displacement curve, respectively (Figure 2.1b). η^{el} and η^{in} are geometry-dependent factors, the existence of which is discussed in Appendix A.

The elastic component of J-integral, J^{el}, in conventional elastic-plastic materials corresponds to Griffith's [72] strain energy release rate, G. Consequently, J^{el} can be calculated for such materials by taking advantage of the relationship between G and the tabulated expressions of the stress intensity factor, K, as a function of crack configuration and load, established by Irwin [73], *i.e.*, $J^{el} = G = K^2/E'$, where $E' = E$ for plane stress and $E' = E/(1 - \nu^2)$ for plane strain, and ν is the Poisson's ratio. Thus, the η^{el} factor determination is actually redundant in those cases. However, the aforementioned expression is not valid for SMAs, for which the Young's modulus, E, assumes different values for austenite, self-accommodated, and oriented martensite.

2.2.1.2 Advancing Cracks

The expression for the J-integral given above, Equation (2.1), is valid only for stationary cracks. For advancing cracks, the incremental formulation proposed by Ernst *et al.* [74] is used for
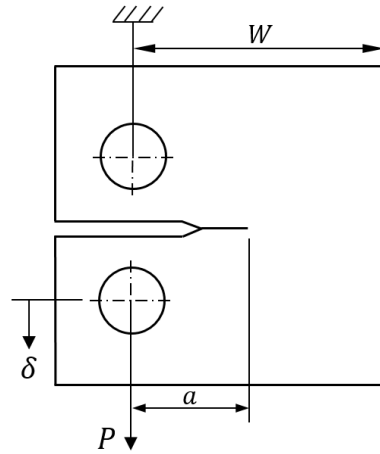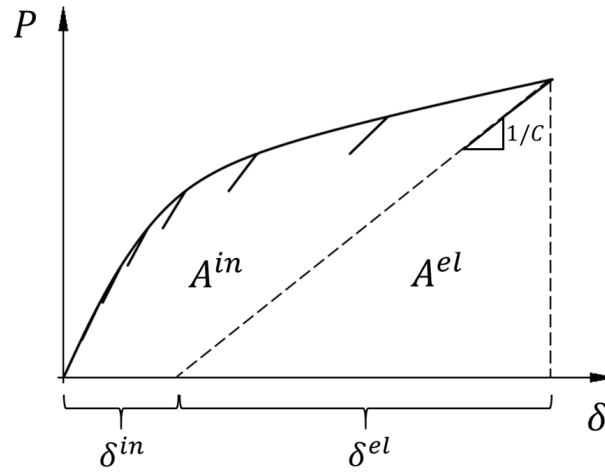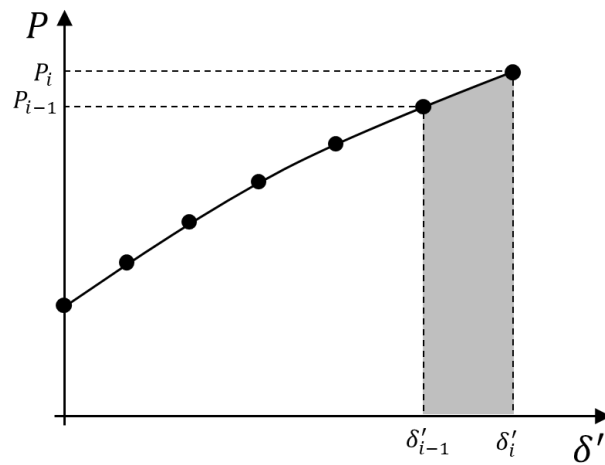
Figure 2.1: Schematic representation of (a) compact tension specimen (b) δ^{el}, δ^{in}, A^{el} and A^{in} on a load-displacement curve; (c) incremental elastic/inelastic area from step $i-1$ to i.

measuring the J-value at the i_{th} loading step as

$$J_i = J_i^{el} + J_i^{in},$$

where J_i^{el} and J_i^{in} are evaluated from the previous step

$$J_i^{el} = \left[J_{i-1}^{el} + \frac{\eta_{i-1}^{el}}{Bb_{i-1}} A_{i-1,i}^{el} \right] \left[1 - \frac{\gamma_{i-1}^{el}}{b_{i-1}} (a_i - a_{i-1}) \right], \tag{2.2}$$

$$J_i^{in} = \left[J_{i-1}^{in} + \frac{\eta_{i-1}^{in}}{Bb_{i-1}} A_{i-1,i}^{in} \right] \left[1 - \frac{\gamma_{i-1}^{in}}{b_{i-1}} (a_i - a_{i-1}) \right]. \tag{2.3}$$

Here γ^{el} and γ^{in} are geometry dependent factors and can be determined using η^{el} and η^{in}, respectively. The details of γ^{el} and γ^{in} evaluation are presented in Appendix A. $A_{i-1,i}^{el}$ and $A_{i-1,i}^{in}$ are the increments of the elastic and inelastic area under a load–displacement record from step $i - 1$ to i, respectively:

$$A_{i-1,i}^{el} = \frac{1}{2}(P_i + P_{i-1})(\delta_i^{el} - \delta_{i-1}^{el}), \tag{2.4}$$

$$A_{i-1,i}^{in} = \frac{1}{2}(P_i + P_{i-1})(\delta_i^{in} - \delta_{i-1}^{in}), \tag{2.5}$$

where $\delta_i^{el} = P_i C_i$ and $\delta_i^{in} = \delta_i - \delta_i^{el}$ are the elastic and inelastic components of the displacement (Figure 2.1c) and C_i is the unloading elastic compliance.

2.2.2 Calculation of Crack Size

To measure crack extension, the elastic compliance method, a widely used technique first introduced by Clarke *et al.* [75] and further enhanced by Joyce and Gudas [76], is used. The crack size corresponding to each unloading/reloading sequence is calculated as follows

$$\frac{a_i}{W} = 1.000196 - 4.06319u + 11.242u^2 - 106.043u^3 + 464.335u^4 - 650.677u^5, \tag{2.6}$$

where $u = 1/\left(\sqrt{BEC_i} + 1\right)$. It should be noted that the elastic compliance method does not take into account the change in apparent elastic properties. For this reason, an *in situ* optical technique

to monitor the crack extension during the experiments was initially implemented. As discussed in detail in Section 2.4, a good agreement between optical measurements and elastic compliance calculations was found. Note that in the elastic compliance calculations, E was assumed equal to the Young's modulus of the stable phase at the nominal temperature at which the experiments took place.

2.2.3 Determination of Fracture Toughness

Once J and Δa values are known, the J–R curve can be constructed, which is essentially a power-law fit to J vs Δa data. To determine the J_{I_C} fracture toughness, the ASTM E1820 procedure is followed. A construction line is first plotted from the origin with a slope of $2\sigma_Y$, where σ_Y is the effective yield strength, *i.e.*, the average of the critical stress, σ_{cr}, and the ultimate tensile strength, σ_{TS}. σ_{cr} denotes either the stress required for initiation of phase transformation or orientation depending on whether the material is in the austenite or self-accommodated martensite state at zero load, respectively. For temperatures higher than martensite desist temperature, M_d, σ_{cr} is the yield stress of austenite. Two exclusion lines are then drawn parallel to the construction line intersecting the abscissa at 0.15 mm and 1.5 mm. J–Δa data points that fall between these two exclusion lines are plotted and a power-law regression is fit throughout. An offset line is then plotted parallel to the construction line, intersecting the abscissa at 0.2 mm. The intersection of the 0.2 mm offset line and the regression line defines the critical value of the J-integral. This interim value can be considered a size-independent fracture toughness value, J_{I_C}, if the qualification requirement, $B > 10\ J_{I_C}/\sigma_Y$, related to the specimen thickness is met. Figure 2.2 shows a typical J–R curve together with the definition of lines and region of qualified data.

2.3 Material Characterization and Experimental Procedure

A binary NiTi rod with a nominal composition of $Ni_{49.5}Ti_{50.5}$ (at.%), processed via hot rotary forging at $800°C$ followed by air cooling, was acquired from ATI. To determine the transformation temperatures, Differential Scanning Calorimetry (DSC) was carried out using a TA Q2000 DSC instrument. A heat/cool cycle at a rate of $10°C/min$ was performed within the 0–$150°C$ temperature
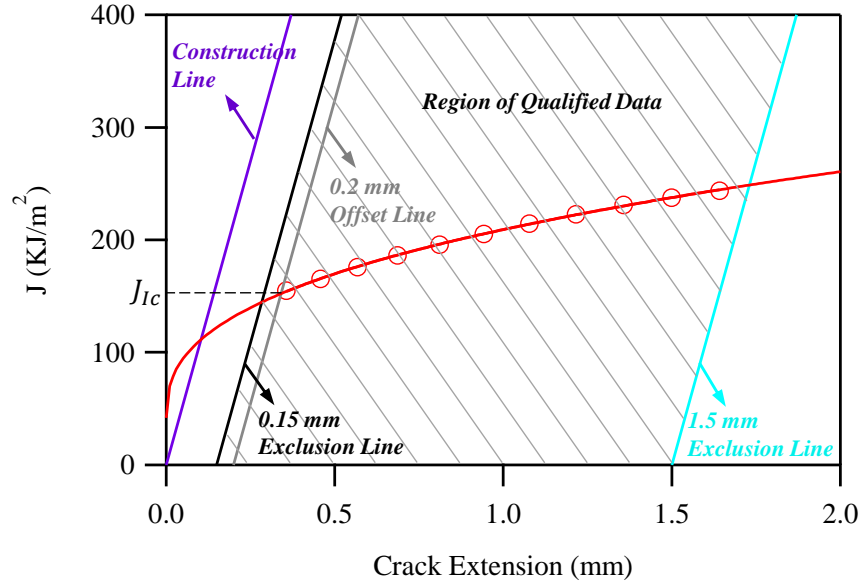
Figure 2.2: Definition of construction lines and region of qualified data.

range. The DSC curve is shown in Figure 2.3. The characteristic phase transition temperatures are obtained based on ASTM F2004 [77] from the intersection of tangent lines as $M_s = 68°C$, $M_f = 42°C$, $A_s = 77°C$ and $A_f = 106°C$ where M_s, M_f, A_s and A_f indicate martensite-start, martensite-finish, austenite-start and austenite-finish temperatures, respectively.

Testing temperatures were selected based on the transformation transition temperatures so that martensitic, transforming, and austenitic materials as defined in the abstract are tested. For the first case, testing was performed below M_f at $T = 25°C$. For the second case, the samples were first heated up to $170°C$, a temperature above A_f, and then cooled down to $80°C$, *i.e.*, above M_s. For the third case, tests were carried out at $170°C$, which is assumed to be greater than M_d. For tensile characterization, dog-bone samples (Figure 2.4(a)) were cut using wire Electrical Discharge Machining (EDM), and pulled to failure with an engineering strain rate of $5 \times 10^{-4} \text{s}^{-1}$ on a servo-hydraulic MTS test frame equipped with a high-temperature MTS extensometer. At each temperature, three tensile tests were carried out to examine the consistency of the results and to obtain the standard deviation. Figure 2.5 shows the stress–strain response from a single experiment at each
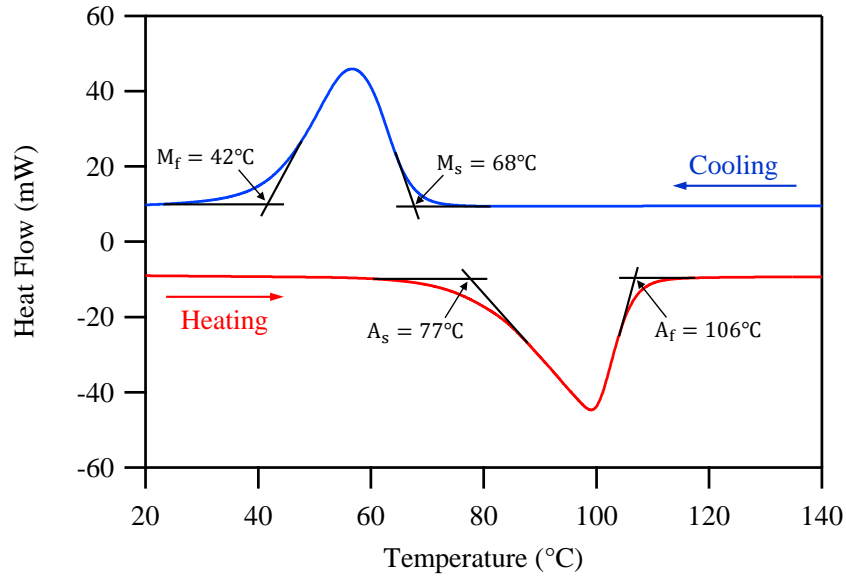
Figure 2.3: DSC curve for the as-received near-equiatomic NiTi SMA sample.

temperature. At room temperature, upon loading, the self-accommodated martensite deformed elastically at low load levels before undergoing orientation/detwinning resulting in a stress plateau at sufficient load levels. The stress–strain curve slope picked up again upon continuing loading as oriented martensite was deformed predominantly elastically. Further loading resulted in slip plasticity and failure. At $80°$C the material was in austenite state at zero load. Application of mechanical loading at that temperature resulted in elastic deformation followed by stress-induced phase transformation occurring at a critical stress value lower than that of orientation/detwinning which is in agreement with the published data [78, 79]. By increasing the load, stress-induced martensite deformed predominantly elastically and then plastically before the occurrence of final failure. It is worth mentioning that at $80°$C, the material does not transform from martensite back to austenite upon unloading. At $170°$C, the material behaved as a conventional ductile metal. In all experiments, a considerable elongation (30-40% strain) was observed. The tensile characterization results are tabulated in Table 2.1.

Fracture tests were performed using CT specimens (Figure 2.4(b)). In order to produce a sharp

27
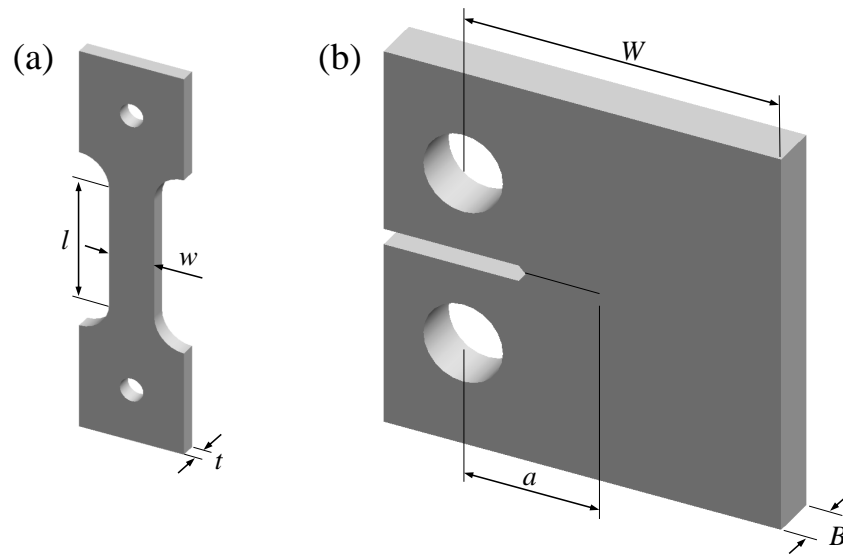
Figure 2.4: Geometry of the NiTi specimens (a) dog-bone for tensile experiments ($l = 8$, $w = 3$, $0.75 \leq t \leq 1.5$, all in mm); (b) compact tension (CT) for fracture experiments ($W = 20$, $9.2 \leq a \leq 10.6$, $2.4 \leq B \leq 3.3$, all in mm).
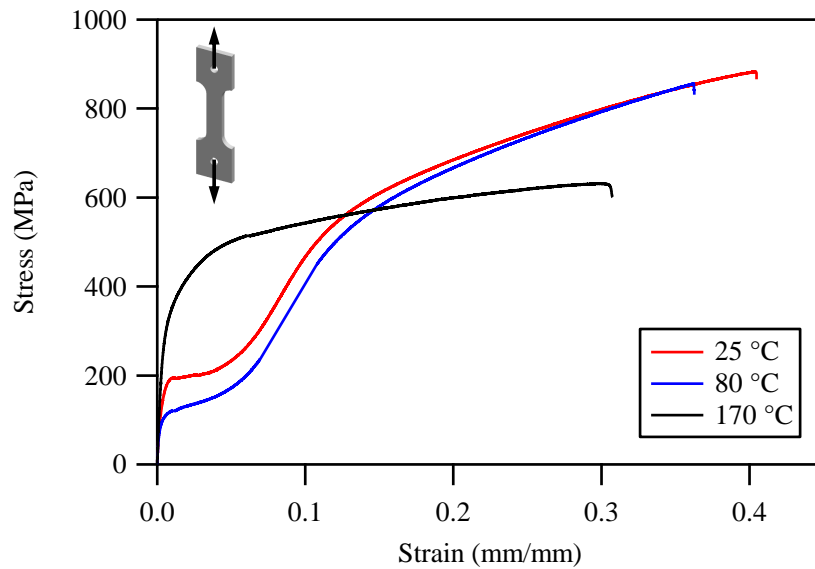
Figure 2.5: Stress-strain curves for near-equiatomic NiTi tested at $25°$C, $80°$C, and $170°$C.

Temperature (°C)	Material Properties		
	E^* (GPa)	σ_{cr} (MPa)	σ_{TS} (MPa)
25	67 ± 3	203 ± 7	950 ± 16
80	74 ± 4	127 ± 9	846 ± 9
170	80 ± 4	274 ± 11	638 ± 8

Table 2.1: Tensile characterization results for near-equiatomic NiTi dog-bone specimens tested at 25°C, 80°C, and 170°C. Three tensile tests were carried out at each temperature. E^* is measured from the initial slope at each testing temperature. σ_{cr} denotes the stress required for either orientation, transformation or austenite yield depending on the material state at zero load. σ_{TS} is the ultimate tensile strength.

crack, specimens were first fatigue pre-cracked at room temperature in a servo-hydralic test frame (MTS model 810) with a sinusoidal waveform at a frequency of 10 Hz. Fatigue pre-cracking was carried out in load control with load values between P_{min} and P_{max}, where P_{max}, initially set equal to 50% of the highest load value expected in the subsequent experiment, was gradually decreased at a normalized K-gradient value equal to -0.01 mm^{-1}. At the end of pre-cracking, all crack sizes, *i.e.*, notch length plus fatigue pre-crack, were within the $0.45 < a/W < 0.55$ range. Displacement-controlled fracture experiments were then carried out in the MTS-810 servo-hydraulic test frame at a loading rate of 0.4 mm/min. Unloading/reloading sequences were performed to measure the specimen compliance. The unload/reload sequences were spaced with the displacement interval 0.1 mm which was approximately equal to $0.01b_0$, recommended by ASTM E1820. Load and actuator displacement, *i.e.*, cross head positions, were recorded continuously at a rate of 10 Hz throughout the test. A correction for machine compliance was then performed to obtain the load-point displacement, which was then converted to load-line displacement via the closed form expressions obtained by Newman [80] (Appendix B). Obviously such corrections are not required if displacement is measured directly from the load-line using a crack opening displacement (COD) gauge.

During each fracture experiment, optical images were recorded continuously from both sides of the CT specimens as schematically shown in Figure 2.6. Two Point Grey CCD cameras equipped with Tokina AT-X PRO lenses were used for image recording. The imaging was performed at an

optical resolution of 0.02 mm/pixel. In one side, the surface was first covered with a white layer of paint and then black speckles were sprayed on it to produce a random pattern. These images were used to measure the full-field Lagrangian strain using digital image correlation (DIC), which is a non-contact optical technique used to measure full-field displacements on the surface of the specimen. Further details on DIC can be found in [81]. Images were post-processed via Vic2D-6 software (developed by Correlated Solutions) to obtain the strain field. The other side of the sample was prepared by mechanical grinding using abrasive papers, followed by polishing with 1 micron diamond suspension. This side is used for monitoring the crack extension. A millimeter scale was directly attached to the polished side of the specimen. Crack size was then measured by post processing the images taken during the experiment, using this scale during post processing. The error in crack extension is expected to be ± 0.05 mm. Similar to the uniaxial tension experiments, CT specimens were tested at 25°C, 80°C, and 170°C. At each temperature, three experiments were carried out to examine the consistency of the results and to obtain the standard deviation. For the tests performed at a higher temperature than room temperature, specimens were heated using a Roy-1500 induction heater and the temperature was measured and controlled using Type K thermocouples attached to the specimen, data acquisition (DAQ) unit, and Labview software. For induction heating, a round coil is designed and the specimen was placed inside it. The length of the coil was extended to both sides of the specimen with the crack line parallel to the coil axis. Because of the relatively high thermal conductivity of NiTi and the relatively small size of the specimens, this heating technique does not produce an appreciable thermal gradient. The temperature was then measured at six different locations of the sample and a dwell time for ten minutes ensured a uniform temperature field within $\pm 2^\circ$C. The experimental setup is shown in Figure 2.7.

2.4 Results and Discussion

2.4.1 Load–Displacement Response

The experimental load-displacement data for NiTi CT specimens at the three testing temperatures are shown in Figure 2.8. At all temperatures, stable crack extension was observed throughout
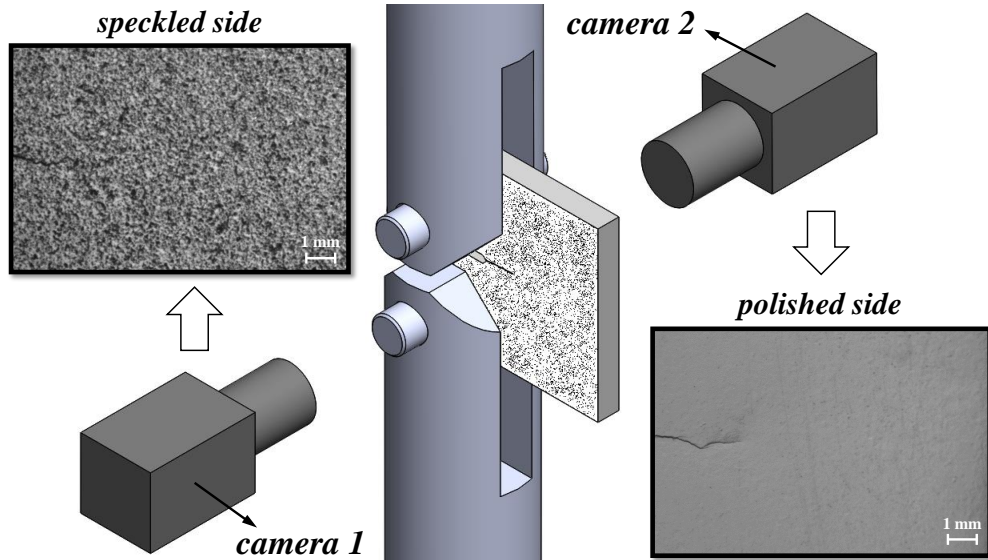
Figure 2.6: Schematic of the experimental setup for recording images from both sides of CT specimens.

the tests. The load-displacement responses can be separated to three stages. In the first stage, the response is linear. In the second stage, it deviates from linearity and reaches a maximum. After the maximum load is reached, in the third stage, the load decreases gradually without any significant load drop until the end of the test. The deviation from linearity is associated with orientation, transformation, and/or plasticity in the specimens.

In the experiments at room temperature (Figure 2.8(a)), a significant deviation from linearity was observed at early stages of loading. At $80°$C (Figure 2.8(b)), this deviation was delayed and the load maxima were comparable to those achieved at room temperature. At $170°$C (Figure 2.8(c)), similar to the tests at $80°$C, deviation from linearity was delayed compared to room temperature. Moreover, at $170°$C the load maxima were considerably higher than the two previous cases. It can be seen from Figure 2.8 that the load-displacement curves do not comply with the characteristic features of a linear elastic material and the data can not be interpreted on the basis of LEFM.
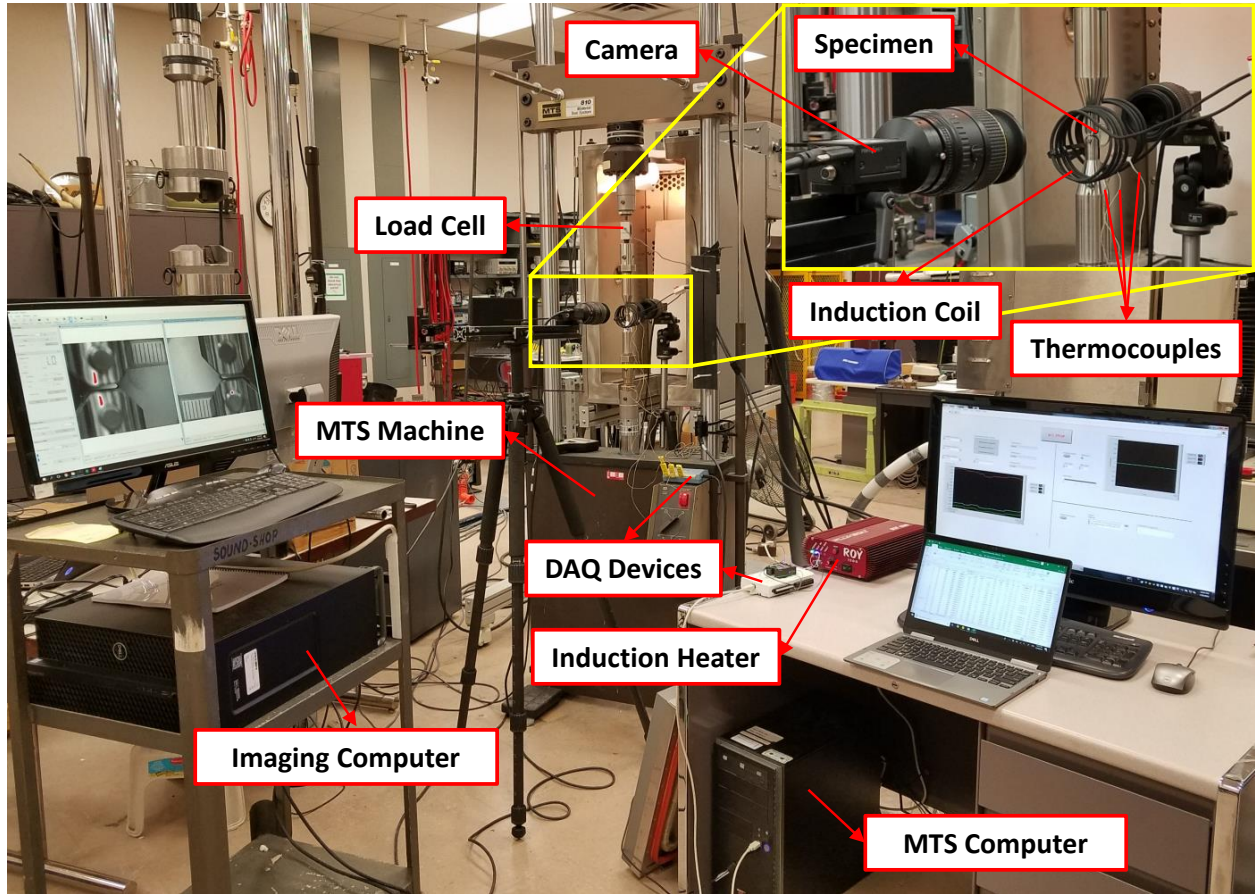
Figure 2.7: The experimental setup used for fracture toughness tests.
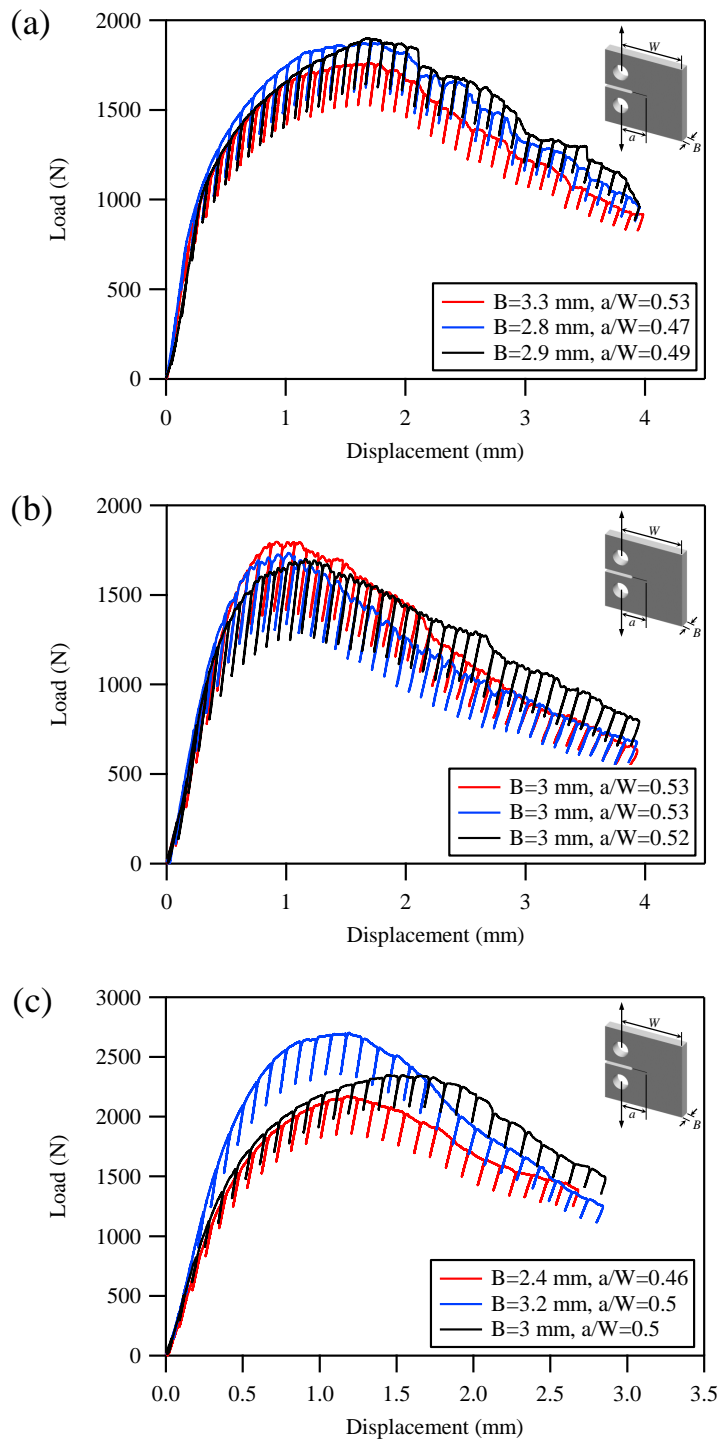
Figure 2.8: Experimental load-displacement curves for NiTi CT specimens tested at: (a) 25°C, (b) 80°C, and (c) 170°C.

2.4.2 In-situ Observations

This section details the information obtained from the *in situ* optical imaging of the NiTi CT specimens. For the sake of brevity, results from a single experiment at $80°C$ are presented. In Figure 2.9, the corresponding load-displacement response is displayed and the load points (a)–(d) at which optical results will be provided are identified. As noted earlier, the speckled surface was used to obtain the strain distribution by the *in situ* DIC technique while the polished surface of the specimen was used for tracking the crack extension as well as observing the surface morphology.

The Lagrangian strain field along the direction normal to the crack line, ε_{yy}, for NiTi at $80°C$, is shown on the left side of Figure 2.10 where (a)–(d) correspond to the load points of Figure 2.9. The color bar is adjusted such that the regions with red color, *i.e.*, $\varepsilon_{yy} \geq 6\%$, approximate the fully transformed region. Point (a) corresponds to the early stages of deviation from linearity. As the load point displacement was increased, strain accumulated symmetrically along two lobes on each side of the crack line at angles of approximately $50°$ from the crack tip and the crack extended into the fully transformed region (point (b)). Further increase in displacement resulted in expanding the transformation zone along the lobes (point (c)). At point (d), transformation under compression was observed at right hand side of the specimen.

The images taken from the polished surface are presented on the right side of Figure 2.10. It can be seen that when the curve started to deviate from linearity (point (a)), the surface morphology changed as a result of phase transformation in front and to the sides of the crack tip. With increased load point displacement, the crack extended stably along the x-axis and into the transformed region (point (b)). Further increase in displacement caused the aforementioned transformation zone to expand and the crack extended further (point (c)). As the crack size increased further, a similar morphology as a result of the compressive load at the right hand side of the CT specimen was observed (point (d)).
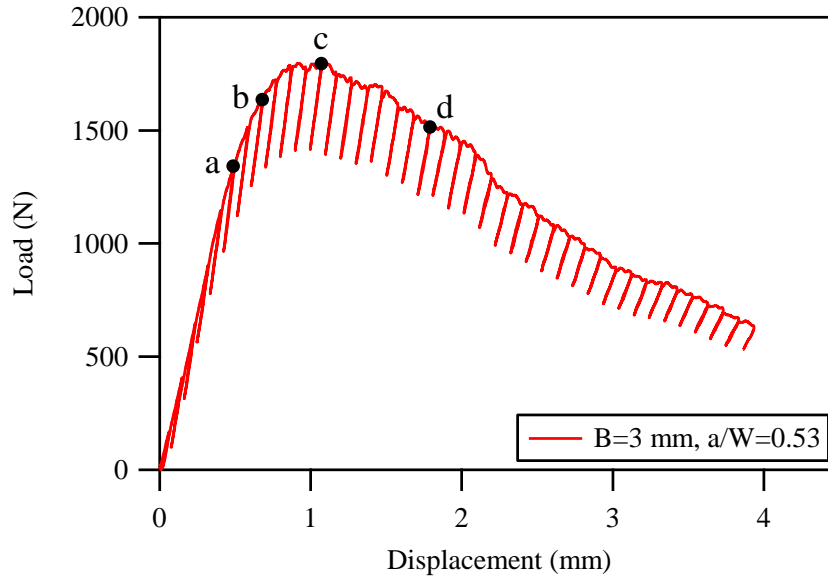
Figure 2.9: Load-displacement curve for NiTi CT specimen tested at $80°$C. Points a-d are the load points for which the optical results are provided.

2.4.3 Crack Growth Measurements

The crack size was measured using two methods: the elastic unloading compliance method (Equation (2.6)) and optical imaging. It is worth mentioning that the compliance data was first corrected for rotation (details of rotation correction can be found in ASTM E1820) and a least-squares minimization was performed to reduce data scattering. The elastic unloading compliance method does not take into account the change in the apparent elastic properties of the material and for this reason an optical imaging method was also used to track crack growth. The *in situ* imaging monitors crack extension from the surface of specimen, and consequently, no through the thickness crack growth information can be obtained, *i.e.*, tunneling could not be observed if present. However, no signs of tunneling were found from the *post mortem* examination of the fracture surfaces. As shown in Figure 2.11 in which crack extension measured from both methods is plotted versus load point displacement for the three experiments preformed at $80°$C, no significant difference (< 0.1 mm) is expected if either method is to be used, at least for the
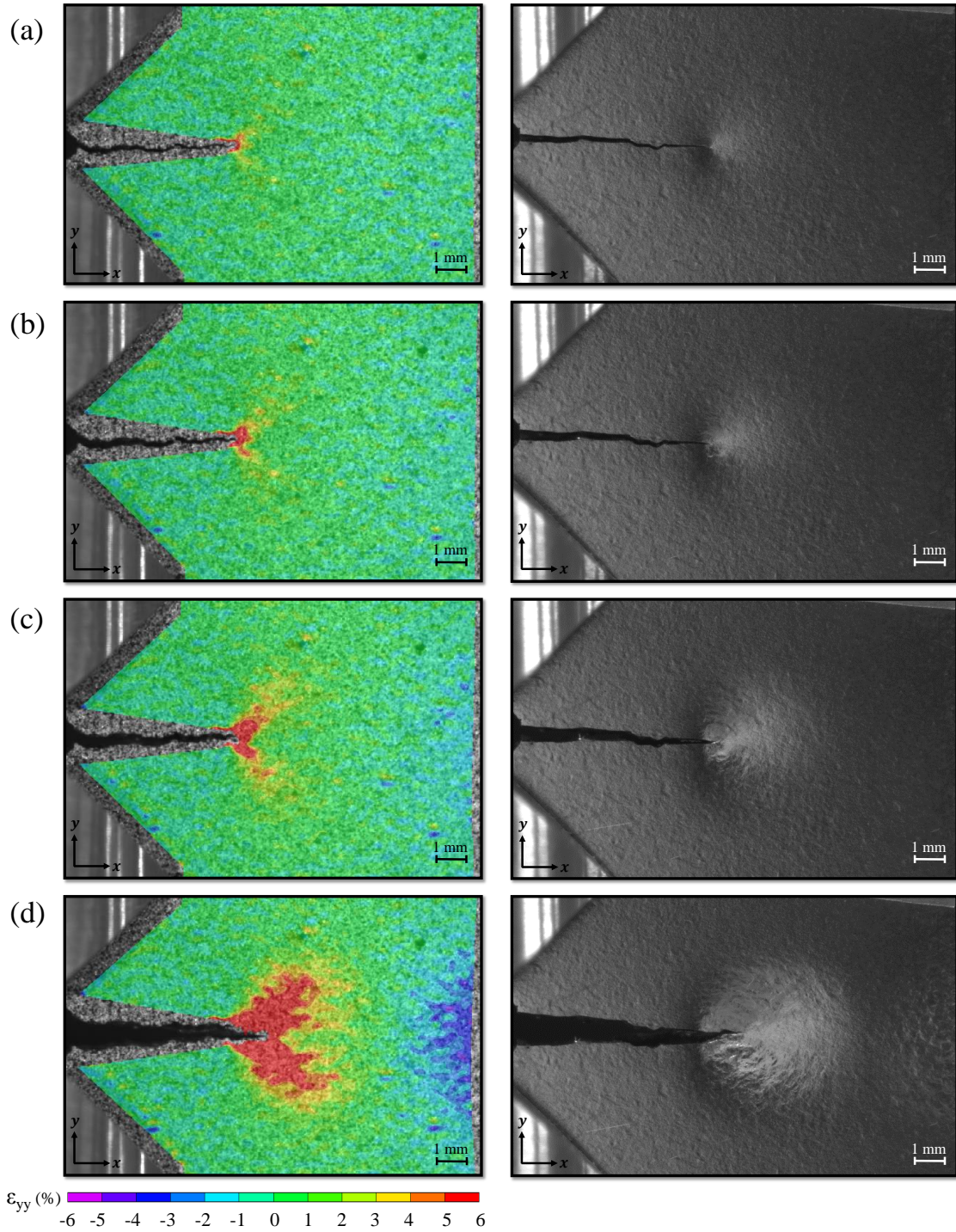
Figure 2.10: Strain (ε_{yy}) contour plots obtained from *in situ* DIC on the speckled surface (left) and optical images of the polished surface (right) showing the evolution of transformation zone in the NiTi CT specimen during crack growth. (a)-(d) correspond to the load points on the load-displacement curve (Figure 2.9).
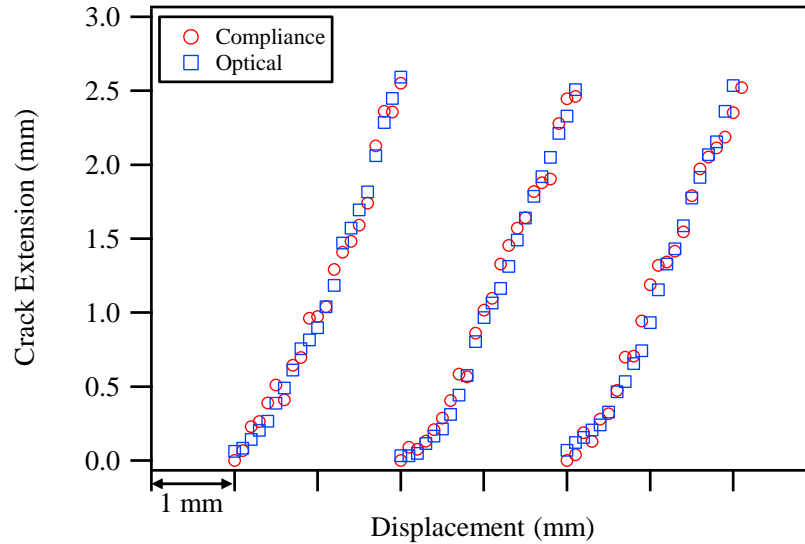
Figure 2.11: Evolution of crack size measured using elastic compliance and optical imaging for the experiments at $80°$C.

material system tested. Although the optical method is recommended since it does not require any assumption of the apparent elastic properties, one may use the compliance method without expecting any substantial error in the results. Another popular method to evaluate crack extension is the potential drop method, which, however, requires additional testing equipment and specimen machining. Furthermore, this method would be impractical for SMAs in which, in addition to crack growth, phase transformation can affect the potential drop signal. This would complicate the separation of the effect of crack growth and phase transformation on the potential drop.

2.4.4 Fracture Toughness

To measure the resistance to crack extension, fracture resistance curves were developed. At each load increment corresponding to unloading/reloading sequences on the load-displacement record (Figure 2.8), the J-values were calculated using Eqs. (2.2) & (2.3). For the tests carried out at $170°$C, since the material response (Figure 2.5) is that of a conventional ductile solid, the ASTM

37

E1820 method would also apply to obtain the J^{el}-values, *i.e.*, through the stress intensity factor

$$K = \frac{P}{B\sqrt{W}} \; f\left(\frac{a}{W}\right),$$

where $f(a/W)$ is a geometry-dependent shape function, given in ASTM E1820 as

$$f\left(\frac{a}{W}\right) = \frac{2 + \left(\frac{a}{W}\right)\left[0.886 + 4.64\left(\frac{a}{W}\right) - 13.32\left(\frac{a}{W}\right)^2 + 14.72\left(\frac{a}{W}\right)^3 - 5.6\left(\frac{a}{W}\right)^4\right]}{\left(1 - \frac{a}{W}\right)^{\frac{3}{2}}}.$$

Once the J-values and Δa values are obtained, J–R curves can be developed (Figure 2.12). Following the procedure described in Section 2.2, the J_{I_C}-values were obtained from the intersection of the 0.2 mm offset line and the regression line. The slope, $2\sigma_Y$, of the offset line approximates the apparent crack advance due to crack tip blunting when there is no slow stable crack tearing under the assumption that, before tearing, the crack advance is equal to one half of the crack-tip opening displacement. In SMAs, crack tip blunting is not as pronounced as in conventional ductile materials and such an assumption may be an exaggeration [14]. Given though that J_{I_C} is not the fracture toughness value at the initiation of crack advance but rather an approximation of it, the aforementioned assumption was adopted in our calculations. The obtained J_{I_C} values are presented in Figure 2.14, according to which the average fracture toughness of martensitic and transforming materials is relatively close while that of stable austenite is higher. The J_{I_C}-values satisfy the ASTM E1820 thickness requirement, $B > 10 \, J_{I_C}/\sigma_Y$, which according to the ASTM standards ensures J-dominance. It should be noted, however, that although according to the standards, any thickness can be used as long as the qualification requirement is satisfied, the thickness of the specimen tested is outside the suggested range $2 \leq W/B \leq 4$ and an experimental investigation on samples with a higher W/B-ratio would thus be desirable.

The extrapolated $K_{J_{I_C}}$-values, calculated using $K_{J_{I_C}} = \sqrt{E' \, J_{I_C}}$ where E' corresponds to the stable phase at the temperature at which the experiments were conducted, are plotted in Figure 2.14 together with the critical stress intensity factors, K_Q, obtained from LEFM (if were to

38
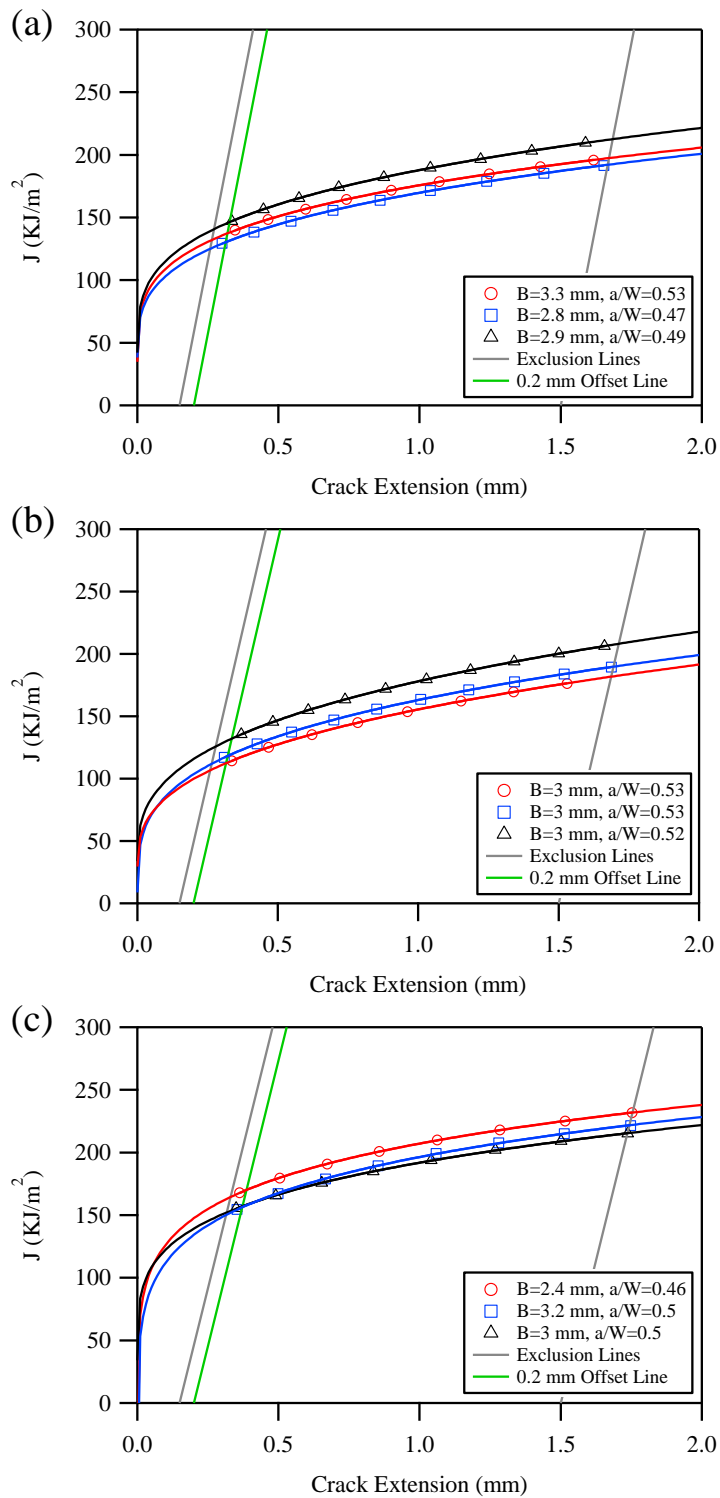
Figure 2.12: J-R curves for NiTi CT specimens tested at: (a) 25°C, (b) 80°C, and (c) 170°C. The intersection of the regression line and the 0.2 mm offset line defines the critical value, J_{I_C}.
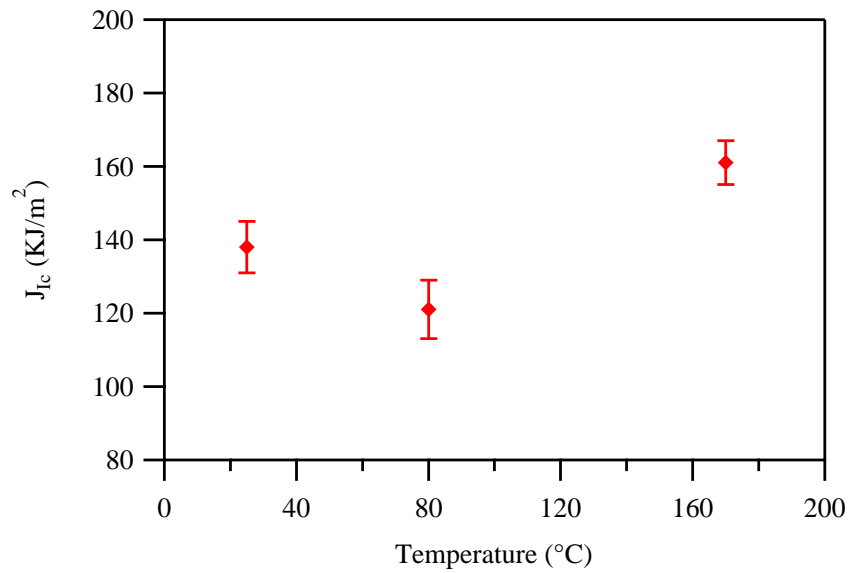
Figure 2.13: J_{I_C} values for NiTi CT specimens tested at 25°C, 80°C, and 170°C. The values corresponding to martensitic and transforming materials are relatively close while the fracture toughness of stable austenite is considerably higher.
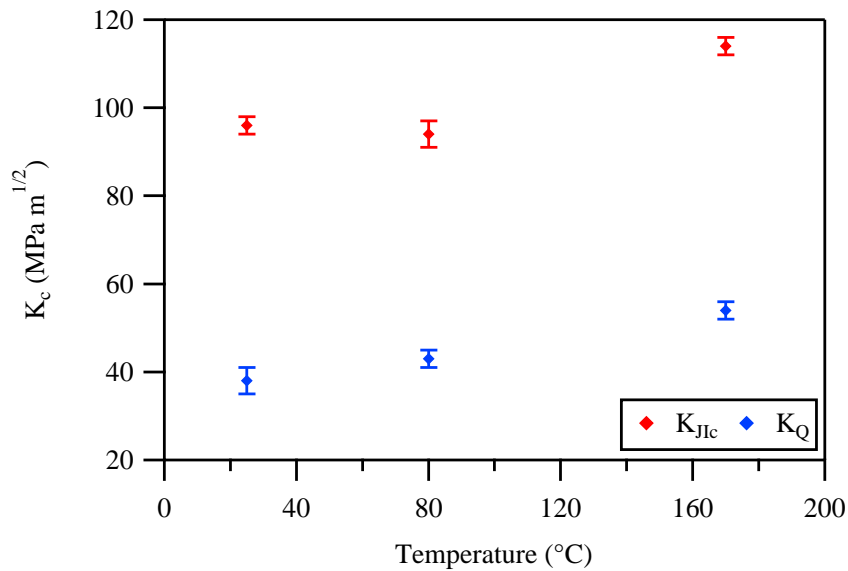
Figure 2.14: $K_{J_{I_C}}$ and K_Q values for NiTi CT specimens tested at 25°C, 80°C, and 170°C. The extrapolated $K_{J_{I_C}}$-values are much higher than the corresponding K_Q-values reported on the basis of LEFM. The extrapolated values of martensitic and transforming materials are found to be approximately the same.

Temperature (°C)	Fracture Toughness		
	J_{I_C} (KJ/m^2)	$K_{J_{I_C}}$ (MPa$\sqrt{\text{m}}$)	K_Q (MPa$\sqrt{\text{m}}$)
25	138 ±7	96 ±2	38 ±3
80	121 ±8	94 ±3	43 ±2
170	161 ±6	114 ±2	54 ±2

Table 2.2: Fracture toughness results for NiTi CT specimens tested at 25°C, 80°C, and 170°C.

assumed valid) for comparison purposes. The average values for all measured critical parameters are tabulated in Table 2.2. The K_Q-values are similar to the ones reported in the literature [14, 16, 20, 21, 23, 29]. It is observed that at each testing temperature, the $K_{J_{I_C}}$-values are much higher than the corresponding K_Q-values reported on the basis of LEFM. Moreover, comparing the $K_{J_{I_C}}$-values at 25°C and 80°C one can see that the fracture toughness values of the martensitic and transforming specimens are almost identical. A plausible explanation for the identical fracture toughness values is that at both temperatures the crack grows into a region of oriented martensite although the far-field material phase is different, *i.e.*, self-accommodated martensite at room temperature or austenite at 80°C–the difference in the apparent elastic properties of the far-field material explains why the corresponding J_{I_C}-values are not as close as the $K_{J_{I_C}}$-values. In the literature [14, 19, 24], it was argued, based on LEFM, that the fracture toughness of SMAs depends monotonically on temperature and this argument is further supported by the K_Q-values obtained from our experiments. However, the more rigorous results of the proposed method depict that the fracture toughness dependence on temperature, in the temperature range of interest in SMAs, is piece-wise constant, below and above M_d, with the fracture toughness above M_d, *i.e.*, the fracture toughness of stable austenite, being considerably higher.

2.5 Summary

The fracture toughness of near-equiatomic NiTi was measured experimentally via a mechanics-aided test methodology using the J-integral as the fracture criterion. The test method used relies on the ASTM E1820 standard method for measuring the fracture toughness of conventional ductile materials extended to account for the transformation and orientation-induced changes in the

apparent elastic properties by evaluating the elastic component of J using an η^{el}-factor. Isothermal fracture experiments were carried out on compact tension specimens at three distinct temperatures, below the martensite-finish temperature, between the martensite-start temperature and the martensite desist temperature, M_d, and above M_d. At these temperatures the material either remains in the martensite state throughout the loading (martensitic material) or transforms from austenite to martensite close to the crack tip (transforming material) or remains always in the austenite state (austenitic material), respectively. The fracture toughness values obtained (critical J-values for crack growth) result in extrapolated stress intensity factors that are about three times greater than the ones reported in literature. This discrepancy is due to the fact that the previously reported values were based on the assumption that the specimen response could be described by linear elasticity despite the fact that the zone of nonlinearity in those experiments was substantial. Moreover, according to the obtained results, and in contrast to literature, the fracture toughness of martensitic and transforming materials was found to be approximately the same, most probably because in both cases the fracture toughness value measured corresponds to the fracture toughness of martensite close to the crack tip. The fracture toughness of stable austenite (above M_d) in contrary was found to be considerably higher.

This work is considered a step towards establishing standards for measuring the fracture toughness of phase transforming materials. Towards this end, modifications to the proposed method regarding the linear compliance method, blunting line slope, and the thickness requirement for J-dominance may be desirable but such modifications are not anticipated to alter any of the aforementioned conclusions of this work.

3.   STABLE CRACK GROWTH IN NiTi: FINITE ELEMENT MODELING AND EXPERIMENTAL VALIDATION[*]

3.1   Introduction

In this chapter, an SMA constitutive model is validated against experimental results for growing cracks in a 3D NiTi compact tension (CT) model subjected to mode-I isothermal loading. The model parameters are calibrated by preforming uniaxial tensile characterization experiments and the virtual crack closure technique (VCCT) is employed as the crack propagation criterion using an experimentally determined fracture toughness value. The remainder of the chapter is structured in the following manner. The constitutive material model for the thermomechanical response of polycrystalline SMAs is given in Section 3.2. The calibration of model parameters is presented in Section 3.3. Section 3.4 describes the finite element boundary value problem and the solution methodology. Results pertaining to crack growth behavior are presented and discussed in Section 3.5. Section 3.6 concludes the chapter by summarizing the key findings.

3.2   Material Model

The constitutive model for polycrystalline SMAs, developed by Lagoudas et al. [83] within the framework of continuum thermodynamics, is adopted and briefly described in this section. The constitutive model considers martensitic volume fraction (ξ), transformation strain ($\boldsymbol{\varepsilon}^t$), and transformation hardening energy (g^t) to be the internal state variables. The martensitic volume fraction is a scalar quantity ($0 \leq \xi \leq 1$) that accounts for the volume fraction of all martensitic variants. The transformation strain is the recoverable inelastic strain generated and recovered during forward and reverse stransformation, respectively. Transformation hardening energy is a measure of the nonlinear change in the mixing energy as phase transformation progresses under constant

---

stress. The model uses specific Gibbs free energy of the form

$$G(\boldsymbol{\sigma}, T, \boldsymbol{\varepsilon}^t, \xi, g^t) = -\frac{1}{2\rho}\boldsymbol{\sigma} : \boldsymbol{S} : \boldsymbol{\sigma} - \frac{1}{\rho}\boldsymbol{\sigma} : [\boldsymbol{\alpha}(T - T_0) + \boldsymbol{\varepsilon}^t]$$
$$+ c\left[(T - T_0) - T\ln\frac{T}{T_0}\right] - s_0 T + u_0 + \frac{1}{\rho}g^t, \tag{3.1}$$

where $\boldsymbol{\sigma}$ is the stress tensor, T is the absolute temperature, T_0 is a reference temperature, and ρ is the mass density. $\mathbf{S}$ and $\boldsymbol{\alpha}$ are the effective compliance and thermal expansion tensors, respectively, and c is the effective specific heat coefficient. s_0, and u_0 denote the effective specific entropy and effective specific internal energy at the reference state, respectively. The effective material properties are defined in terms of ξ using the rule of mixtures [84]. Assuming any change in the current state of the system is only with a change in ξ [84], the evolution of $\boldsymbol{\varepsilon}^t$, *i.e.* flow rule, is given as

$$\dot{\boldsymbol{\varepsilon}}^t = \boldsymbol{\Lambda}\dot{\xi}, \quad \boldsymbol{\Lambda} = \begin{cases} \boldsymbol{\Lambda}^{fwd}, \ \dot{\xi} > 0, \\ \\ \boldsymbol{\Lambda}^{rev}, \ \dot{\xi} < 0, \end{cases} \tag{3.2}$$

where $\boldsymbol{\Lambda}$ is the transformation tensor and determines the magnitude and direction of transformation strain. $\boldsymbol{\Lambda}^{fwd}$ and $\boldsymbol{\Lambda}^{rev}$ are the transformation direction tensors during forward and reverse transformation, respectively, and are defined as [84]

$$\boldsymbol{\Lambda}^{fwd} = \frac{3}{2}H^{cur}\frac{\boldsymbol{\sigma}'}{\bar{\sigma}}, \quad \boldsymbol{\Lambda}^{rev} = \frac{\boldsymbol{\varepsilon}^t}{\xi}, \tag{3.3}$$

where $\bar{\sigma} = \sqrt{\frac{3}{2}\boldsymbol{\sigma}' : \boldsymbol{\sigma}'}$ is the Mises equivalent stress and $\boldsymbol{\sigma}'$ is the deviatoric part of the stress tensor. H^{cur} denotes the uniaxial transformation strain magnitude for complete transformation and is a function of stress

$$H^{cur}(\bar{\sigma}) = H_{sat}\left(1 - e^{-k\bar{\sigma}}\right), \tag{3.4}$$

where H_{sat} is the maximum transformation strain, and k controls the rate at which H^{cur} exponentially evolves to H_{sat}. The evolution of transformation hardening energy, g^t, is given as

$$\dot{g}^t = f\dot{\xi}, \quad f = \begin{cases} f^{fwd}, \; \dot{\xi} > 0, \\ \\ f^{rev}, \; \dot{\xi} < 0, \end{cases} \tag{3.5}$$

where f is the hardening function and defines transformation hardening behavior. f^{fwd} and f^{rev} are the hardening functions during forward and reverse transformation, respectively, and are defined as

$$\begin{cases} f^{fwd} = \frac{1}{2}a_1(1 + \xi^{n_1} - (1 - \xi)^{n_2})) + a_3, \\ \\ f^{rev} = \frac{1}{2}a_2(1 + \xi^{n_3} - (1 - \xi)^{n_4})) - a_3, \end{cases} \tag{3.6}$$

where the exponents n_1, n_2, n_3, and n_4 accept values in the range $0 < n_i \leq 1$ and provide smooth transition in the thermo-mechanical response at the initiation and completion of transformation. a_1 a_2 and a_3 can be calculated using the stress-temperature phase diagram. Using the definition of G and the evolution equations, and with the procedure of Coleman and Noll [85], the total infinitesimal strain is obtained as

$$\varepsilon = \boldsymbol{S} : \boldsymbol{\sigma} + \boldsymbol{\alpha}(T - T_0) + \varepsilon^t, \tag{3.7}$$

Rewriting Equation (3.7) in terms of stress yields

$$\boldsymbol{\sigma} = \boldsymbol{C} : [\varepsilon - \boldsymbol{\alpha}(T - T_0) - \varepsilon^t], \tag{3.8}$$

where $\boldsymbol{C} = \boldsymbol{S}^{-1}$. Moreover, the Clausius-Planck inequality, *a.k.a.* the local dissipation inequality, can be written as

$$\pi\dot{\xi} \geq 0, \tag{3.9}$$

where π is the thermodynamic force conjugated to ξ. For Equation (3.9) to be satisfied, π must be positive when ξ is increasing, and negative when ξ is decreasing. Assuming the phase transformation will take place when π, reaches a threshold value, Y, this can be defined in an implicit way by introducing a transformation function , Φ, such that

$$\Phi = 0, \quad \Phi = \begin{cases} \Phi^{fwd} = \pi^{fwd} - Y^{fwd}(\boldsymbol{\sigma}), \ \dot{\xi} > 0, \\ \\ \Phi^{rev} = -\pi^{rev} - Y^{rev}(\boldsymbol{\sigma}), \ \dot{\xi} < 0, \end{cases} \tag{3.10}$$

where π^{fwd}, π^{rev} are the thermodynamic driving forces for forward and reverse transformation, respectively. Y^{fwd}, Y^{rev} are the critical value of the thermodynamic force to initiate and sustain forward and reverse phase transformation, respectively.

3.3 Calibration of Model Parameters

Given the constitutive relations in the previous section, the common material parameters that are used to calibrate the model are: the elastic modulus of austenite and martensite, E_A and E_M; Poisson's ratio of austenite and martensite, ν_A and ν_M; the parameters for $H^{cur}(\bar{\sigma})$ in Equation (3.4), $i.e.$, k and H_{sat}; transformation temperatures at zero load, $i.e.$, austenite start A_s, austenite finish A_f, martensite start M_s and martensite finish M_f; and austenite and martensite stress–temperature slopes, C_A, and C_M.

To calibrate the model, characterization tests were carried out on flat dog-bone samples, electro-discharge machined from a binary NiTi rod with a nominal composition of $Ni_{49.5}Ti_{50.5}$ (at.%). The elastic moduli were measured from an isothermal stress–strain curves [70]. To obtain the phase transformation characteristics, isobaric experiments were carried out where the sample was loaded under uniaxial tension to various load levels and then thermally cycled. The results are presented in Figure3.1a. A schematic on how the phase transformation characteristics are determined in each isobaric tensile experiment is depicted in Figure3.1b. The critical transformation temperatures for start and finish of the forward and reverse phase transformation are measured by drawing tangent lines, as shown in Figure 3.1b. These critical temperatures are then used to generate stress–

Parameter	Value	Parameter	Value
E_A	74 GPa	M_s	67°C
E_M	68 GPa	M_f	57°C
ν_A	0.33	A_s	94°C
ν_M	0.33	A_f	106°C
H_{sat}	6 %	C_A	8 MPa/°C
k	0.026 MPa^{-1}	C_M	15 MPa/°C

Table 3.1: Material parameters used in finite element simulations. The parameters are calibrated based on the uniaxial isothermal and isobaric experiments on near-equiatomic NiTi.

temperature phase diagram (Figure 3.2a). The transformation temperatures at zero stress levels are extracted with extrapolation. Moreover, austenite and martensite stress–temperature slopes, C_A and C_M, are obtained as the average of the slopes of the linear regression lines for the start and finish of transformation: $C_A = (C_{A_s} + C_{A_f})/2$, and $C_M = (C_{M_s} + C_{M_f})/2$. The attained maximum transformation strain, $H^{cur}(\bar{\sigma})$ generated under each uniaxial stress level is measured as shown in Figure 3.1b, and is plotted as a function of applied constant stress value. This is presented in Figure 3.2b where the tendency of $H^{cur}(\bar{\sigma})$ to saturate with increasing applied stress level is demonstrated with an exponential fit. The relevant material properties obtained from characterization tests are shown in Table 5.1.

3.4 Numerical Boundary Value Problem

As mentioned in Chapter 1 plane strain/stress assumption is an idealization of the real problem. A brief discussion on the effect of such idealization on crack tip stress distribution and transformation zone in 2D cracks is provided in Appendix C. Therefore, employing a 3D model enables a direct comparison with experimental data without the need to make an assumption on the stress state. To this end, a 3D finite element boundary value problem of a compact tension SMA specimen, with dimensions identical to the one in [70], is set up in Abaqus finite element suite (Figure 3.3a). A pre-crack, represented by "unbonded" nodes, is introduced that simulates the fatigue pre-crack in a typical crack growth experiment. To mimic the mode-I experiment, displacement in the top pin hole is pinned (rotation is allowed) while displacement is specified in the y direction at the bottom
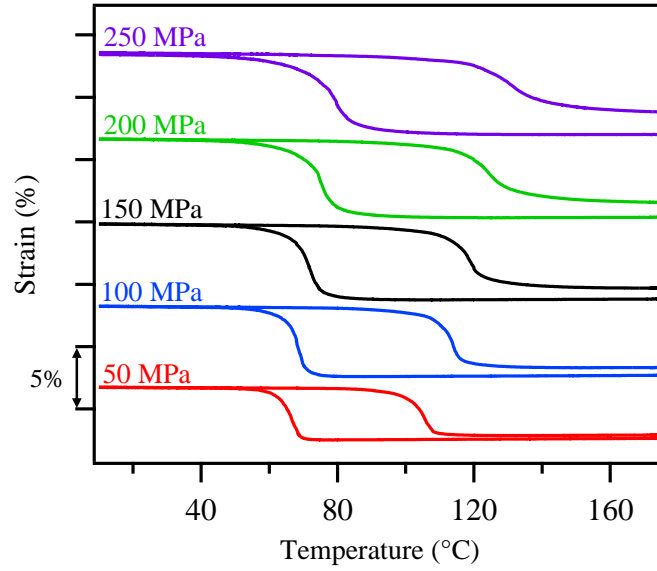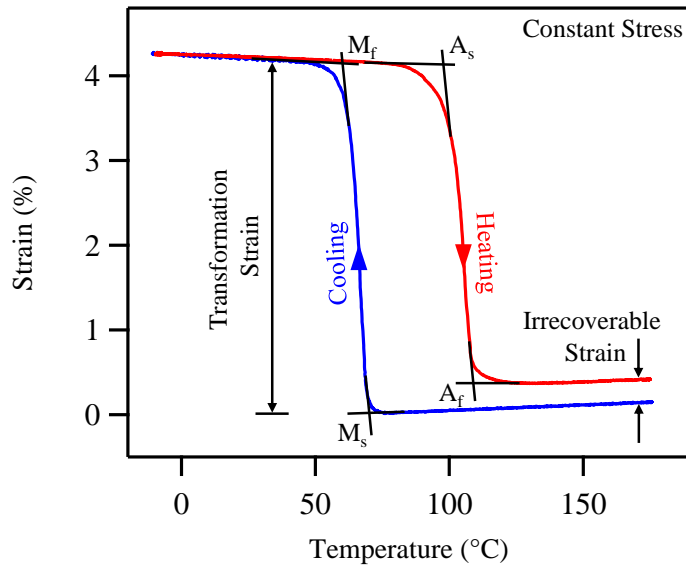
Figure 3.1: (a) Strain–temperature response of NiTi under isobaric tensile experiment at various applied stress level; (b) schematic of a typical SMA response, and how the phase transformation characteristics are obtained from a heating–cooling cycle.
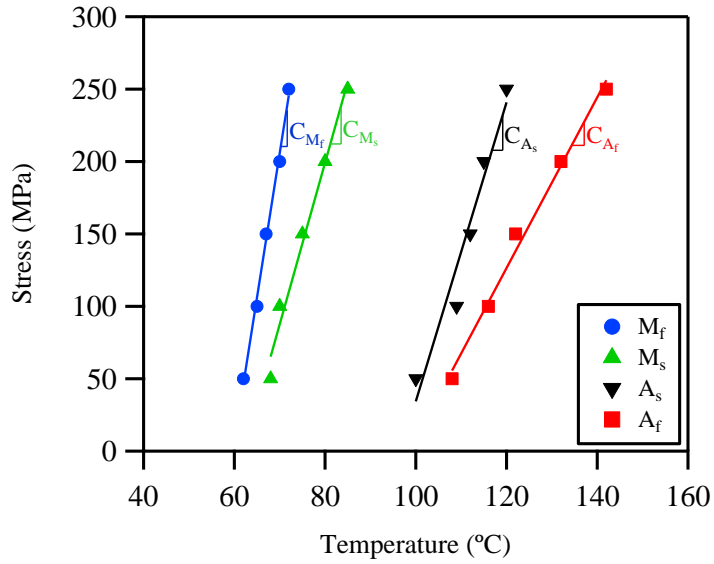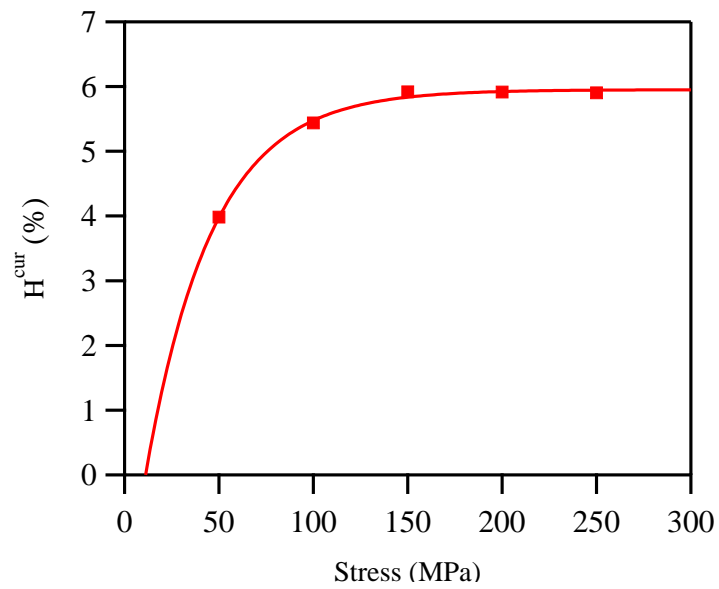
Figure 3.2: (a) Stress-temperature phase diagram; (b) saturation of maximum transformation strain, $H^{cur}(\sigma)$, with increasing applied stress level.

pin hole. An isothermal loading path at $T = 80°C$ is adopted for the simulation. At this tempera-ture, the austenitic material transforms to martensite upon loading but does not reverse transform upon unloading. Eight-node linear brick hexahedral elements with reduced integration (C3D8R) are used. A total of 210048 elements are employed in the finite element model and mesh is highly refined along the crack line to accurately capture the near-tip fields as shown in Figure 3.3a.

The crack tip energy release rate, G, is used as the driving force for crack growth and the VCCT is utilized for its calculation. The VCCT is based on the following assumptions: (i) the energy released in the process of a certain amount of crack extension is equal to the energy required to close the crack by the same amount, and (ii) there is no significant change in the state of the crack tip as it moves by an infinitesimal distance Δa, *i.e.* from a to $a + \Delta a$. The fracture criterion is defined as $G \geq G_c$ where G_c is the the critical value at which debonding occurs. Considering J as the nonlinear energy release rate [86], the critical value is specified from the fracture toughness measurements on near-equiatomic NiTi presented in Chapter 2. Figure 3.3b demonstrates VCCT for eight-noded 3D solid elements where only a section of the model is illustrated for convenience. For the elements placed in the crack front, the mode-I energy release rate, G_I, is computed as

$$G_I = -\frac{1}{2\Delta S} P^i (v^l - v^{l*}).$$
(3.11)

Here $\Delta S = \Delta a d$ is the area virtually closed where Δa is the length of the elements at the crack front, and d is the width of the elements. P^i is the nodal force at the crack tip and perpendicular to the crack plane, and v^l and v^{l*} denote the opening displacement of the upper and lower crack surfaces, respectively (Figure 3.3b).

3.5 Results and Discussion

3.5.1 Load–Displacement

The numerically obtained load–displacement curve under isothermal mode-I loading of the SMA CT specimen is shown in Figure 3.4a. The load is calculated from the reaction force at the pinned top pin hole, while displacement is obtained from the bottom pin hole, where the verti-

(a)

(b)
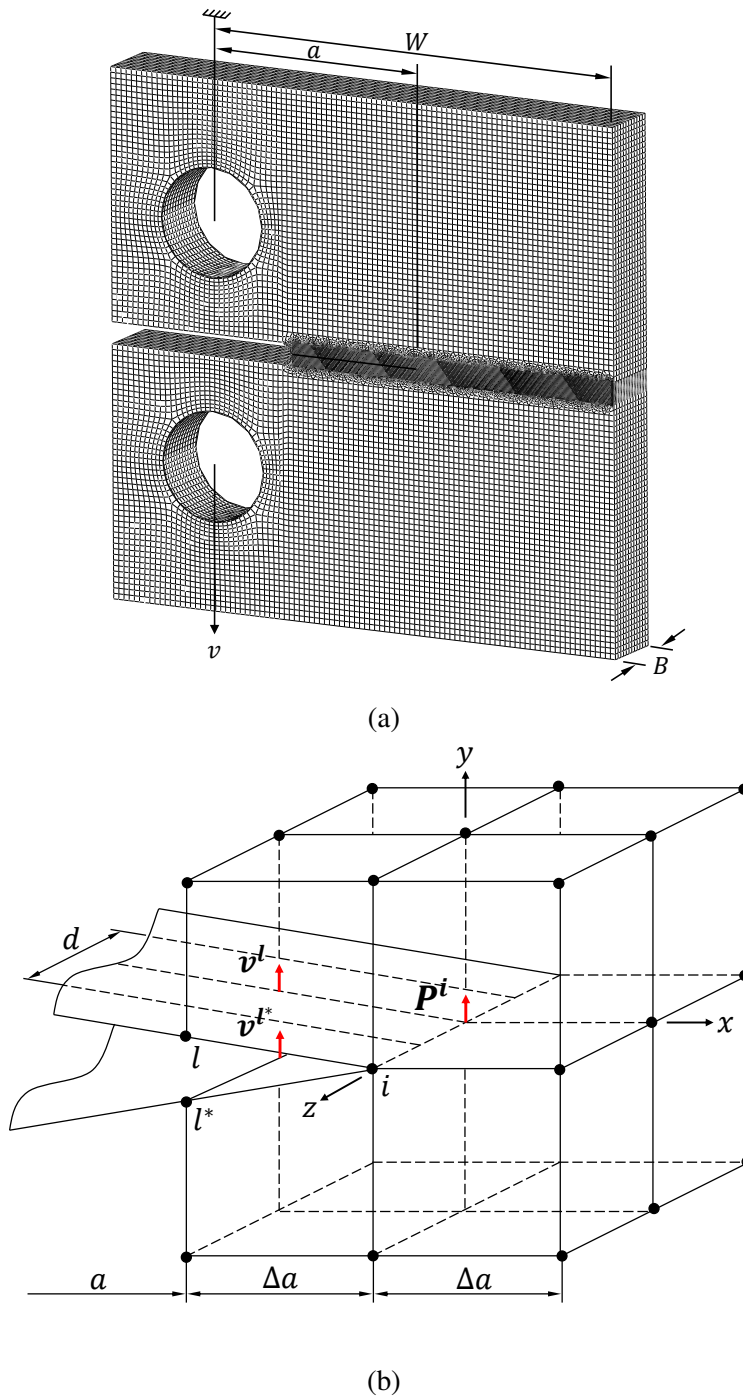
Figure 3.3: (a) Finite element boundary value problem and the mesh geometry; (b) virtual crack closure technique for eight-noded three-dimensional solid elements.

cal displacement boundary condition is applied. The load-displacement characteristics can be explained in three stages: (i) the response is linear at the beginning, which corresponds to small-scale transformation close to the crack tip; (ii) a deviation from linearity appears, which corresponds to the large-scale transformation at the crack tip, and continues until a maximum load is attained; (iii) followed by a gradual decrease without any abrupt drop, indicating stable crack growth. Good agreement is observed between numerical results and experimental data obtained from NiTi CT specimen at $T = 80°$C [70] (Figure 3.4b). To show the importance of selecting the proper fracture criterion, a finite element simulation is also carried out using the same geometry, material parameters, and boundary conditions, but with a different critical energy release rate. This time, instead of using J_{Ic}, the critical parameter is calculated using $G_{Ic} = K_Q^2/E'$ where K_Q is the experimentally determined interim critical stress intensity factor, which is obtained by linear elastic fracture mechanics (LEFM), and E' is the effective elastic modulus. The result is included in Figure 3.4b, according which the agreement with the experimental data is poor.

3.5.2 Strain Distribution

The in-plane strains near the crack-tip at the maximum load are presented in Figure 3.5, where ε_{xx}, ε_{xy}, and ε_{yy} contours are plotted in Figure 3.5(a),(b), and (c), respectively. Note that the contour plots shown in the figure correspond to the strains calculated at the surface of the CT model. This enables a direct comparison with the experimental results obtained using digital image correlation (DIC) which is a surface measurement technique. The details on the experimental setup and post-processing can be found in Chapter 2. The experimentally measured in-plane strains are shown in Figure 3.5(d)-(f). For each strain component, the numerical and experimental results share color bars for the ease of comparison. In all figures, the crack tip is set as the origin. In general, a good agreement is observed between the numerical predictions and the experimental results in terms of overall shape of contours and magnitude of strains. The numerically obtained results, however, slightly overpredict the strains, most probably due to the fact that the maximum load is attained at a larger applied displacement value compared to the experiment, as can be seen in Figure 3.4b. Moreover, comparing the shape of contours, a difference in the angle of the two
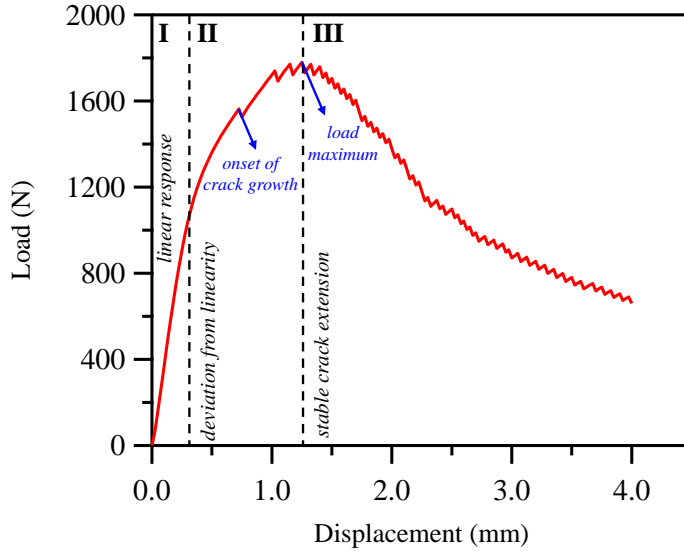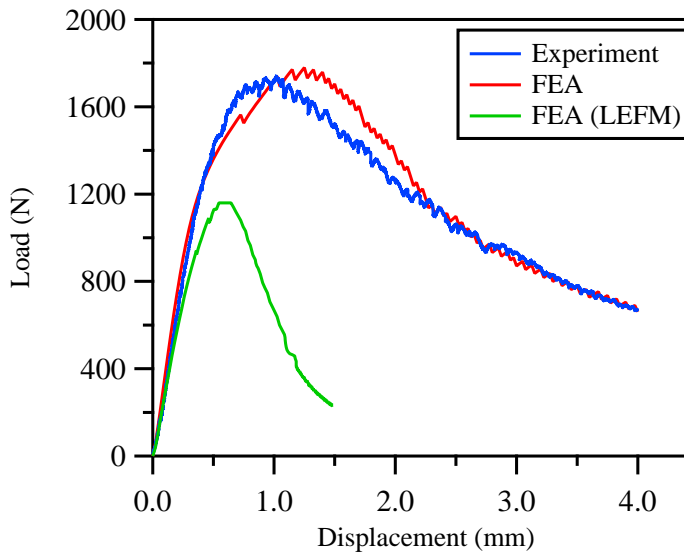
Figure 3.4: (a) Load–displacement curve under mode-I isothermal loading of the compact tension SMA model showing three stages: (i) linear response; (ii) deviation from linearity towards load maximum; and (iii) stable crack growth; (b) comparison of experimentally measured load–displacement curve with the ones calculated using FEA.

lobs in front of the crack tip can be recognized for the strains in loading direction (ε_{yy}).

3.5.3 Transformation Zone

The evolution of stress-induced transformation zone near the crack tip is presented in Figure 3.6. To determine the transformation zone, the equivalent strain $\varepsilon_{eq} = \sqrt{\frac{2}{3} e : e}$ is calculated where e is the deviatoric part of the strain tensor. The strains are normalized by H_{sat} and for viewing ease, the color bar is set so that dark blue represents the untransformed region, red represents the fully transformed region, and the colors in between represents transforming region. The evolution of transformation zone is shown at the following points on the load-displacement curve: (i) at the early stage of loading corresponding to $v = 0.5$ mm, (ii) at the onset of crack extension, (iii) at the maximum attained load, and (iv) after 1 mm crack extension. The numerically results obtained from the surface of the CT model are presented in Figure 3.6(a), (b), (c), and (d), respectively. Upon loading, stress near the crack tip increases and a martensitic transformation zone appears at the crack tip. The transformation size is relatively small in the early stages of loading (Figure 3.6(a)). At the onset of crack extension, *i.e.*, the crack extends into a fully transformed martensitic region while the far-field phase is austenite (Figure 3.6(b)). During crack growth the transformation zone expands (Figure 3.6(c) and (d)) while the martensitic material left behind the growing crack exerts a closing force and provides a shielding effect, which justifies the stable crack growth observed. To evaluate the transformation zone experimentally, the equivalent strains are obtained using DIC and are plotted in Figure 3.6(e)-(h) for points (i)-(iv), respectively. Comparing the results with the numerically obtained ones, a good agreement is observed especially for the overall size of the transforming region. The numerical results slightly overpredicts the size of the fully transformed region at the crack tip.

3.5.4 Crack Front

The variation of mode-I energy release rate, G_I, at the crack tip and on the crack plane is presented in Figure 3.7a for different values of applied displacements. It can be seen that G_I attains the maximum value at the middle through the thickness of the specimen, and decreases
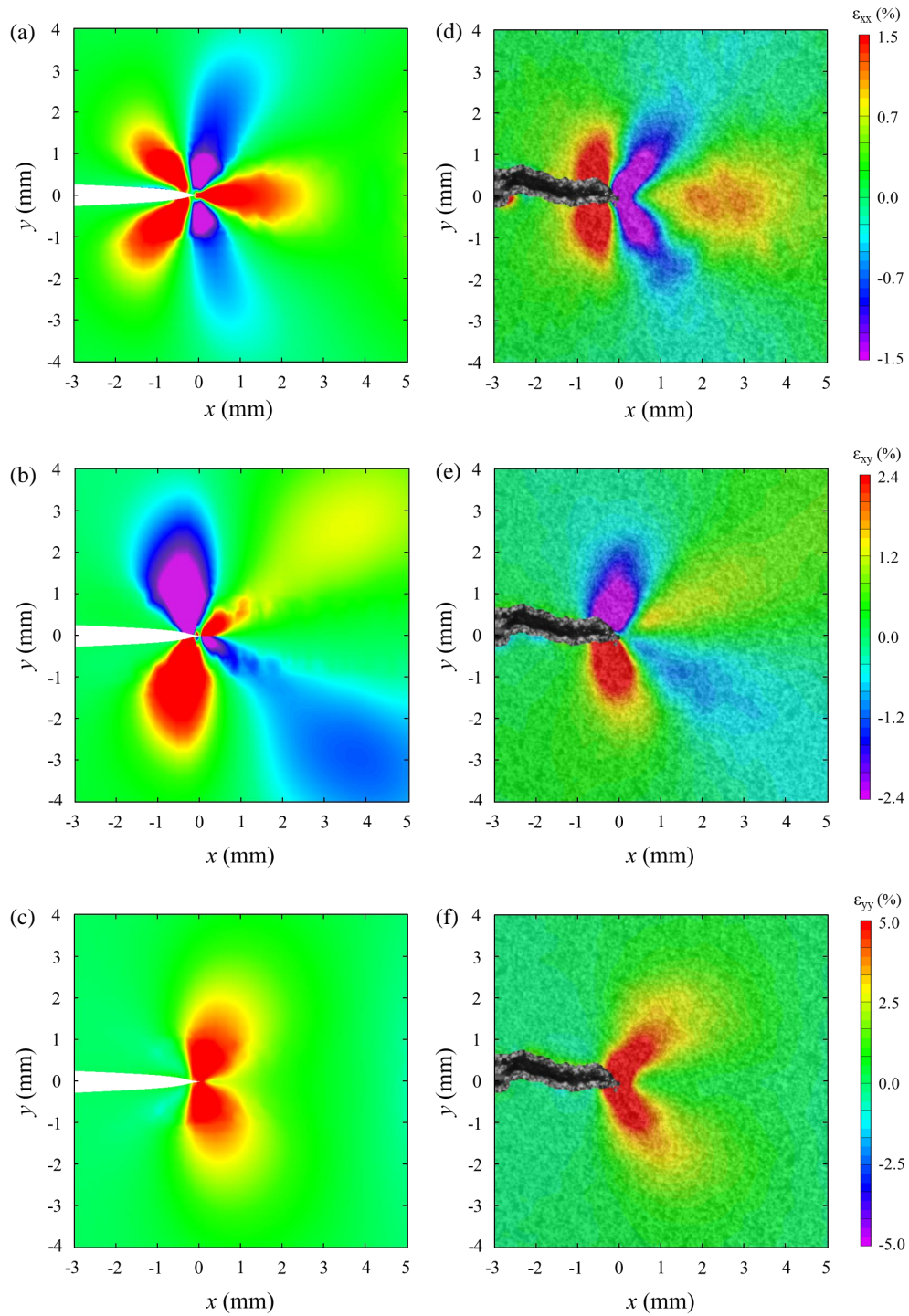
Figure 3.5: Contour plots of in-plane strains near the crack-tip of NiTi SMA at the maximum attained load: (a,d) ε_{xx}, (b,e) ε_{xy}, and (c,f) ε_{yy}, calculated from FEA (left) and measured using digital image correlation (right).

Figure 3.6: Evolution of transformation zone near the crack tip. The normalized equivalent strains ε_{eq}/H_{sat} are obtained numerically (top), and experimentally using digital image correlation (bottom) at different stages of loading: (a),(e) at the early stage of loading corresponding to $v = 0.5$ mm; (b),(f) at the maximum attained load; and (d),(h) after 1 mm crack extension.
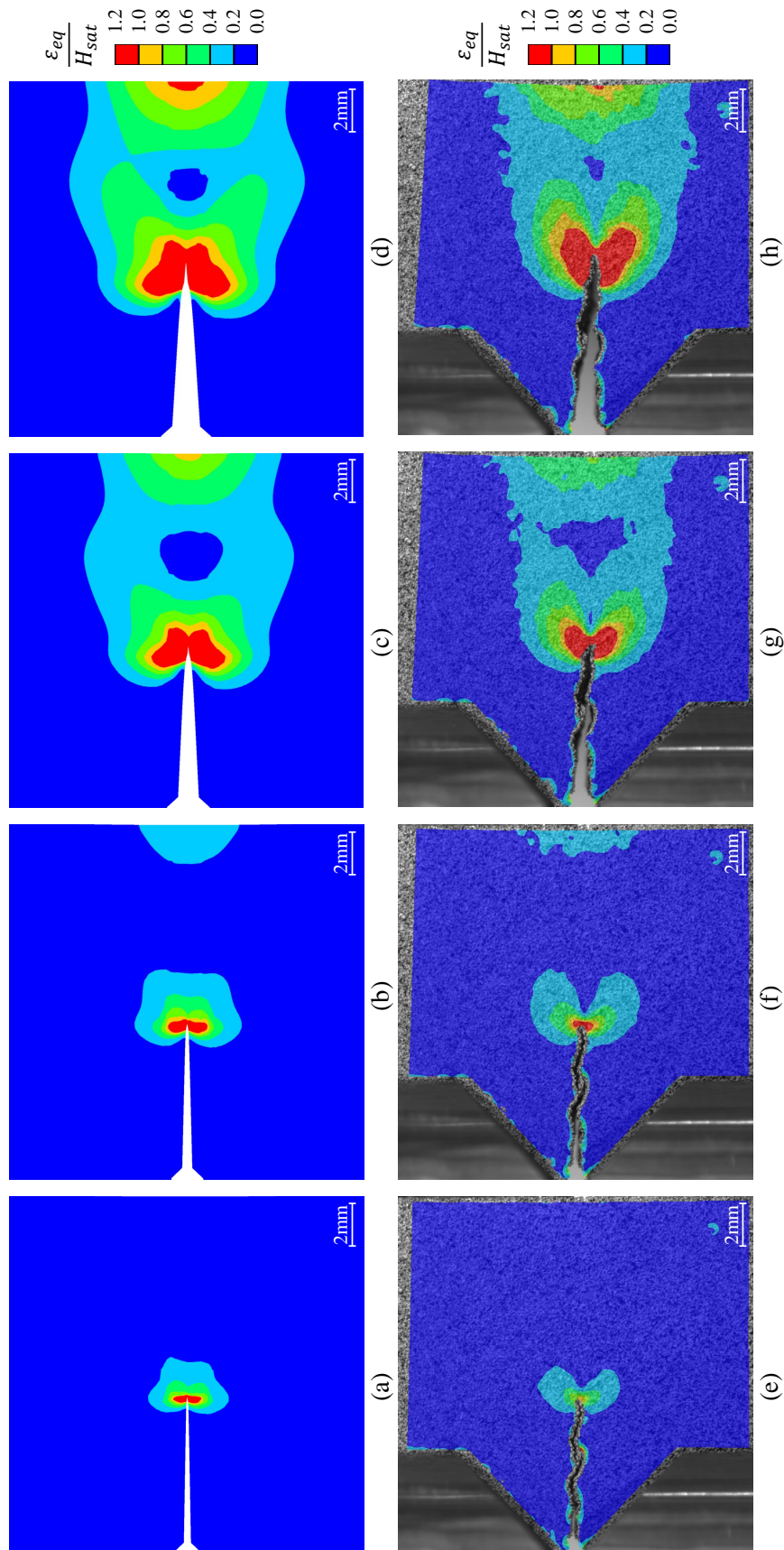
symmetrically and attains minimum value at the surface. The variation of G_I through the thickness can be explained by the change in the state of stress. To this aim, Figure 3.7b plots the out-of-plane normal stress, σ_{zz}, near the crack tip and through the thickness. Since the stress state on the surface is close to plane stress, σ_{zz} contours attain minimum value. Consequently, on the surface, the maximum shear stress occurs in planes making $45°$ with the plane of the specimen (xy-plane). Moving towards the middle, the stress state tends to plane strain and σ_{zz} has its maximum value at the middle. In this case, the maximum shear stress occurs in planes normal to the plane of specimen and making $45°$ with the crack plane. More details on this is provided in Appendix C.

Although the variation of G_I through the thickness may imply that the crack grows faster in the middle, where the triaxiality is higher, crack front is found to remain straight during crack growth simulations. This agrees with the post mortem examination of the fracture surface, as shown in Figure 3.8. According to the SEM micrograph, shear lips are not evident on the fracture surface of the NiTi CT specimen. The flat fracture surface indicates cleavage fracture, and therefore suggests much less sensitivity of the fracture toughness to the specimen thickness. The decrease in fracture toughness with specimen thickness is usually observed in the materials with ductile crack growth (microvoid coalescence), and has roots in through-thickness variation of triaxiality which results in flat fracture surface in the middle and shear lips near the free surface. Therefore, the stringent thickness requirement for such materials may be relaxed for SMAs where cleavage fracture prevails. The effect of thickness on fracture toughness of NiTi SMAs that aims to relax such requirements is currently under investigation.

3.6 Summary

Crack growth under mode-I loading and in the presence of stress-induced martensitic phase transformation is investigated in a NiTi compact tension model via 3D finite element analysis on the basis of a developed constitutive law. The virtual crack closure technique is implemented and crack is assumed to extend when the energy release rate reaches its critical value. It is shown that the characterization of the material response from uniaxial experiments and the experimentally measured fracture toughness result in simulations of the fracture response that agree quite well

(a)

(b)
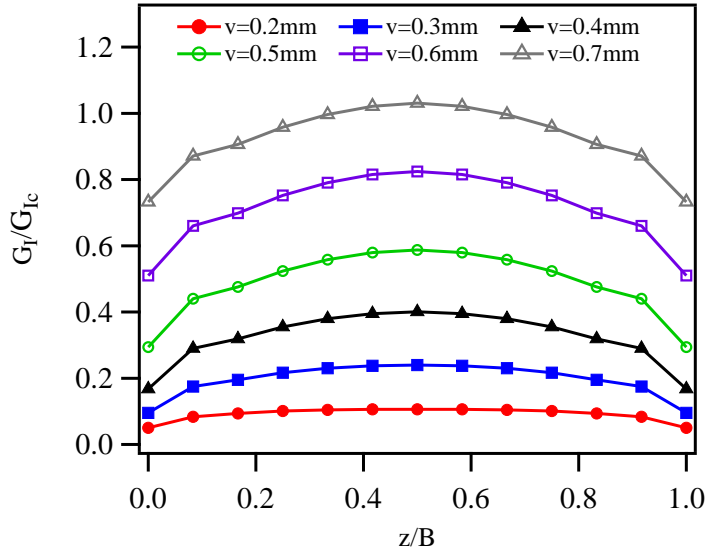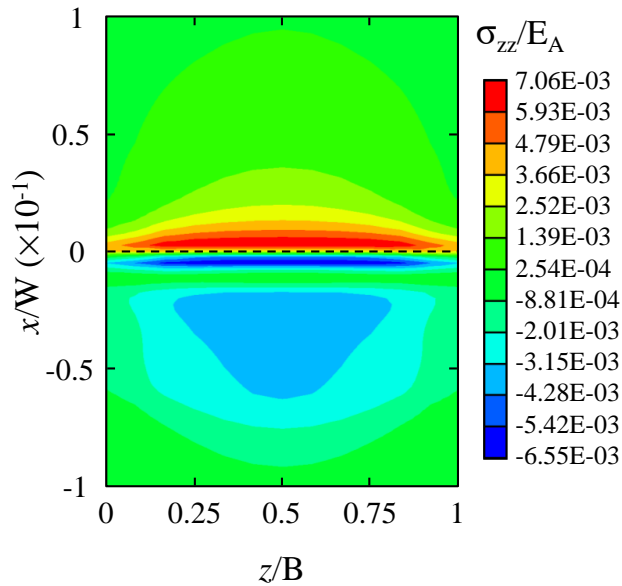
Figure 3.7: (a) (a) Variation of mode-I energy release rate, G_I, at the crack tip and through the thickness for different values of applied displacement; (b) out-of-plane normal stress, σ_{zz}, near the crack tip and through the thickness. Crack front is shown by the dashed line at $x/W = 0$.
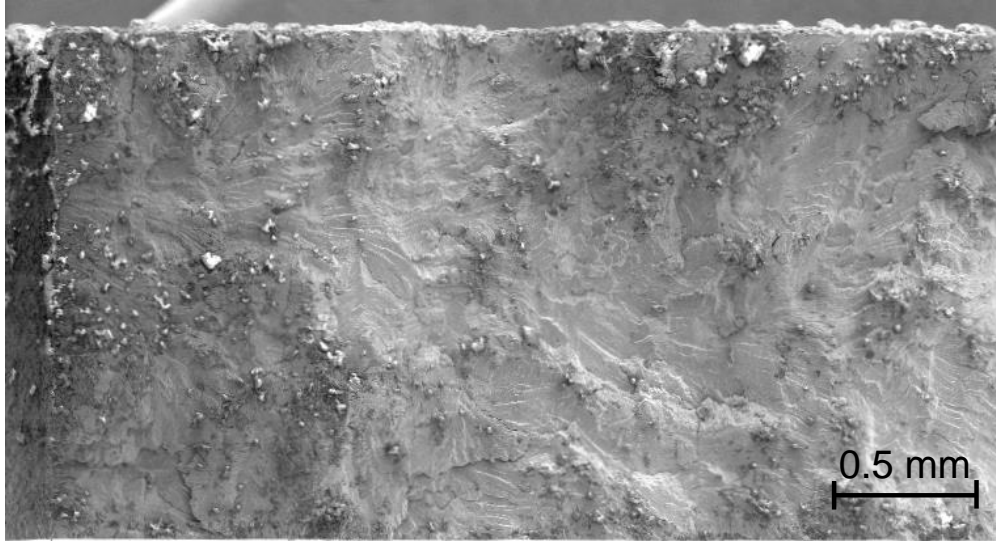
Figure 3.8: Scanning electron microscopy (SEM) image of the fracture surface of NiTi compact tension specimen.

with the experimental data in terms of the load–displacement curve, near-tip strain distribution, and the size and shape of the stress-induced phase transformation zone at different stages of loading. Further studies are currently under way to explore the effect of specimen thickness on fracture of SMAs.

4.   FRACTURE OF NiTiHf HIGH-TEMPERATURE SMA

4.1   Introduction

In this chapter, fracture behavior of a Ni-rich NiTiHf is investigated. Mode-I isothermal fracture experiment was carried out at three temperatures (selected based on phase transformation temperatures) resulting in three different constitutive response. Load–displacement data were measured and fracture toughness values were obtained, revealing the effect of testing temperature on fracture behavior. The chapter is organized as follows: Section 4.2 describes the material and explains the experimental methods. Section 4.3 presents and discusses the results. Finally, a summary of key findings is provided in Section 4.4.

4.2   Material and Methods

A Ni-rich high-temperature SMA bar with a nominal composition of $Ni_{50.3}Ti_{29.7}Hf_{20}$ (at.%) was acquired from ATI. All samples were first solution heat treated at $900°C$ for one hour followed by water quenching to assure a single phase structure. Subsequently, the samples were aged at $550°C$ for three hours followed by water quenching to tailor the precipitate structure and resulting transformation temperatures. Samples were cut using electrical discharge machining (EDM): circular shape for differential scanning calorimetry (DSC), dog-bone for tensile characterization, and disk-shaped compact (DCT) for fracture experiment. Because the bulk material was in the form of bar, selection of DCT geometry instead of CT allowed for more efficient use of the material.

Transformation temperatures at zero load were measured using a TA Instruments differential scanning calorimeter with a heating/cooling rate of $10°C/min$ within $0–300°C$ range. The DSC results are presented in Figure 4.1. The transformation temperatures at zero load were obtained from the intersection of tangent lines as $M_s = 135°C$, $M_f = 117°C$, $A_s = 149°C$, and $A_f = 162°C$, where M_s, M_f, A_s, and A_f denote martensite start, martensite finish, austenite start, and austenite finish temperatures, respectively. Three testing temperatures were selected based on the transformation temperatures: $25°C$, $145°C$, and $180°C$. The corresponding isothermal loading paths at
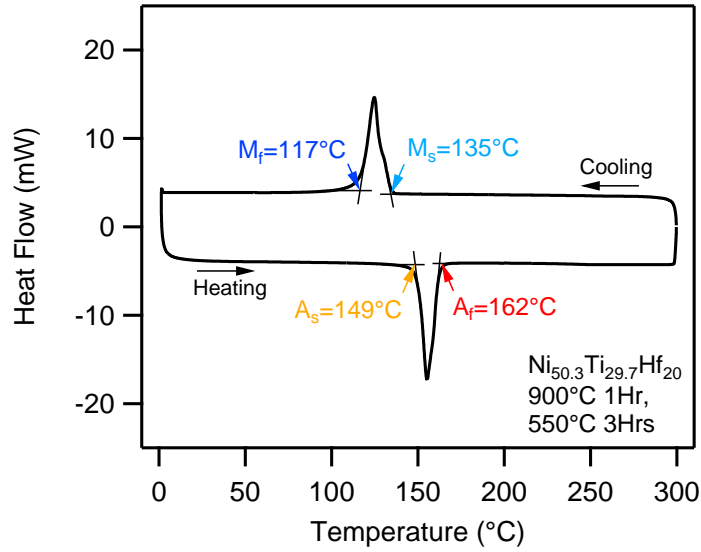
Figure 4.1: DSC curve for the solutionized and precipitation heat treated $Ni_{50.3}Ti_{29.7}Hf_{20}$. M_s, M_f, A_s, and A_f denote martensite start, martensite finish, austenite start, and austenite finish temperatures, respectively.

these three temperatures are illustrated in the schematic stress–temperature phase diagram in Figure 4.2. According to the figure, at $25°C$ self-accommodated martensite undergoes detwinning upon loading (martensitic material); at $145°C$ austenite transforms to martensite during loading with no reverse transformation upon unloading (transforming materials); at $180°C$ austenite transforms to martensite during loading and transforms back to austenite upon unloading (superelastic material). For the experiments at $145°C$, the material was first heated up to a temperature above A_f, and then cooled down to the testing temperature, to ensure the starting phase was austenite.

Uniaxial tensile characterization was carried out on a servo-hyraulic MTS machine equipped with a high-temperature MTS extensometer. Flat dog-bone specimens were pulled to failure at $25°C$, $145°C$ and $180°C$ with an engineering strain rate of $1.5 \times 10^{-4}s^{-1}$. For testing temperatures other than room temperature, the specimen was heated and cooled via thermal conduction from the grips to reach and maintain the desired temperature. Temperature was measured using a K-type thermocouple directly attached to the gauge section of the specimen.
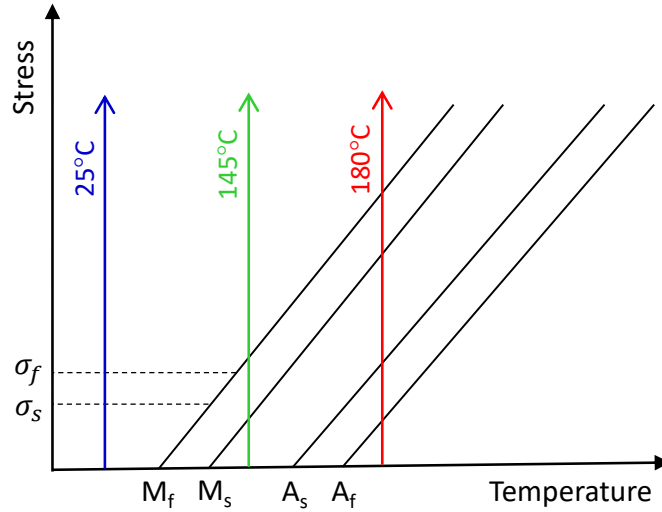
Figure 4.2: Schematic stress–temperature phase diagram showing the isothermal loading paths at 25°C, 145°C, and 180°C, resulting in martensitic, transforming, and superelastic materials, respectively.

Fracture experiments were carried out using DCT specimens with nominal dimensions of $W = 20$ mm and $B = 3$ mm, where W and B are the specimen width and thickness, respectively. Surface of the samples were first prepared by mechanical grinding using abrasive papers. Specimens were then fatigue pre-cracked on a servo-hydraulic MTS frame (MTS-810) at room temperature. The pre-cracking was performed in load control using a sinusoidal waveform and a frequency of 10 Hz with a constant load ratio, $R = P_{min}/P_{max} = 0.1$, until a crack size to width ratio a/W of ~ 0.5 was achieved. mode-I isothermal experiments were then carried out at three temperatures, 25°C, 145°C and 180°C. The specimens were pulled in displacement control with a rate of 0.4 mm/min until failure. Crack-mouth opening displacement (CMOD) was recorded using an MTS COD gauge. The temperature was monitored and controlled by averaging the readings from three K-type thermocouples, attached to different locations on the specimens. Specimens were heated via induction heating and cooled through convection cooling.

Digital image correlation (DIC) was implemented to measure full-field strain during the frac-

62

ture experiment. To this aim, the surface of the specimens were first covered with a thin layer of white paint and then black speckles were applied to generate a random pattern. Optical images were recorded at every seconds using Point Grey Grasshopper GX-FW-60S6M-C CCD camera equipped with Tokina AT-X Pro 100 mm f2.8 macro lens, resulting in an optical resolution of 0.014 mm/pixel. The DIC subset size was selected as 21x21 pixel and the step size was 3 pixels. The images were post-processed via Vic2D-6 software developed by Correlated Solutions. Rigid body motion was eliminated from DIC measurement before calculating the strains.

4.3 Results and Discussion

4.3.1 Uniaxial Tensile Characterization

Figure 4.3 shows the uniaxial stress-strain results for $Ni_{50.3}Ti_{29.7}Hf_{20}$ at three testing temperatures. Upon tensile loading at $25°C$, the self-accommodated martensite deformed in a nonlinear manner. Recognizing this nonlinearity in the stress-strain curve, an apparent Young's modulus was estimated by applying a best linear-fit through the initial loading part of curve (up to 100 MPa) to be ~ 66 GPa. Unlike binary NiTi SMAs, detwinning took place without any stress plateau or delineation of the transition between the elastic and inelastic deformation mechanisms in agreement with the published data, e.g. Ref. [87]. The specimen failed at an ultimate tensile stress of ~ 660 MPa and total elongation of ~ 2.3 %. At $145°C$, upon loading austenite deformed predominantly elastically with a Young's modulus of ~ 80 GPa. At ~ 70 MPa austenites started to transform into stress induced martensite, and an stress plateau was observed. After the plateau, the detwinned martensite deformed predominantly elastically, with possibly other deformation mechanisms in play. Finally, the sample failed at a relatively lower ultimate tensile stress (~ 400 MPa) and higher total elongation (~ 3.6 %) compared to the experiment at $25°C$. Finally, at $180°C$, the characteristics of the stress-strain response was similar to that of $145°C$, however, the stress induced transformation started at relatively higher stress value (~ 260 MPa), as one could predict from the phase diagram (Figure 4.2). The specimen failed at ~ 480 MPa after a total elongation of ~ 4.4 %. Note that at $180°C$, upon unloading at low strains (not shown in the figure), the stress-
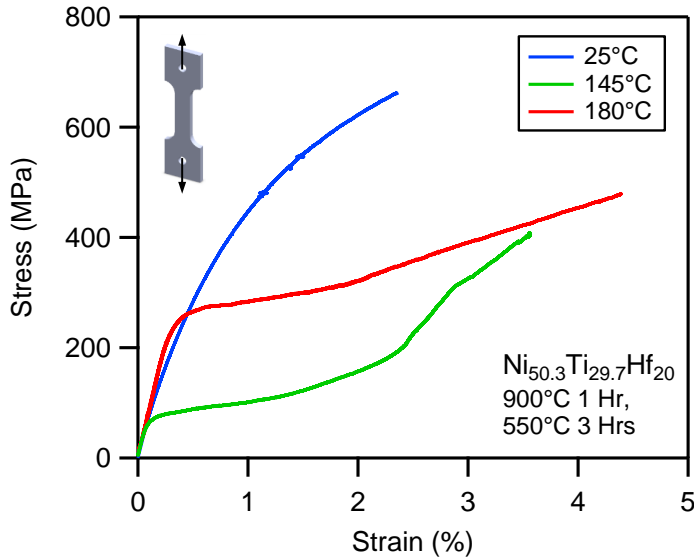
Figure 4.3: Tensile stress–strain curves for $Ni_{50.3}Ti_{29.7}Hf_{20}$ obtained from uniaxial testing of flat dog-bone specimens at $25°C$, $145°C$, and $180°C$.

induced martensite transformed back to austenite, recovering all the applied strain (superelasticty). The uniaxial tensile results are summarized in Table 4.1.

4.3.2 Fracture Toughness Measurements

Mode-I isothermal fracture experiments were performed using fatigue pre-cracked NiTiHf DCT specimens. The resulting load–displacement data at $25°C$, $145°C$, and $180°C$ are presented in Figs. 4.4a, 4.4b, and 4.4c, respectively. At all temperatures, the response was predominantly linear with very small deviations from linearity towards load maximum, followed by an abrupt load drop indicating unstable crack growth. The characteristic features of the load–displacement curves were similar to that of a brittle material, implying limited presence of dissipation mechanisms at the crack-tip. In the experiments performed at $25°C$, small load drops were observed close to the load maximum, which were followed by a sudden load drop where the crack extended unstably. After unstable crack growth, the load didn't drop to zero, and the specimen showed some load bearing capacity. This behavior was not observed in the other two testing temperatures where

Temperature (°C)	Material Properties			
	E (GPa)	σ_{cr} (MPa)	σ_{TS} (MPa)	ε_f (%)
25	66	376	662	2.3
145	80	73	409	3.6
180	83	264	479	4.4

Table 4.1: Tensile characterization results for NiTiHf dog-bone specimens tested at 25°C, 145°C, and 180°C. σ_{cr} denotes the stress required for either detwinning or transformation depending on the material state at zero load. σ_{TS}, and ε_f are stress and strain values at failure, respectively.

the load maximum was followed with an abrupt drop to zero. At 145°C, the specimens reached higher load maxima before the occurrence of unstable crack growth. Moreover, the nonlinearity in the load–displacement curves were more pronounced. Finally, at 180°C, negligible deviation from linearity was observed in the load–displacement response.

Because fracture instability was observed in all tested specimens, a single point fracture toughness value was determined from each load–displacement response. Employing the J-integral as the fracture criterion, J at the final point of instability was calculated using the formula proposed in Chapter. 2 as the sum of elastic and inelastic components

$$J = J^{el} + J^{in} = \frac{\eta^{el} A^{el}}{Bb} + \frac{\eta^{in} A^{in}}{Bb}, \tag{4.1}$$

where $b = W - a$ is the length of the unbroken ligament, A^{el} and A^{in} are the elastic and inelastic components of the area under the load–displacement curve, respectively, and η^{el} and η^{in} are geometry factors [70]. The critical J values (J_c) obtained at the three testing temperatures are presented in Figure 4.5. According to the figure, J_c of martensitic and superelastic materials are relatively close while those of transforming material are considerably higher. The transforming material owes the higher J_c to the higher maximum attained load and more pronounced nonlinearity in the load–displacement response. As discussed in Refs. [25, 88], this is because the transformation acts as a toughening mechanism and can dissipate certain amount of energy that otherwise would be available for crack extension. The material tested at 180°C, however, has a lower J_c because it
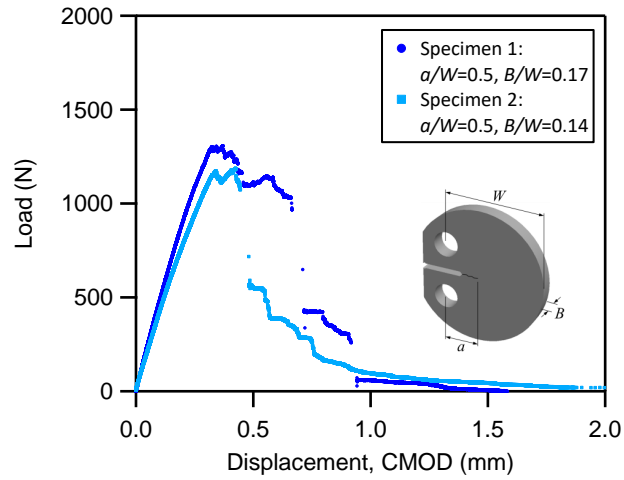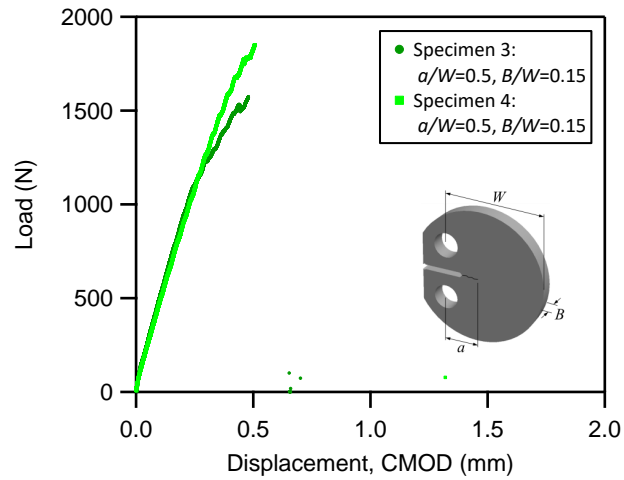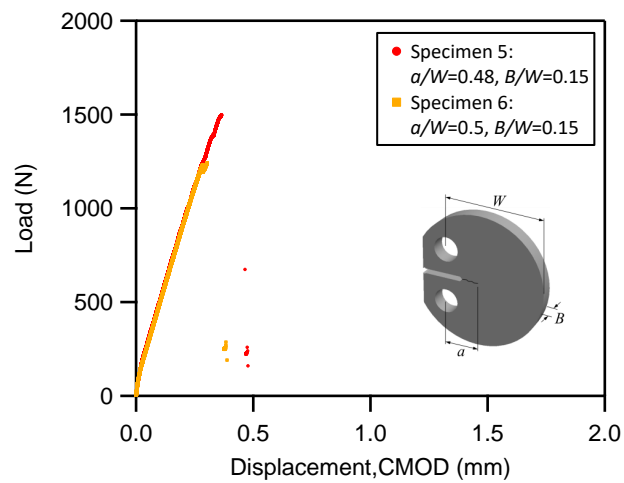
Figure 4.4: Load–displacement curves for fatigue pre-cracked $Ni_{50.3}Ti_{29.7}Hf_{20}$ DCT specimen tested in mode-I at: (a) $25°C$; (b) $145°C$; and (c) $180°C$.

showed insignificant deviation from linearity. Although at 180°C the material undergoes phase transformation upon loading, the transformation starts at a much higher stress value compared to the material tested at 145°C, as can be seen from the stress–strain curves in Figure 4.3 and σ_{cr} values in Table 4.1. This limits the ability of the material to dissipate energy through phase transformation.

According to ASTM E1820 [71] for the critical J values reported here to be qualified as a geometry-independent fracture toughness value, the thickness and unbroken ligament requirements given by $B, b \geq 100 J_c / \sigma_Y$ should be met. In this formula σ_Y is referred to as the effective yield strength, and for the conventional elastoplastic materials is defined as the average of 0.2% yield stress and the ultimate tensile strength. In the case of SMAs, the critical stress at the onset of transformation/detwinning, σ_{cr}, is more suitable to be used instead. The requirement for the unbroken ligament is satisfied for all the specimens tested here. This is not the case for the thickness requirement, for which specimens with thicknesses as high as ~ 12 mm is required. However, as discussed in Chapter 3, the thickness requirement for SMAs is not expected to be as stringent as that of conventional ductile materials because SMAs fail predominantly by cleavage fracture [89, 90], and crack tunneling and shear lip formation has not been evident in SMAs. Further studies on the effect of specimen thickness on fracture toughness of SMAs are currently under way.

For comparison purposes, the extrapolated average K_{J_c} values are plotted in Figure 4.6 together with the critical stress intensity factors, K_c, obtained from linear elastic fracture mechanics (LEFM). K_{J_c} values are calculated using J_c values as

$$K_{J_C} = \sqrt{E\,J_c,} \tag{4.2}$$

where E corresponds to the stable phase at the testing temperature. K_c values are calculated as

$$K_c = \frac{P_c}{B\sqrt{W}}\, f\left(\frac{a}{W}\right), \tag{4.3}$$

where P_c is the load at the point of instability and $f(a/W)$ is a shape function, given in ASTM
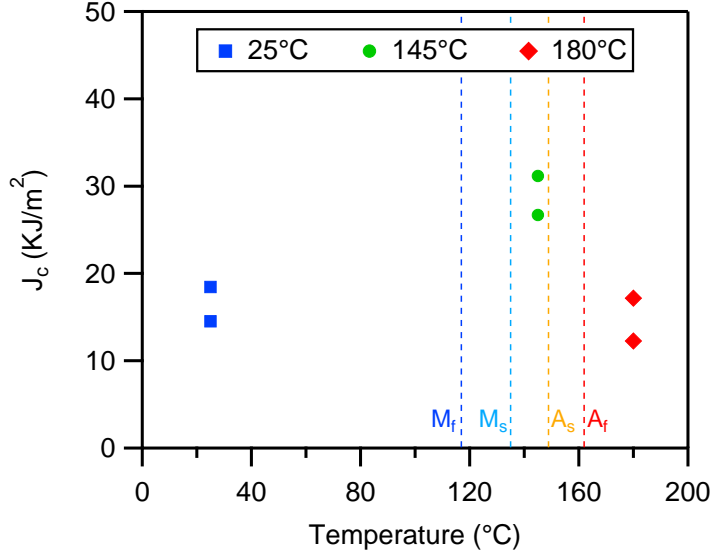
Figure 4.5: J_c values for NiTiHf DCT specimens tested at $25°C$, $145°C$, and $180°C$. The transformation temperatures are shown with dashed lines. The values corresponding to martensite and superelastic materials are relatively close while the fracture toughness of transforming material is considerably higher.

E399 [30] for DCT specimen as

$$f\left(\frac{a}{W}\right) = \frac{2 + \left(\frac{a}{W}\right)\left[0.76 + 4.8\left(\frac{a}{W}\right) - 11.58\left(\frac{a}{W}\right)^2 + 11.43\left(\frac{a}{W}\right)^3 - 4.08\left(\frac{a}{W}\right)^4\right]}{\left(1 - \frac{a}{W}\right)^{\frac{3}{2}}}. \quad (4.4)$$

It can be seen that at all testing temperatures, the K_{J_c} values are higher than the corresponding K_c values. This is because K_{J_c} takes into account the load–displacement response, while K_c only uses the load value and the specimen dimensions. However, because the nonlinearity in the load–displacement response was limited, the difference between K_{J_c} and K_c values is small, with the smallest difference at $180°C$, at which the nonlinearity in the load–displacement response was the least. Moreover, in a similar trend to the J_c values, the highest fracture toughness was observed at $145°C$. The relative increase in the fracture toughness values at $180°C$ compared to $25°C$ is due to the relatively higher elastic modulus. The values for all measured critical parameters are tabulated in Table 4.2.
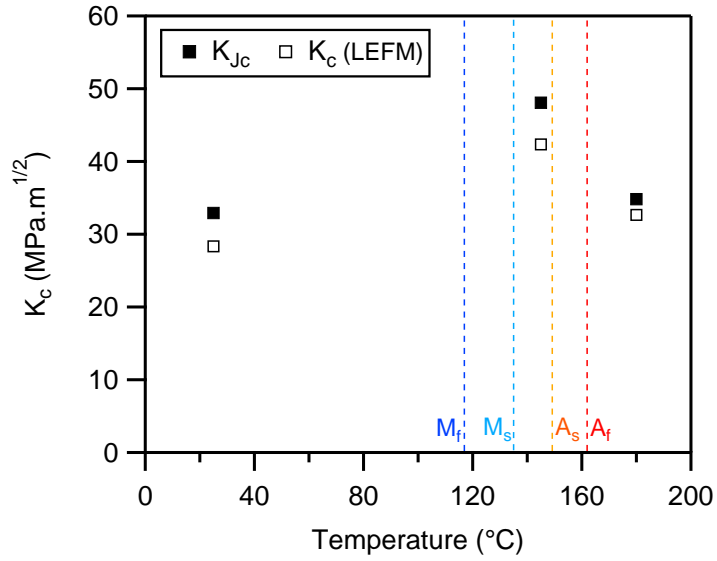
Figure 4.6: Average K_{Jc} and K_c values for NiTiHf DCT specimens tested at $25°C$, $145°C$, and $180°C$. K_{Jc} and K_c values were obtained using Eqs. (4.2) and (4.3), respectively. The transformation temperatures are shown with dashed lines.

Specimen	Temperature (°C)	Fracture Toughness		
		J_c (KJ/m^2)	K_{Jc} (MPa$\sqrt{m}$)	K_c (MPa$\sqrt{m}$)
1	25	14.5	30.9	27.4
2	25	18.4	34.9	29.3
3	145	26.7	46.2	38.6
4	145	31.2	49.9	46.1
5	180	17.2	37.7	34.8
6	180	12.3	31.9	30.5

Table 4.2: Critical fracture parameters for NiTiHf DCT specimens tested at $25°C$, $145°C$, and $180°C$.
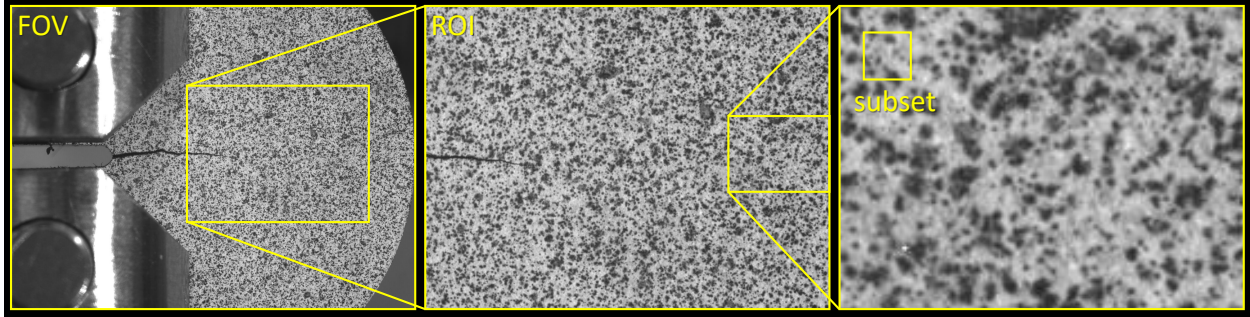
Figure 4.7: Surface of the DCT specimen showing the speckle pattern, field of view (FOV), region of interest (ROI), and subset used for DIC analysis.

4.3.3 Full-field Strain Measurements

DIC was implemented to measure the full-field strains near the crack-tip. Figure 4.7 shows the surface of the DCT specimen with the speckle pattern, field of view (FOV), region of interest (ROI), and subset used for DIC analysis. Strains along the direction normal to the crack line (ε_{yy}) at the point of instability at $25°C$, $145°C$, and $180°C$ are shown in Figs. 4.8a, 4.8b, and 4.8c, respectively. At all temperatures, strain accumulated symmetrically with respect to the crack line and along two lobes on each side of it. It can be seen that even at the maximum load, the generated strains are relatively small in magnitude, and non-zero strains are confined to the crack-tip region, which indicates that the zone of non-linear deformation, i.e. detwinning/transformaiton, is small compared to the crack configuration (small-scale yielding, SSY). The limited presence of dissipation mechanisms acting near the crack-tip explains the predominantly linear load–displacement response, and the unstable crack growth observed at all temperatures. No significant difference was observed between the strain maps at different testing temperatures.

4.3.4 Comparison: NiTiHf vs. NiTi

To further understand the fracture behavior of NiTiHf, this section compares the results for martensitic NiTi and NiTiHf specimens. For the sake of brevity, for each material, results from a single experiment at $25°C$ are presented. For both materials, this temperature is below M_f and

70
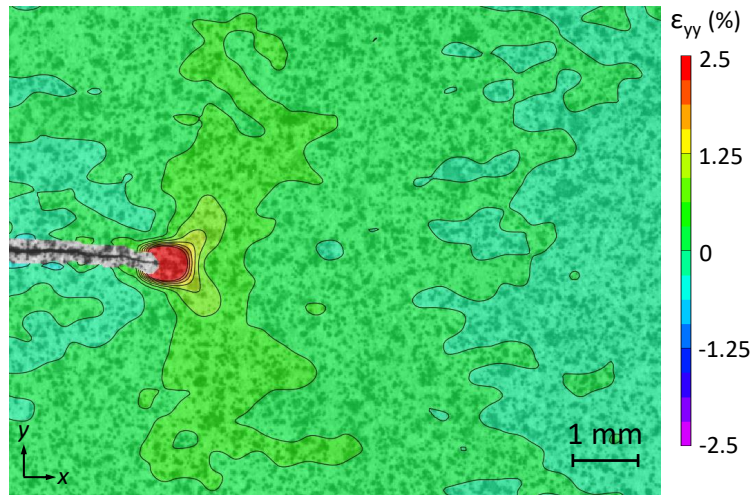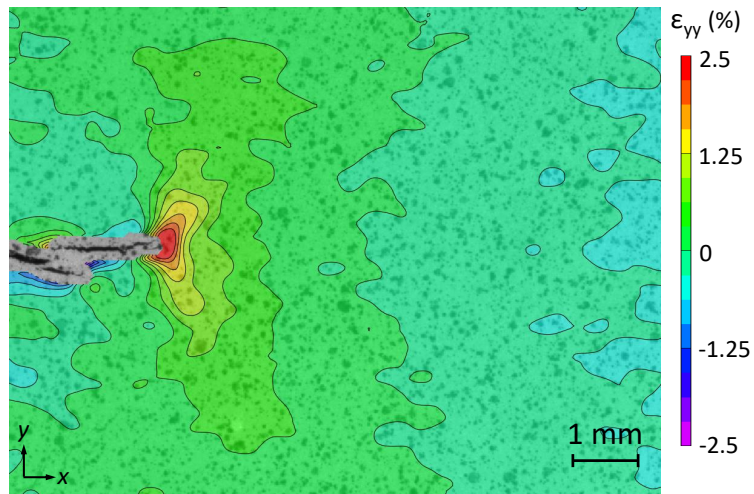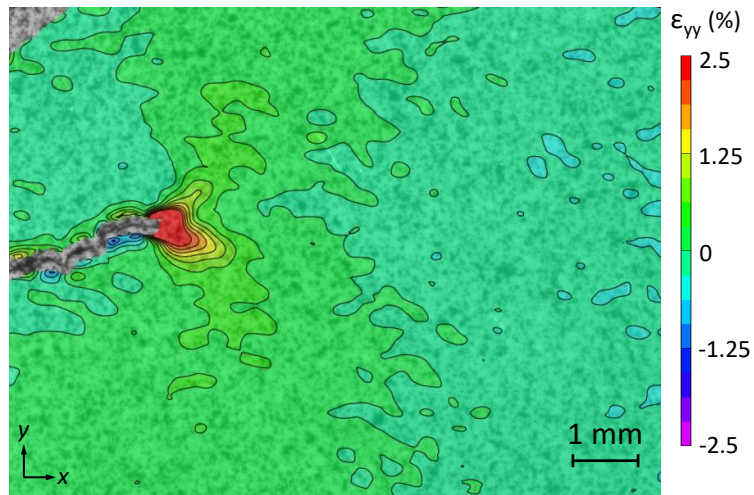
Figure 4.8: DIC strain maps at the point of instability near the crack-tip of $Ni_{50.3}Ti_{29.7}Hf_{20}$ DCT specimen tested in mode-I at: (a) $25°C$; (b) $145°C$; and (c) $180°C$.
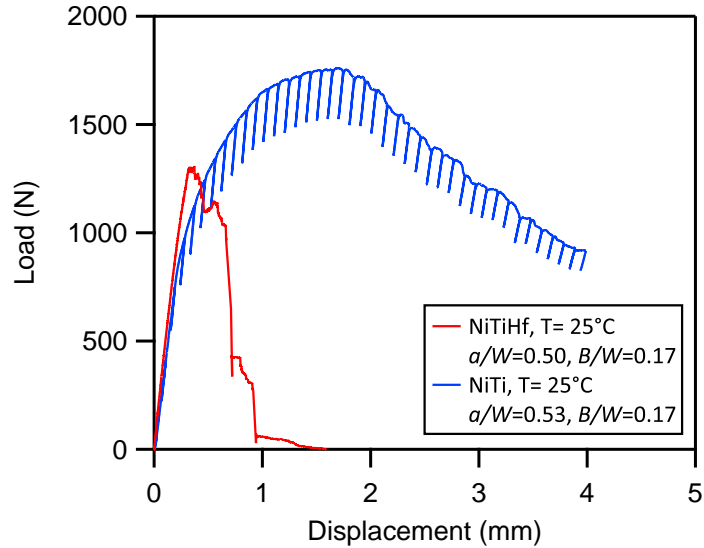
Figure 4.9: Load–displacement curves for $Ni_{50.3}Ti_{29.7}Hf_{20}$ DCT specimen and $Ni_{49.5}Ti_{50.5}$ CT specimen tested in mode-I at $25°C$.

therefore the stable phase is martensite. Figure 4.9 plots the corresponding load–displacement data. Note that the thickness of the two specimens is approximately the same and the initial crack size is slightly larger for NiTi specimen. Upon loading up to ~ 800 N, the response of the two materials are similar and the curves are behaving in a linear manner. This is because the deformation is predominantly elastic in both cases. After ~ 800 N, however, the curve corresponding to NiTi starts deviating from linearity and reaches its maximum at ~ 1700 N. Meanwhile, the curve corresponding to NiTi continues in an elastic manner until ~ 1300 N. After reaching its maximum, load drops gradually in NiTi specimen indicating stable crack growth. In NiTiHf specimen, the abrupt load drop after maximum indicates unstable crack growth. The significant difference in the load–displacement curves has roots in the difference in the ability of these two materials to dissipate energy through detwinning/plasticity.

Strain (ε_{yy}) contour plots corresponding to the maximum load for NiTiHf and NiTi specimens are presented in Figs. 4.10a and 4.10b, respectively. For ease of comparison, both plots share the same color bar. Comparing the two plots, one can see the origin of the difference observed in
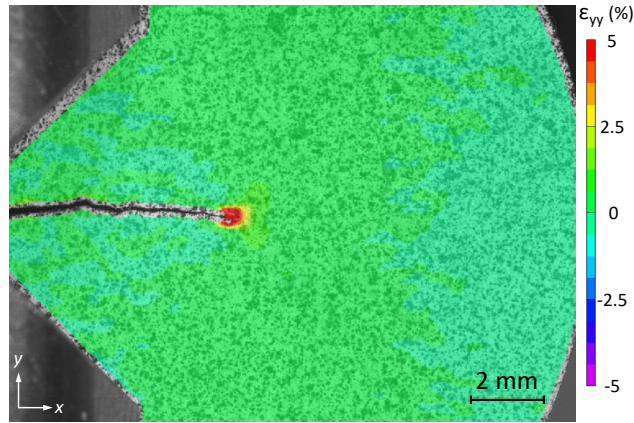
(a)
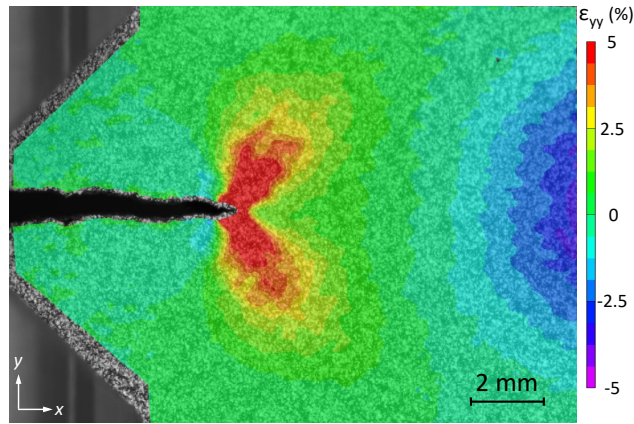
(b)

Figure 4.10: Strain (ε_{yy}) contour plots corresponding to the maximum load for (a) $\text{Ni}_{50.3}\text{Ti}_{29.7}\text{Hf}_{20}$ DCT specimen, and (b) $\text{Ni}_{49.5}\text{Ti}_{50.5}$ CT specimen, both tested at room temperature.

the load–displacement curves in Figure 4.9. In NiTi specimen the red region, representing strains up to 5%, extends well beyond the crack-tip. The increase in displacement resulted in expanding this region. In NiTiHf specimen, however, this region is limited only to the crack-tip, and further increase in displacement resulted in unstable crack growth. At the other end of the NiTi specimen, the metrical underwent large compressive strains. Such compressive strains were absent in NiTiHf specimen.

The fracture surfaces were investigated using a Tescan LYRA-3 Scanning Electron Microscope (SEM). The micrographs of NiTiHf and NiTi specimens, tested at room temperature, are presented in Figs. 4.11a, and 4.11b, respectively. The micrographs show transgranular fracture mode in
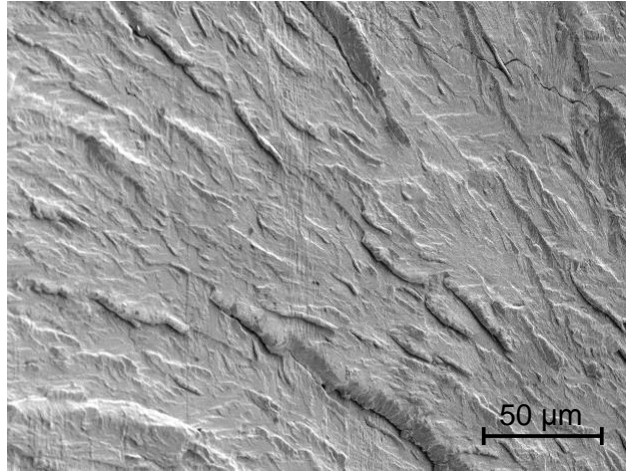
(a)
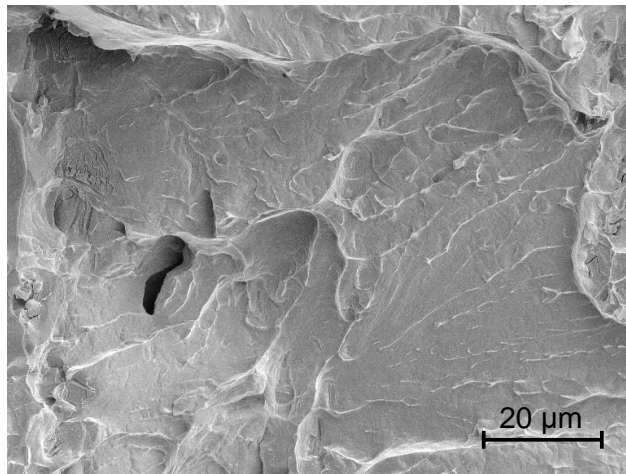
(b)

Figure 4.11: Scanning electron microscopy (SEM) images of the fracture surface of (a) $Ni_{50.3}Ti_{29.7}Hf_{20}$ DCT specimen, and (b) $Ni_{49.5}Ti_{50.5}$ CT specimen, both tested at room temperature.

both materials. Brittle fracture pattern prevails throughout the fracture surface of NiTiHf, and the cleavage facets are notable. The brittle pattern of fracture surface is consistent with the load–displacement curve (Figure 4.9) and DIC results (Figure 4.10a). For NiTi, the presence of river marks and dimples indicate that cleavage fracture and ductile tearing acted in conjunction. This is in agreement with previous observations on NiTi SMAs (Ref. [89]).

4.4 Summary

Fracture behavior of a Ni-rich $Ni_{50.3}Ti_{29.7}Hf_{20}$ high-temperature shape memory alloy under mode-I isothermal loading was examined at three temperatures: $25°C$, $145°C$, and $180°C$. At these temperatures, self-accommodated martensite undergoes detwinning upon loading (martensitic material), austenite transforms to martensite during loading with no reverse transformation upon unloading (transforming materials), and austenite transforms to martensite during loading and transforms back to austenite upon unloading (superelastic material), respectively. Unstable crack growth was observed at all testing temperatures. The load–displacement curves were obtained and the critical J-integral values (J_c) were calculated. The specimens tested at $145°C$ showed the highest resistance to crack growth. This is because at this temperature the material at the crack-tip can transform at a relatively low stress value and therefore dissipate more energy through phase transformation compared to the specimens tested at $180°C$ where the transformation starts at a much higher stress value. The strain field on the surface and near the crack-tip was measured using DIC. Strain contour plots showed limited extent of dissipation mechanisms acting near the crack-tip at all testing temperatures.

5. FINITE ELEMENT MODELING OF ACTUATION CRACK GROWTH IN NiTiHf HIGH TEMPERATURE SHAPE MEMORY ALLOYS

5.1 Introduction

In this chapter, an SMA constitutive model is implemented to investigate crack growth under actuation loading in a disk-shaped compact tension (DCT) specimen. The model parameters are calibrated using uniaxial tensile experiments on a NiTiHf high temperature SMA. The virtual crack closure technique (VCCT) is employed as the crack propagation criterion and the critical crack growth parameters is adopted from fracture toughness measurements on the same material system. The chapter is organized as follows: Section 5.2 presents the experimental procedure to calibrate the material parameters. Section 5.3 describes the finite element boundary value problem. Section 5.4 presents and discusses the crack growth results. Section 5.5 concludes the chapter by summarizing the key findings.

5.2 Model Calibration

The constitutive model for polycrystalline SMAs, developed by Lagoudas et al. [83], and described in Chapter 3 is adopted. The key material parameters that are used to calibrate the model are: the elastic modulus of austenite and martensite, E_A and E_M; Poisson's ratio of austenite and martensite, ν_A and ν_M; the parameters for $H^{cur}(\bar{\sigma})$ in Equation (3.4), i.e. k and H_{sat}; transformation temperatures at zero load, *i.e.*, austenite start A_s, austenite finish A_f, martensite start M_s and martensite finish M_f; and austenite and martensite stress–temperature slopes, C_A, and C_M.

To calibrate the model, uniaxial tensile experiments were carried out using $Ni_{50.3}Ti_{29.7}Hf_{20}$ (at. %) flat dog-bone specimens. To measure the elastic moduli, E_A and E_M, the temperature was fixed at $180°C$ (above A_f). The specimen was then loaded to $\sim 2.5\%$ strain and unloaded to zero load uwith an engineering strain rate of $1.5 \times 10^{-4} s^{-1}$. The corresponding stress–strain response is shown in Figure 6.5a. E_A and E_M are obtained from the initial part of loading and unloading, respectively, as shown in the figure.
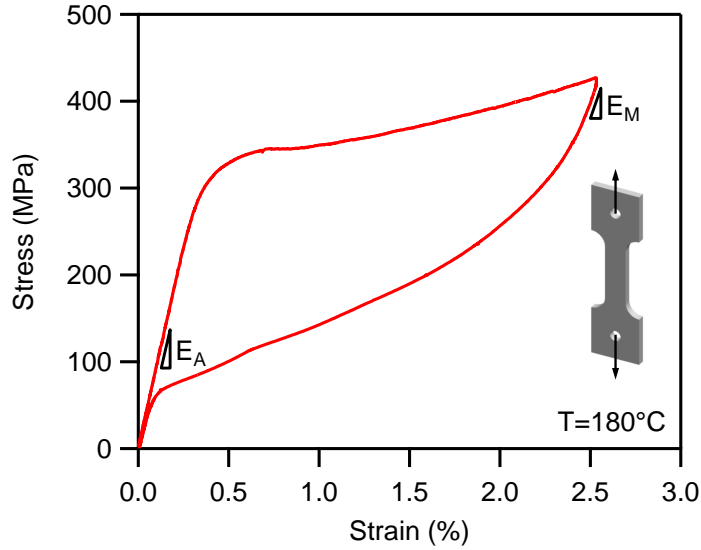
Figure 5.1: Uniaxial tensile experiment results for NiTiHf under mechanical loading at $T = 180°$C.

To obtain the phase transformation characteristics, the specimen was loaded to various bias load levels (50 MPa–400 MPa), and then thermally cycled between $80°$C and $340°$C with a rate of $10°$C/min. The strain–temperature results are presented in Figure 5.2a. The critical transformation temperatures for start and finish of the forward and reverse phase transformation are determined for each stress level as illustrated in Figure5.2b. The critical temperatures are then used to generate stress–temperature phase diagram, as shown in Figure 5.3, from which austenite and martensite stress–temperature slopes, C_A and C_M, are obtained. The maximum transformation strain, $H^{cur}(\sigma)$ generated under each uniaxial stress level is measured as shown in Figure 5.2b, and is plotted as a function of applied stress value. This is presented in Figure 5.4 where the tendency of $H^{cur}(\sigma)$ to saturate with increasing applied stress level is demonstrated with an exponential fit. The material properties obtained from characterization tests are tabulated in Table 5.1.

Using the material parameters presented in Table 5.1, the strain–temperature response is calculated by performing isobaric tensile simulations in Abaqus. Figs. 5.5a–5.5f respectively shows the results for the stress values 50–400 MPa. The experimental data from NiTiHf (Fig 5.2a) are
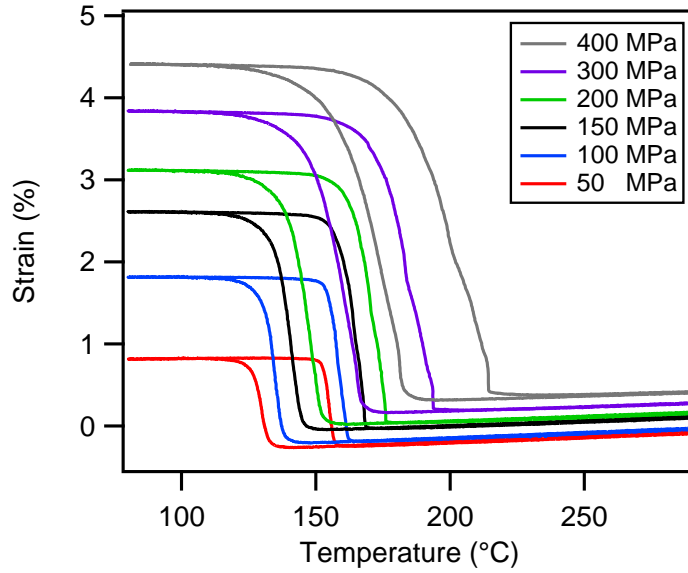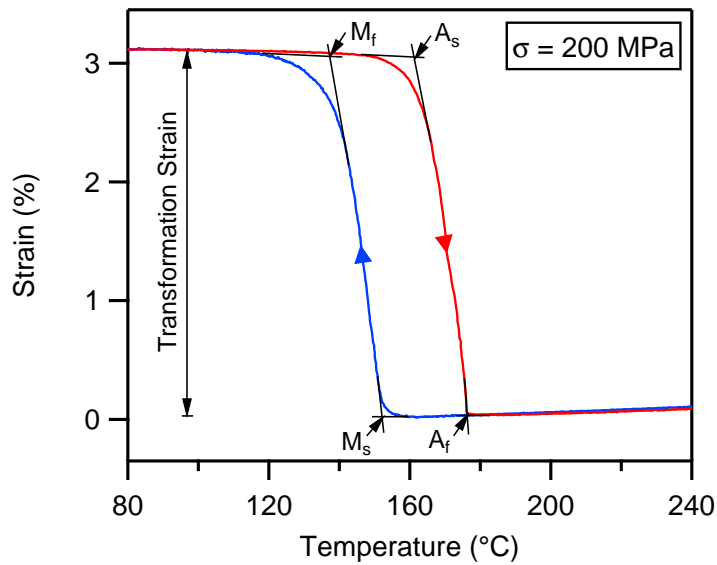
Figure 5.2: (a) Strain–temperature response of NiTiHf under isobaric tensile experiment at various applied stress levels; (b) Strain–temperature response at $\sigma = 200$ MPa, and how the phase transformation characteristics are obtained from a heating–cooling cycle.
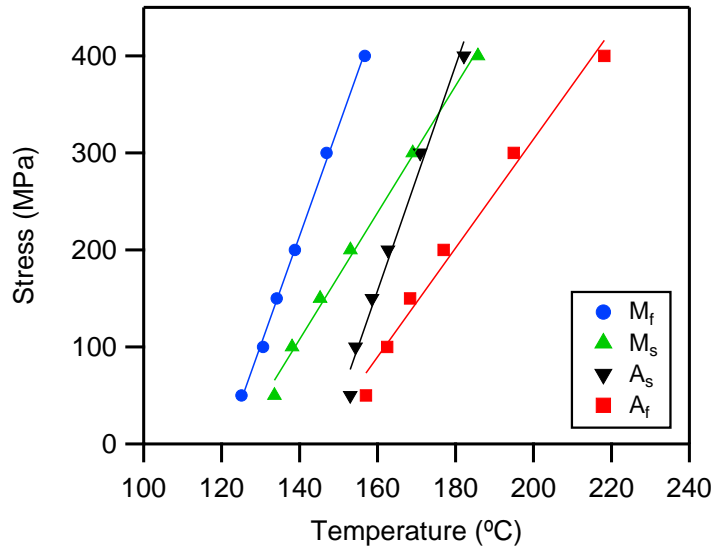
Figure 5.3: Stress-temperature phase diagram for NiTiHf obtained by measuring transformation temperatures at various applied stress levels.
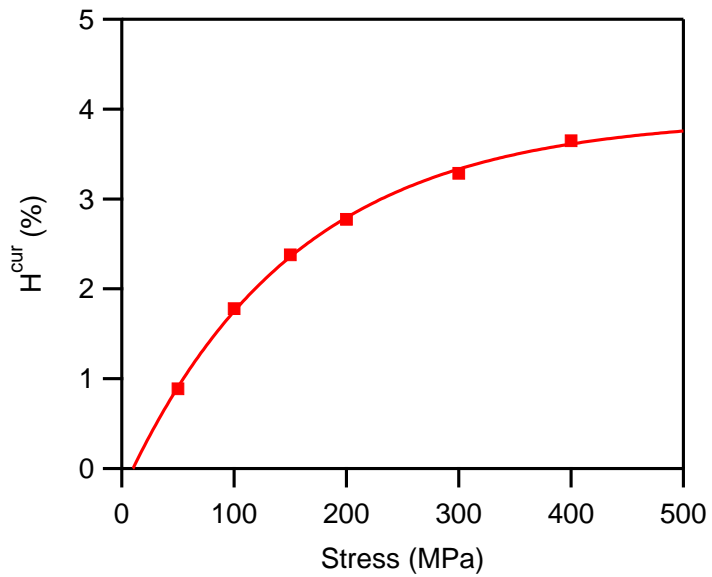
Figure 5.4: Saturation of maximum transformation strain, $H^{cur}(\sigma)$, with increasing applied stress level.

Parameter	Value	Parameter	Value
E_A	90 GPa	M_s	135°C
E_M	62 GPa	M_f	115°C
ν_A	0.33	A_s	149°C
ν_M	0.33	A_f	162°C
H_{sat}	4.1 %	C_A	8 MPa/°C
k	0.006 MPa^{-1}	C_M	8.8 MPa/°C

Table 5.1: Material parameters used in finite element simulations. The parameters are calibrated based on the uniaxial tensile experiments on NiTiHf doge-bone specimens under mechanical and actuation loading.

also plotted for each stress level for comparison. According to the figures, a good agreement is observed between the FEA results and experimental data in terms of transformation characteristics, especially for the stress values 100–300 MPa. At 50 MPa the model slightly overpredicts the transformation strain, and at 400 MPa the model is not able to capture the change in the hardening behavior of the experiential results.

5.3 Problem Formulation

A three-dimensional (3D) finite element boundary value problem of a DCT specimen is set up in Abaqus finite element analysis (FEA) suite (Figure 5.6a). The geometry of the model is identical to that of a NiTiHf DCT specimen that was experimentally investigated. The material model described in Chapter 3 is implemented in the Abaqus implicit finite element solver using a user-defined material subroutine (UMAT). A pre-crack, represented by "unbonded" nodes, is introduced that simulates the fatigue pre-crack in a typical crack growth experiment. To mimic a mode-I experiment, displacement in the top pin hole is pinned (rotation is allowed) while load is applied in the y direction at the bottom pin hole (Figure 5.6a). The crack path is assumed to grow orthogonal to loading direction (mode-I). Eight-node linear brick hexahedral elements with reduced integration (C3D8R) are used. A total of 73512 elements are employed in the finite element model and mesh is highly refined along the crack line to accurately capture the near-tip fields as shown in Figure 5.6a.
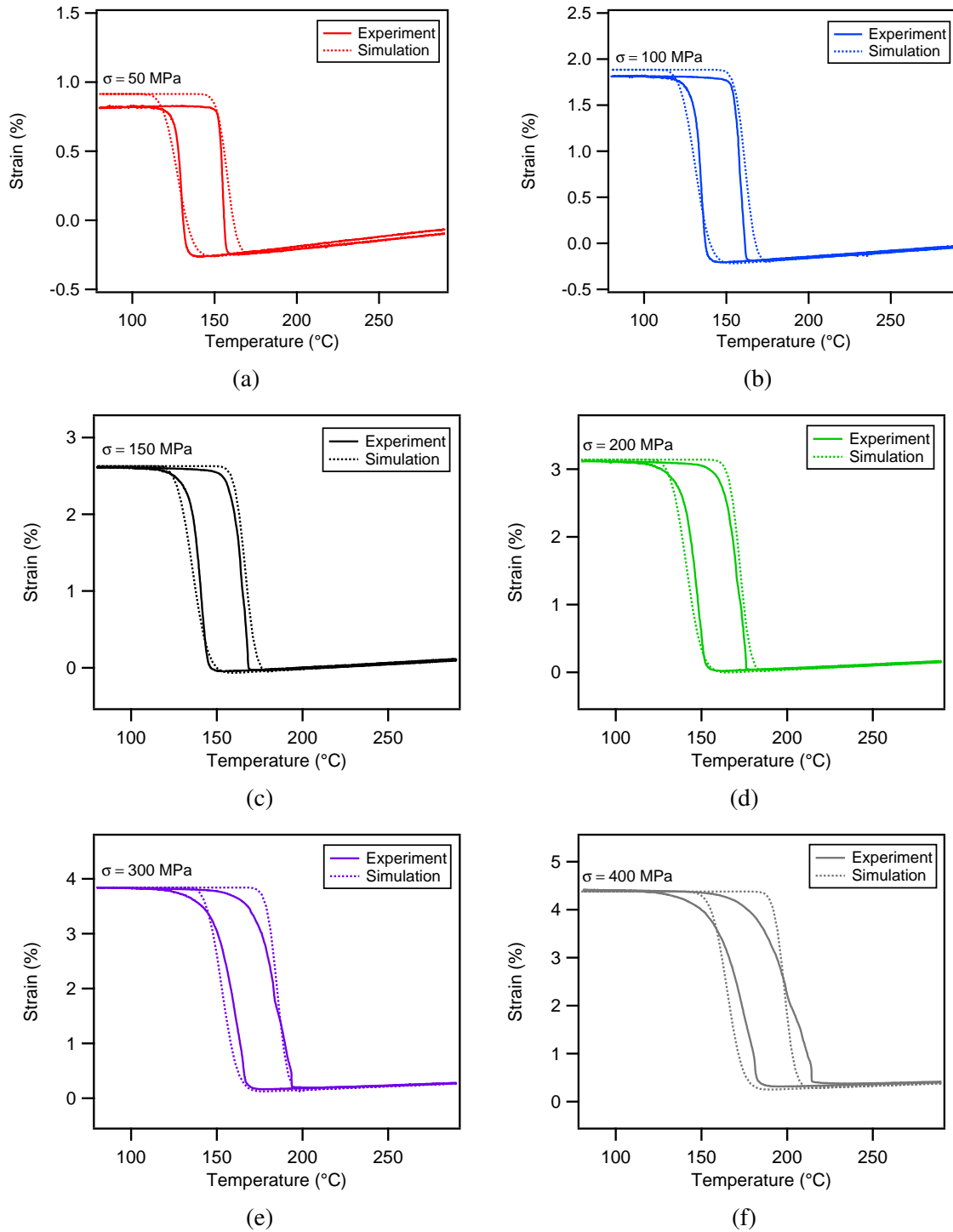
Figure 5.5: Comparison of strain–temperature response obtained from isobaric tensile experiments on NiTiHf, and finite element simulations using the material parameters in Table 5.1 at various applied stress levels: (a) 50, (b) 100, (c) 150, (d) 200, (e) 300, and (f) 400 MPa.

VCCT is implemented for its calculation where the crack tip energy release rate, G, is used as the driving force for crack growth. VCCT assumes: (i) the energy released in the process of a certain amount of crack extension is equal to the energy required to close the crack by the same amount, and (ii) there is no significant change in the state of the crack tip as it advances from a to $a + \Delta a$. Debonding occurs when $G = G_c$, where G_c is the critical energy release rate. Considering the presence of martensite at the crack tip during crack extension, the critical energy release rate is assumed to be equal to the fracture toughness of martensite (Chapter 4). Figure 5.6b demonstrates VCCT for eight-noded 3D solid elements. For the elements placed in the crack front, the mode-I energy release rate, G_I, is computed as

$$G_I = -\frac{1}{2\Delta S} P^i (v^l - v^{l^*}).$$

(5.1)

Here $\Delta AS = \Delta ad$ is the area virtually closed where Δa is the length of the elements at the crack front, and d is the width of the elements. P^i is the nodal force at the crack tip and perpendicular to the crack plane, and v^l and v^{l^*} denote the opening displacement of the upper and lower crack surfaces, respectively (Figure 5.6b).

The imposed boundary conditions are adopted from the actuation crack growth experiment on the NiTiHf DCT specimen. A uniform temperature field ($T = 200°$C) is prescribed at every material point. This temperature is well above A_f and therefore ensures that the material is in austenitic phase. A constant bias load ($P_{bias} = 545$ N) is applied at the bottom pin hole. Following the application of the load, the specimen is subjected to thermal cycling between the upper cycle temperature, UCT=200°C and the lower cycle temperature, LCT=75°C. Thermal cycling is repeated between UCT and LCT until failure. Assuming elastically deforming martensite at the crack tip, the critical energy release rate is set to be equal to fracture toughness J_c of NiTiHf at martensitic state.
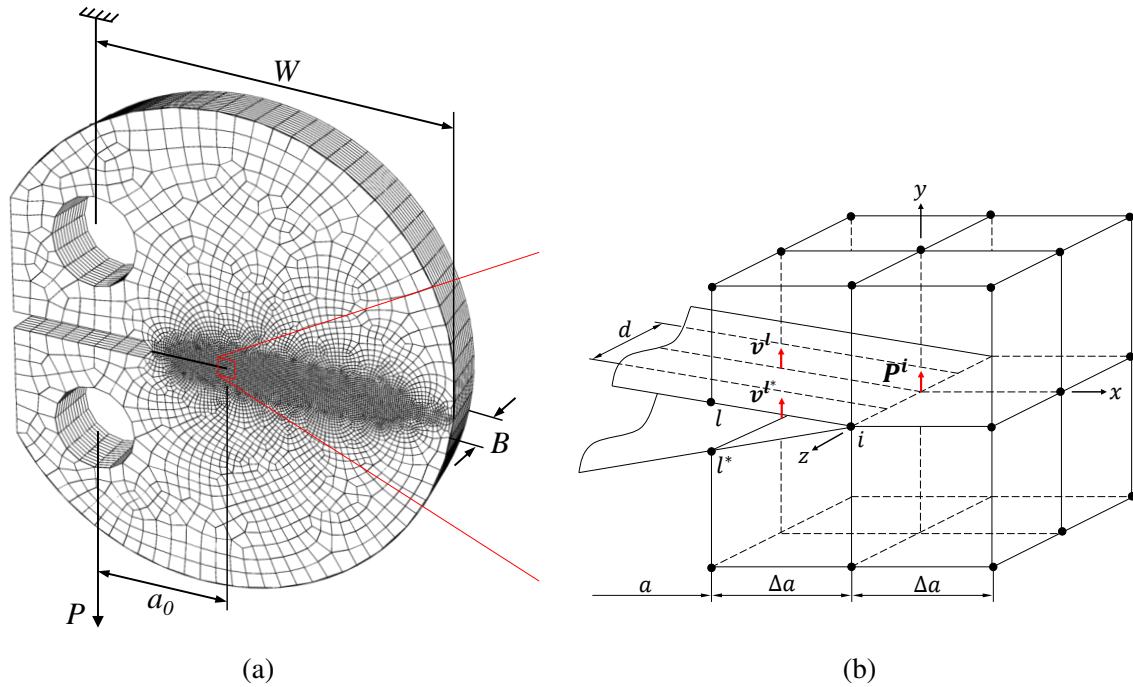
Figure 5.6: (a) Finite element boundary value problem and the mesh geometry. $P_{bias} = 545$ N, $W = 20$ mm, $a_0/W = 0.27$, $B/W = 0.14$; (b) 3D virtual crack closure technique for eight-node three-dimensional solid elements.

5.4 Results and Discussion

5.4.1 Crack Extension vs. Actuation Cycle

Crack extension, $\Delta a = a - a_0$, with respect to the actuation cycle number obtained from FEA under applied bias load of $P_{bias} = 545$ N is plotted in Figure 5.7a. At this applied load, the specimen completes 30 actuation cycle before it fails during the subsequent cycle. The majority of the crack extension is linear, with a nonlinearity occurring at the very end, which corresponds to unstable crack growth and ultimate failure. To illustrate the importance of selecting the proper critical crack growth parameter, another simulation is carried out using the same geometry, material parameters, and boundary conditions, but with a different critical energy release rate, G_c. This time, instead of using J_c, the critical parameter is calculated using $G_c = K_c^2/E$ where K_c is the experimentally determined critical stress intensity factor, obtained by linear elastic fracture mechanics (LEFM). The result is shown in Figure 5.7b, together with the experimental data obtained

from the same actuation crack growth experiment which is used for model geometry and boundary conditions. According to the figure, the experimental data and simulation results match very well in terms of the actuation crack growth rate and total cycles to failure when J_c is used as the critical energy release rate. However, the agreement is poor when $G_c = K_c^2/E$ is adopted.

5.4.2 Displacement–Temperature Response

Figure 5.8 plots the displacement–temperature results of the actuation crack growth simulation for the DCT specimen under an applied bias load of $P_{bias} = 545$ N. The displacement is obtained from the crack mouth (CMOD) in the loading direction. According to the figure, the specimen completes 30 actuation cycle and then fails in the subsequent cycle during cooling. In all actuation cycles the crack growth occurs during cooling when the material undergoes phase transformation from austenite to martensite. This is in agreement with previous results obtained from a 2D center-cracked infinite NiTi SMA plate crack [56, 57], in which the increase in the crack tip energy release rate during forward transformation is cited as the reason behind this observation. The results shown here explain that the increase in the energy release rate is because of the generated displacement during transformation. Basically, in Equation (C.1) the opening displacement of the crack faces, $v^l - v^{l*}$, is the reason for the reported increase. It can be seen from the figure that the displacement increases with number of cycles. This is because of the crack growth in each cycle that leads to a larger generated displacement under the same applied load during the subsequent cycle. Moreover, the critical temperatures for crack extension increase with number of cycles. This can be attributed to the larger initial crack size resulting from the crack growth during previous cycle, and consequently higher stresses at the crack tip.

The numerical displacement–temperature results for the last cycle before failure is plotted in Figure 5.9. According to the figure, at $137°$ C, the displacement starts to increase during cooling when the material undergoes forward phase transformation until $117°$ C, after which the displacement change, if any, is only limited to the thermal expansion. During heating, the displacement starts to decrease at $150°$ C while the material undergoes reverse transformation. When the temperature reaches $165°$ C, there is no further change in displacement with heating. At the end of
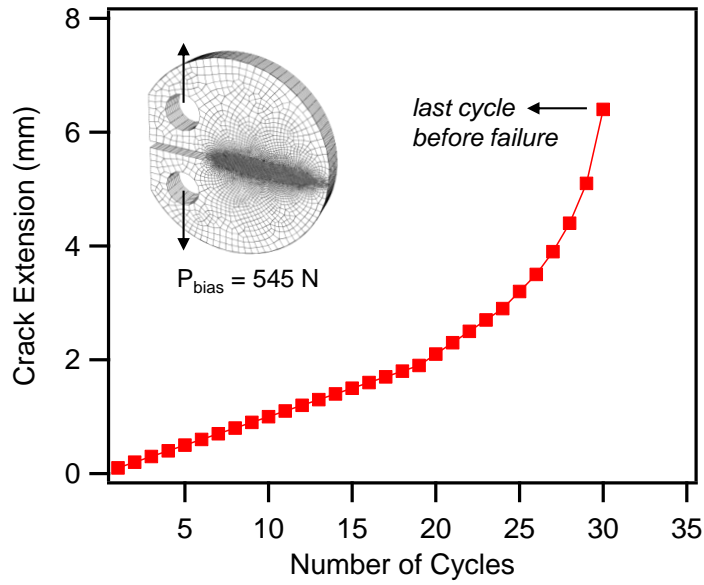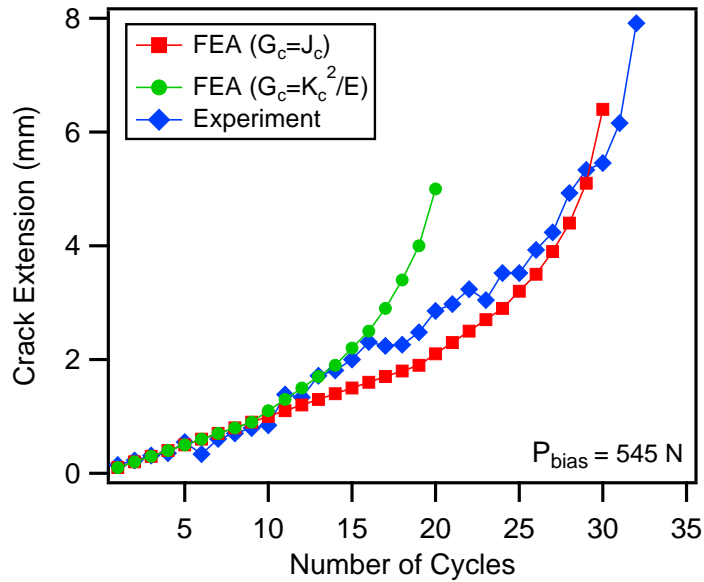
Figure 5.7: Crack extension with respect to actuation cycle number under an applied bias load $P_{bias} = 545$ N: (a) FEA results for NiTiHf DCT model showing crack growth through multiple cycles; (b) comparison with with the experimental data shows a good agreement when J_c is used as the critical energy release rate. The agreement is poor when $G_c = K^2/E$ is adopted.
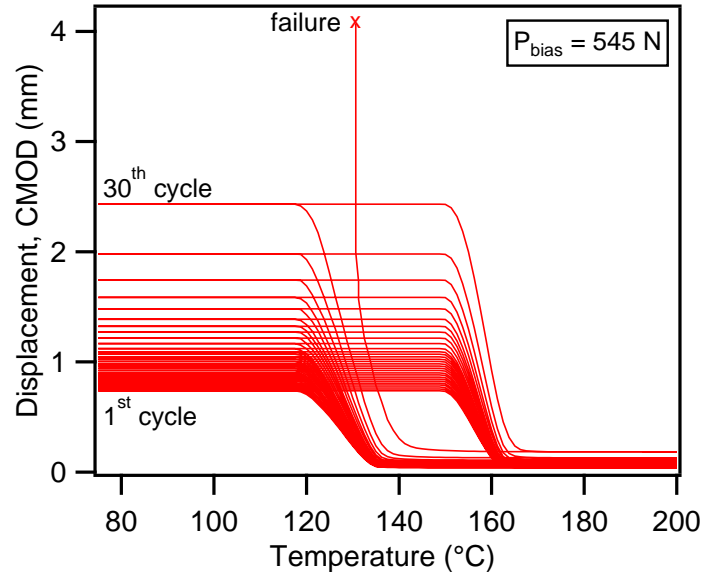
Figure 5.8: Numerical displacement-temperature response of the DCT model under an applied bias load $P_{bias} = 545$ N for all actuation cycles until failure.

the actuation cycle, the displacement is slightly larger than the displacement at the beginning of the cycle, leading to an unrecovered displacement. As mentioned earlier, the crack size at the end of the cycle is larger than that at the beginning, therefore, under the same applied load the crack mouth displacement is larger. The numbers labeled on the plot refers to the points for which the evolution of transformation is investigated in the next section.

5.4.3 Evolution of Transformation during Actuation Cycle

The evolution of martensite volume fraction, ξ, on the surface of the DCT specimen for the actuation crack growth cycle of Figure 5.9 at the labeled points is shown in Figure 5.10. The color bar is set so that dark blue represents the untransformed region, red represents the fully transformed region, and the colors in between represents transforming region. Cooling from a fully austenitic phase, at Point 1, the majority of the specimen is untransformed, and a small area at the crack-tip starts to transform to martensite. The transformation occurs first in front of the crack tip where the stresses are higher, which agrees with the phase diagram (Figure 5.3). At

86
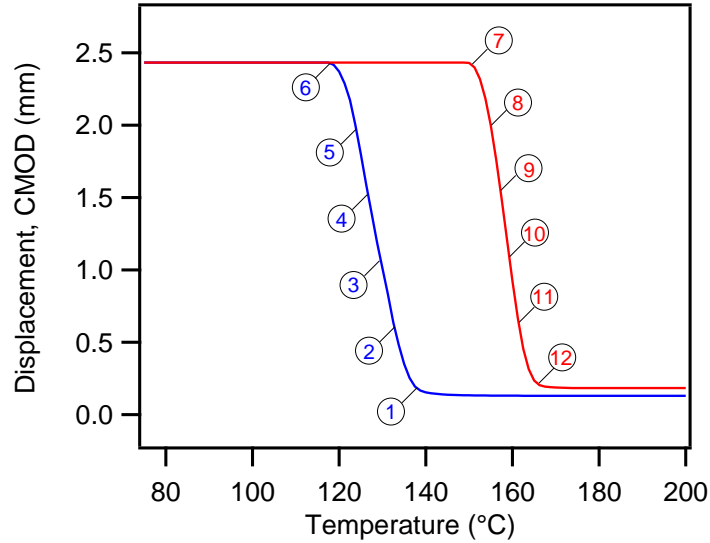
Figure 5.9: Numerical displacement-temperature response of the DCT model under an applied bias load $P_{bias} = 545$ N for the last actuation cycle before failure (30th cycle).

Point 2, the transformation zone becomes larger and a fully transformed region appears at the crack tip. The other end of the specimen also starts to transform under compression. At Point 3, the entire specimen is transforming (no dark blue color), and the crack grows into a zone of fully transformed martensite, which has grown larger around the crack tip. At Point 4, the fully transformed martensite is extended further, and starts to appear at the other end of the specimen. At Point 5, the fully transformed martensite is reached to the specimen boundaries. The specimen is fully martensite at Point 6 and the crack growth is stopped. During heating, and starting from Point 7, the reverse transformation takes place. It should be noted that while the forward transformation during cooling occurs first in front of the crack tip, the reverse transformation during heating starts from behind the crack tip where the stress levels are lower. At Point 8, the material Points far from the crack-tip start to reverse transform, but the majority of the specimen is still fully martensite. At Point 9, the martensitic region is only limited to the material point in front of the crack and at the other end of the specimen. At Point 10, fully austenitic regions begin to appear near boundaries of the specimen far from the crack. Majority of the specimen is reverse transformed to austenite

87

at Point 11 with transforming regions ahead of the crack. Finally, at Point 12, the entire specimen is fully austenite, except a confined zone at the crack tip with high stresses that eventually reverse transforms with further heating to higher temperatures.

5.5 Summary

Crack growth under actuation loading, i.e. thermal cycling under an applied bias load, is investigated in a disk-shaped compact tension model via 3D finite element analysis. The SMA model parameters are calibrated using uniaxial tensile experiments from a NiTiHf dog bone specimens. The virtual crack closure technique is implemented and crack is assumed to extend when the energy release rate reaches its critical value. It is shown that the choice of experimentally measured J_c fracture toughness results in simulations of the fracture response that agree quite well with the experimental data in terms of crack growth per actuation cycle and overall cycles to failure. In agreement with experimental observations, the crack is found to grow during cooling, when the material undergoes transformation from austenite to martensite. This is because of the increase in the crack tip energy release rate that has roots in the generated displacement associated with phase transformation. Evolution of transformation during actuation cycle revels that the forward transformation during cooling occurs first in front of the crack tip, while the reverse transformation during heating starts from behind the crack tip.

Figure 5.10: Evolution of martensite volume fraction (ξ) for an actuation crack growth cycle at points labeled in Figure 5.9 during cooling (points 1–6) and heating (points 7-12).

6.   UNIFICATION OF MECHANICAL AND ACTUATION CRACK GROWTH IN SMAS: THEORY AND EXPERIMENTATION

In this chapter, a unified methodology is proposed for fatigue crack growth in SMAs under two main loading paths, i.e. mechanical and actuation. The methodology is applied to understand the mechanisms contributing to crack growth in the presence of thermal and mechanical induced phase transformation in a Ni-rich NiTiHf high-temperature SMA under Mode-I loading. For mechanical crack growth, the specimen is subjected to cyclic loading at a constant temperature where the material undergoes forward transformation upon loading and reverse transformation upon unloading. For actuation crack growth, the specimen is subjected to thermal cycling under constant load between an upper cycle temperature and a lower cycle temperature ensuring complete forward transformation upon cooling and reverse transformation upon heating. The resistance of the material to crack growth under both loading paths is characterized by measuring the crack growth rates corresponding to the range of the applied driving force. The chapter is outlined as follows: Section 6.1 describes the proposed theory to unify mechanical and actuation fatigue crack growth. Section 6.2 describes the material system and explains the experimental procedure. The experimental results are presented and discussed in Section 6.3. The chapter concludes with a summary of key findings given in Section 6.4.

6.1   Theory

6.1.1   J-integral Approach to Fatigue Crack Growth

The objective of a fatigue crack growth experiment is to characterize the material's resistance to crack extension under cyclic loading by expressing the crack growth rate, da/dN, as a function of a correlating fracture parameter. The crack-tip stress intensity factor range, ΔK, defined by the linear elasticity, has been widely used in the engineering community as the correlating parameter. Paris and Erdogan [91] discovered that at intermediate ΔK values, the log-log plot of da/dN vs. ΔK is linear, and proposed the power-law equation for fatigue crack growth, widely known as the

Paris Equation

$$\frac{da}{dN} = C\Delta K^m, \tag{6.1}$$

where C and m are material constants that can be determined experimentally. ΔK is valid under small scale yielding (SSY) assumption, which can be violated if the plastic zone, or in general zone of non-linear deformation, close to the crack tip becomes comparable to the characteristic dimensions of the crack configuration. In such cases J-integral, introduced by Rice [86], can be applied to characterize the crack-tip conditions. It has been shown that the concept of J-integral can be extended to cyclic loading [92–96], and J-integral has been successfully implemented [97–99] to fit the crack growth rate data to a power-law expression in ΔJ

$$\frac{da}{dN} = C\Delta J^m. \tag{6.2}$$

In the linear elastic range ΔJ is related to ΔK through

$$\Delta J = \frac{(\Delta K)^2}{E'}, \tag{6.3}$$

where $E' = E$ for plane stress and $E' = E/(1 - \nu^2)$ for plain strain, and ν is the Poisson's ratio. Therefore, even in the linear elastic regime, ΔJ cannot be interpreted as the difference between maximum and minimum J-values, i.e. $\Delta J \neq J_{max} - J_{min}$. A more thorough discussion on this is provided in Appendix D. Moreover, it should be noted that J-integral is based on deformation plasticity, i.e. nonlinear elasticity, and when unloading occurs during cyclic loading, this theory can no longer model the material behavior. However, considering the loading half of a fatigue cycle, rather than the complete cycle, ΔJ is simply a generalization of J in which the initial load and displacement values are not necessarily zero. Therefore, similar to J, ΔJ can be inferred from the load vs. displacement curve.

As proposed in Ref [70], by dividing the displacement into an elastic and an inelastic part, i.e. $v = v^{el} + v^{in}$, J-integral can be calculated as the sum of the elastic and inelastic components

$$J = J^{el} + J^{in}$$

$$J = \frac{\eta^{el} A^{el}}{Bb} + \frac{\eta^{in} A^{in}}{Bb}, \tag{6.4}$$

where B is the specimen thickness and b is the length of the unbroken ligament, i.e. $b = W - a$ where W and a are the specimen width and crack size, respectively. A^{el} and A^{in} are the elastic and inelastic components of the area under the load–displacement curve, respectively. η^{el} and η^{in} are geometry-dependent factors [70, 71]. Extending Equation (6.4) for use in the loading half of fatigue cycle yields

$$\Delta J = \frac{\eta^{el} \Delta A^{el}}{Bb} + \frac{\eta^{in} \Delta A^{in}}{Bb}, \tag{6.5}$$

where the η factors adopt the same values as for monotonic loading. ΔA^{el} and ΔA^{in} are the elastic and inelastic components of the area under the load–displacement curve during the loading portion of a fatigue cycle, respectively. Following explains how Equation (6.5) can be employed to calculate ΔJ as the correlating parameter in mechanical and actuation fatigue crack growth in SMAs.

6.1.1.1 Mechanical Crack Growth

A mechanical fatigue crack growth experiment involves cyclic loading of a precracked specimen under an applied load with certain cycle frequency and waveform. The load–time and displacement–time curves during mechanical fatigue experiment are schematically shown in Figure 6.1a and Figure 6.1b, respectively. Note that the temperature is constant during the mechanical fatigue crack growth experiment (Figure 6.1c). If the loads and displacements have initial values P_{min} and v_{min}, and increase to P_{max} and v_{max}, per Figure 6.2a, ΔJ can be inferred using Equation (6.5) where ΔA^{el} and ΔA^{in} are evaluated as

$$\Delta A^{el} = \frac{1}{2}(P_{max} - P_{min})\Delta v^{el}, \tag{6.6}$$

and

$$\Delta A^{in} = \int_{v_{min}}^{v_{max}} (P - P_{min})dv - \Delta A^{el}. \tag{6.7}$$

92

In Equation (6.6), $\Delta v^{el} = C(P_{max} - P_{min})$ where C is the unloading elastic compliance obtained from the initial portion of the unloading part of a fatigue cycle. Note that if the load–displacement curve in Figure 6.2a is straight, i.e. the specimen behaves in a linear elastic manner, ΔJ can be calculated using Equation (6.3). In the case of SMAs, extra caution should be taken in selecting the E value because it assumes different values for austenite, self-accommodated, and oriented martensite. If SSY assumption is violated, i.e. significant deviation from linearity is observed in the load–displacement curve, using Equation (6.3) to calculate the elastic part may result in erroneous ΔJ values. In such cases, ΔJ should be calculated using Equation (6.5).

It is important to note that in the presence of crack closure effects, instead of the nominally applied ΔJ, an effective J-integral range, ΔJ_{eff}, should be determined for which P_{min} and v_{min} in Equations (6.6) and (6.7) are substituted with P_{op} and v_{op}, where P_{op} and v_{op} are the minimum load and displacement values at which the crack is open during loading, respectively. More details on determining ΔJ_{eff} is provided in Appendix D.

6.1.1.2 *Actuation Crack Growth*

An actuation fatigue crack growth experiment involves thermal cycling of a precracked specimen under a constant bias load. In such experiment, the temperature is cycled between a lower cycle temperature, LCT, and an upper cycle temperature, UCT, with a certain heating/cooling rate. The load–time and displacement–time curves during an actuation fatigue experiment is schematically shown in Figure 6.1d and Figure 6.1e, respectively. The key point to note is that although the load is constant, the displacement varies with cycling the temperature (Figure 6.1f) because of the phase transformation. It is worth mentioning that thermal expansion/contraction may also contribute to the displacement under actuation loading, but in much lesser degree compared to the phase transformation. Considering a single actuation cycle (Figure 6.2b), if the applied bias load is P_{bias}, at the beginning of cooling the displacement has initial value v_{min}, and increases to v_{max} at the end of cooling. ΔJ can be inferred using Equation (6.5) where ΔA^{el} and ΔA^{in} are evaluated as

$$\Delta A^{el} = \frac{1}{2} P_{bias} \Delta v^{el}, \tag{6.8}$$

and

$$\Delta A^{in} = P_{bias}(v_{max} - v_{min}) - \Delta A^{el}. \qquad (6.9)$$

In Equation 6.8, $\Delta v^{el} = CP_{bias}$. To distinguish between the elastic and inelastic components of the area under the load-displacement curve, the elastic compliance is needed. This can be measured with the aid of partial unloading/reloading sequences at the end of cooling during the actuation experiment. If the unloading/reloading sequence is performed at the end of heating even with the same crack size, specimen compliance may be different due to the elastic moduli mismatch between austenite and martensite phases.

It is important to note that the phase transformation may result in significant amount of non-proportional loading, and therefore path-dependency of J-integral. For a nonlinear material, the path-independence of J-integral holds when proportional loading occurs everywhere in the domain [49, 100]. It has been shown that similar to elastic-plastic materials, J-integral in SMAs subjected to mode-I mechanical loading exhibit path dependence [25, 49]. Moreover, the change in the material stiffness from austenite to martensite results in heterogeneity of the material domain. Because of this heterogenity induced by phase transformation the path-independence of J-integral can be violated. Assuming a fracture criterion based on J-integral can be justified if the path-dependency is small. Such an assumption can not be made for SMAs undergoing actuation loading. As a result, we will refer to ΔJ as ΔJ^* to acknowledge the possibility of violating its path-independency. Nevertheless, similar to ΔJ, ΔJ^* can be considered as a dissipation-based fracture criterion that accounts for the dissipation through phase transformation. Appendix E investigates the path-dependence of J-integral under both mechanical and actuation loading paths using finite element analysis (FEA). FEA results suggest a small amount of path-dependency under mechanical loading (a maximum of $\sim$10% difference between the crack-tip and far-field J values). Under actuation loading, however, the path-dependency is much more significant; the difference between the near-tip and far-field values is $\sim 50\%$ at the early stages of phase transformation and reaches as high as $\sim 270\%$ at the end of transformation.
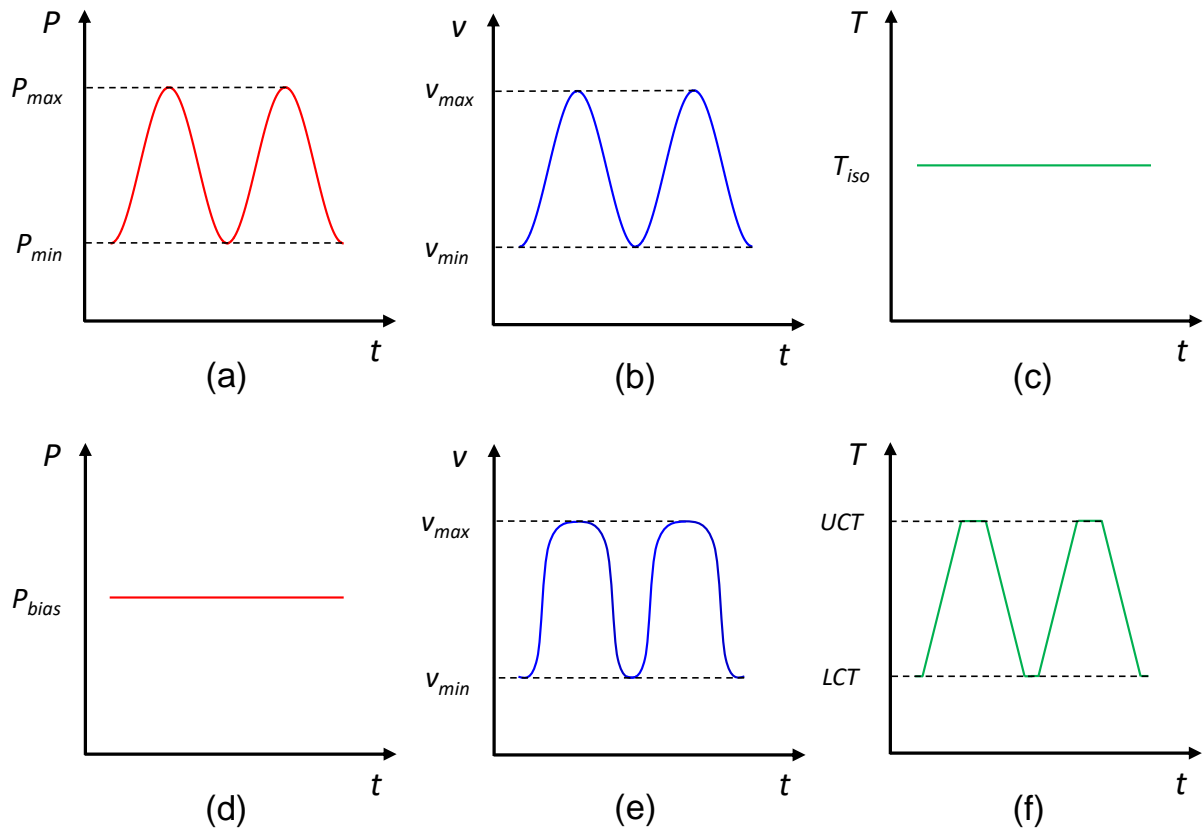
Figure 6.1: Variation of load P, displacement v, and temperature T with respect to time for a single mechanical cycle (a-c) and actuation cycle (d-f).
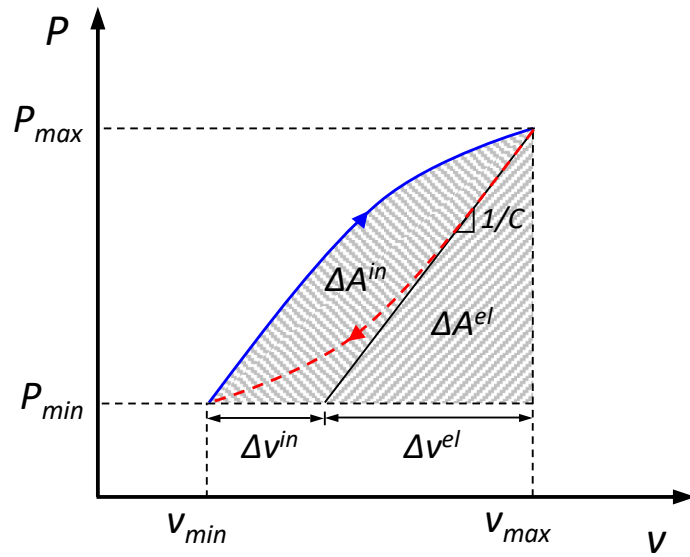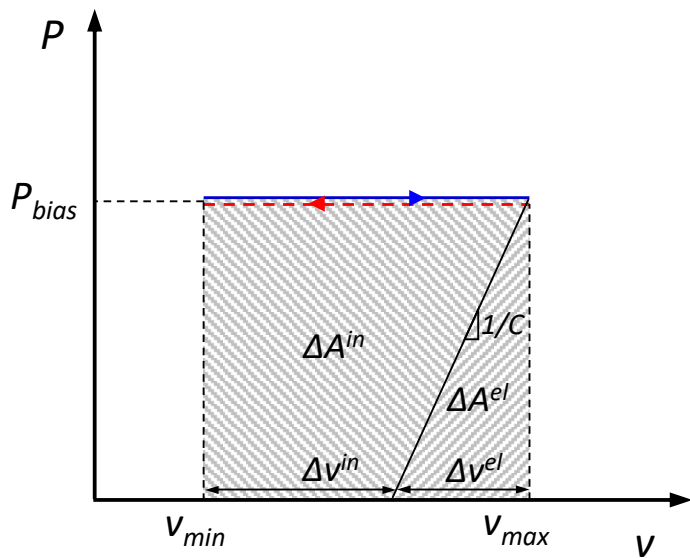
Figure 6.2: Load–displacement schematic illustrating the areas used in definition of cyclic J-integral for: (a) a mechanical loading cycle; (b) an actuation loading cycle.

6.2 Material and Methods

A hot extruded NiTiHf round bar with a nominal composition of $Ni_{50.3}Ti_{29.7}Hf_{20}$ (at. %) was acquired from ATI. The material was first solution heat treated at $900°C$ for one hour followed by water quenching to assure a single-phase structure. Subsequently, it was aged at $550°C$ for three hours followed by water quenching to tailor the precipitated microstructure and obtain the desired transformation temperature range.

Transformation temperatures at zero load were measured using a TA Instruments differential scanning calorimeter (DSC) with a heating/cooling rate of $10°C/min$ within 0–$300°C$ temperature range. The DSC curve is presented in Figure 6.3, from which the transformation temperatures are obtained from the intersection of tangent lines as $M_s = 135°C$, $M_f = 117°C$, $A_s = 149°C$, and $A_f = 162°C$, where M_s, M_f, A_s, and A_f denote martensite start, martensite finish, austenite start, and austenite finish temperatures, respectively. Based on these results, the temperature for mechanical experiments was selected as $180°C$, a temperature above A_f at which the material is expected to undergo stress-induced phase transformation upon loading, and reverse phase transformation upon unloading. For actuation experiments, LCT and UCT were selected as $50°C$ and $300°C$, respectively, to assure complete forward and reverse transformation.

Uniaxial tensile experiments were carried out using flat dog-bone-shaped specimens, machined by electrical discharge machining (EDM), on a servo-hydraulic MTS machine equipped with a high-temperature MTS extensometer. For the uniaxial mechanical experiment, the specimen was heated up to $180°C$, loaded to $\sim 2.5\%$ strain and then unloaded to zero load with an engineering strain rate of $1.5 \times 10^{-4} s^{-1}$. For the uniaxial actuation experiment, the specimen was heated up to UCT, loaded to a constant bias load corresponding to a uniaxial stress of 200 MPa, cooled down to LCT with a rate of $10°C/min$, and then heated up to UCT with the same rate. Heating and cooling were performed via thermal conduction from the grips and the temperature was measured using a K-type thermocouple directly attached to the gauge section of the dog-bone specimen.

For crack growth experiments, disk-shaped compact tension (DCT) specimens (Figure 6.4) were cut from the bar using EDM with their notch aligned in the radial direction. Both sides of
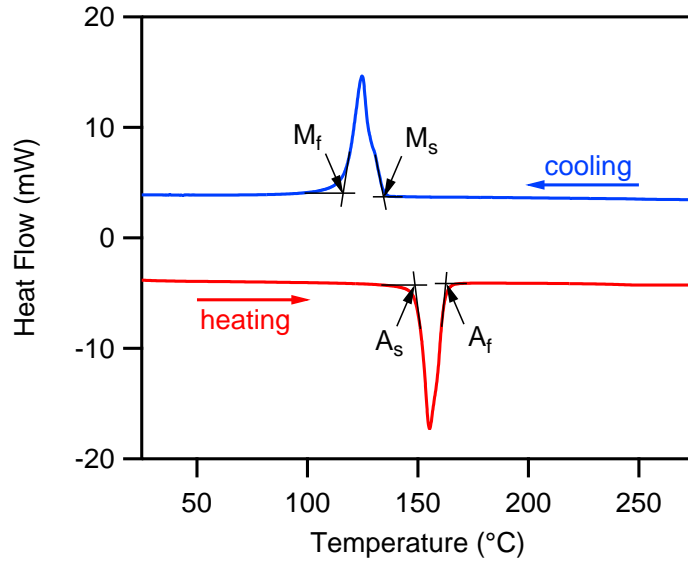
Figure 6.3: Differential scanning calorimetry of $Ni_{50.3}Ti_{29.7}Hf_{20}$ high temperature shape memory alloy. Transformation temperatures were measured from the intersection of tangent lines as $M_f = 117°C$, $M_s = 135°C$, $A_s = 149°C$, and $A_f = 162°C$.

the samples were prepared by mechanical grinding using abrasive papers to remove the machining oxides and for a better surface finish for optical crack size measurements. The samples were fatigue pre-cracked and tested using a servo-hydraulic MTS machine (MTS-810) equipped with a 10 kN load cell. Pre-cracking was performed at room temperature under cyclic loading with a sinusoidal waveform, at a frequency of 10 Hz and a constant load ratio, $R = P_{min}/P_{max} = 0.1$. During pre-cracking, the crack size was optically monitored from both sides of the specimen until the desired initial crack size (a_0) was obtained. For crack growth experiments, the temperature was monitored and controlled by averaging the readings from three K-type thermocouples, attached to different locations on the specimens. Specimens were heated via induction heating and cooled through assisted convection cooling. Crack month opening displacement (CMOD) was measured using an MTS COD gauge.

Mechanical crack growth was carried out at $180°C$, and in general accordance with the procedure described in ASTM E647 [101]. Similar to the pre-cracking, the fatigue crack growth ex-
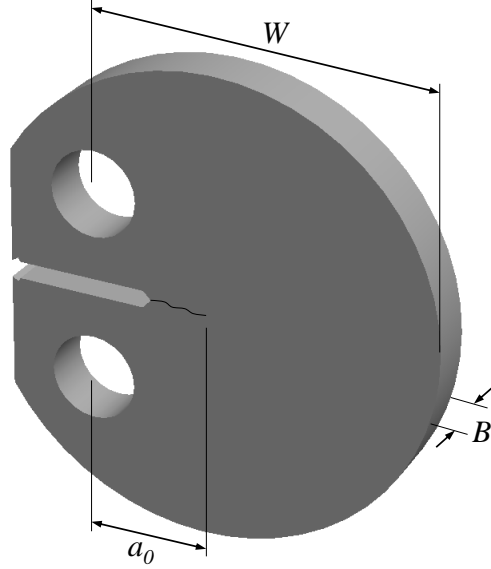
Figure 6.4: Geometry of NiTiHf disk-shaped compact tension (DCT) specimen for crack growth experiments with nominal dimensions of $W = 20$, $a_0 = 5$, $B = 3$, all in mm.

periment was conducted under load control where the specimen was mechanically cycled between P_{min} and P_{max} at 10 Hz, and using a constant load ratio, $R = 0.1$. To approach the threshold values, a load shedding scheme was adopted at a normalized K-gradient, $(1/K)dK/da$, of ~ -0.08 mm^{-1} . The load shedding scheme was started at crack growth rates below $\sim 10^{-8}$ m/cycle and continued until crack growth rates reached 10^{-10} m/cycle (the operational definition of threshold value). For fatigue crack growth rates above $\sim 10^{-8}$ m/cycle, constant load scheme was adopted and P_{min} and P_{max} were kept constant to move towards the unstable crack growth regime and ultimate fracture.

Crack size was monitored visually in situ from both sides of the specimen using two Point Grey Grasshopper GX-FW-60S6M-C CCD cameras equipped with Tokina AT-X Pro 100 mm f2.8 macro lenses, resulting in a resolution of 6 μm/pixel. At selected intervals, load was held constant at half of the applied maximum load during the preceding cycle and a pair of images were recorded, using which crack size was obtained as the average of the values measured from both sides. It is worth mentioning that because the specimens used in this study were relatively thin ($\sim$ 3mm), no

significant through-thickness variation of crack front is expected.

For actuation crack growth, the specimen was heated up to UCT ($300°$C) under zero load to fully transform the material into austenite, loaded to a constant bias load level, and then thermally cycled between UCT and LCT ($50°$C) with an average rate of $\sim 1.4°$C/s, with a 2 min dwell time at the end of each half cycle. Given the temperature range, $\Delta T = 250°$C, each actuation cycle took ~ 10 min to complete. Because the cycling frequency in an actuation crack growth experiments is orders of magnitude lower than that of a mechanical experiment, it is virtually impossible to run actuation experiments at loads that correspond to low ΔJ^* values. Consequently, the actuation experiment herein was performed at crack growth rates $\sim 5 \times 10^{-7}$ m/cycle and higher. Even at the aforementioned crack growth rates, generating data points under the constant load scheme becomes tedious. Therefore, load was increased systematically to approach the unstable crack growth regime and ultimate fracture. Partial unload/reloads were performed at the end of each half cycle to measure the specimen compliance, necessary to distinguish elastic and inelastic parts of the area under the load–displacement curve (Figure 6.2b).

6.3 Results and Discussion

6.3.1 Uniaxial Experiments

Figure 6.5a shows the uniaxial stress–strain curve for NiTiHf flat dog-bone specimen under mechanical loading at $180°$C. The specimen was loaded to ~ 2.5 % strain and then unloaded to zero load. According to the figure, upon loading, austenite deformed predominantly elastically at low stress levels with a Young's modulus E_A of ~ 90 GPa. When stress reached ~ 300MPa, the forward phase transformation started, and austenite transformed to stress-induced martensite. Upon unloading, the stress-induced martensite deformed predominantly elastically with a Young's modulus E_M of ~ 60 GPa before transforming back to asutenite. At the end of unloading, the specimen recovered the applied strain, and no transformation-induced plasticity (TRIP) was observed.

Figure 6.5b shows the uniaxial strain–temperature results for NiTiHf. The dog-bone specimen

was heated up to UCT, loaded to $\sigma = 200$ MPa, and then thermally cycled between UCT and LCT. According to the figure, upon cooling, the strain was decreased because of the thermal expansion of austenite until the temperature reached $\sim 155°C$, at which the temperature-induced forward transformation starts. The transformation strain generated at this stress level was measured to be ~ 3 %. After the transformation was finished, upon further cooling, a very small increase in strain was observed because of the negative thermal expansion coefficient of martensite [102,103]. Reheating the sample to UCT resulted in the reverse transformation to austenite. At the end of heating, no sign of TRIP was observed.

6.3.2 Mechanical Fatigue Experiment

The evolution of the crack size, a, with respect to the number of cycles, N, during the mechanical fatigue experiment of the NiTiHf DCT specimen at $180°C$ is presented in Figs. 6.6a and 6.6b for load shedding and constant load schemes, respectively, showing the typical crack growth trend for each scheme. Fatigue crack growth rates, da/dN were then determined from the data using the secant method which involves calculating the slope of the straight line connecting successive data points on the a vs. N curves, i.e. $da/dN = (a_{i+1} - a_i)/(N_{i+1} - N_i)$.

Figure 6.7 shows the load–displacement curves during constant load scheme of cyclic mechanical loading for NiTiHf DCT specimen. The curves correspond to the final cycle of last six completed 100-cycle intervals before failure. As the number of cycles were increased, crack growth resulted in an increase in the specimen compliance, and therefore the slope of the load–displacement curve decreased. Moreover, by increasing the number of cycles, the load–displacement response became more non-linear and the area of the hysteresis loop was increased. This can be explained by the increase in the size of the inelastic zone ahead of the crack tip. According to the figure, this deviation from linearity was very small. Note that these curves correspond to the final stages of fatigue crack growth before failure where the nonlinearity is expected to be most pronounced. Hence, in the specific case of the material in hand, ΔJ values are expected to be approximately equal to ΔJ^{el} because of the negligible contribution from the inelastic part, ΔJ^{in}. Consequently, ΔJ can be obtained using Equation (6.3). To investigate this, ΔJ values for the cycles in Fiq. 6.7
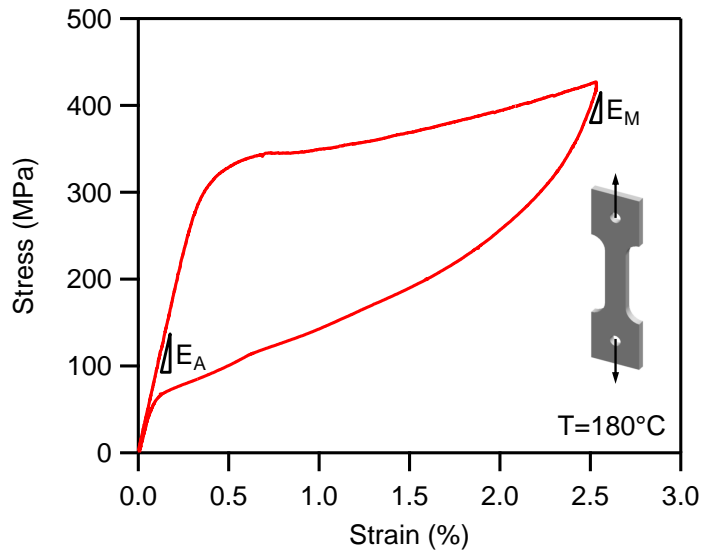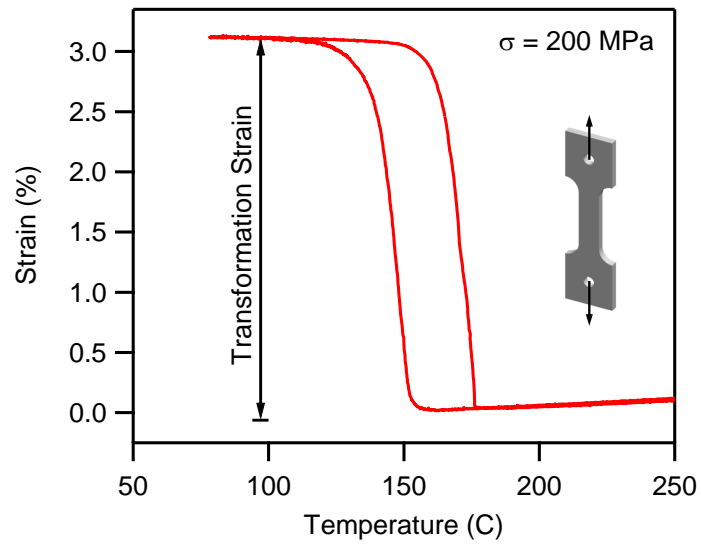
Figure 6.5: Uniaxial tensile test results for $Ni_{50.3}Ti_{29.7}Hf_{20}$ high temperature shape memory alloy: (a) mechanical loading at $T = 180°C$; (b) actuation loading at $\sigma = 200$ MPa.
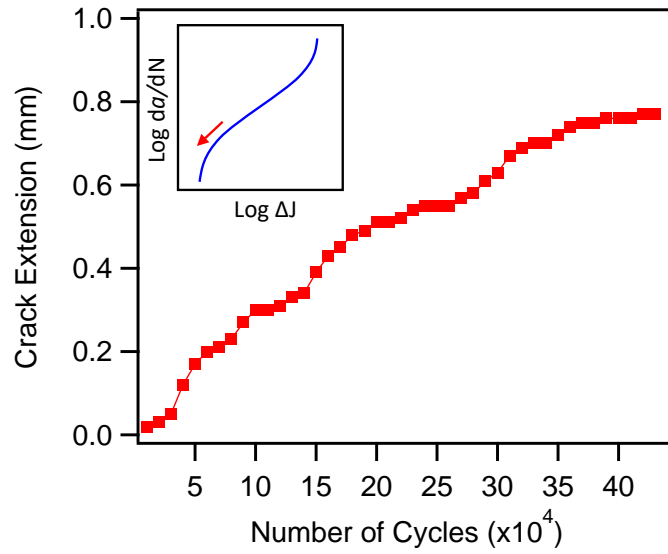
(a)
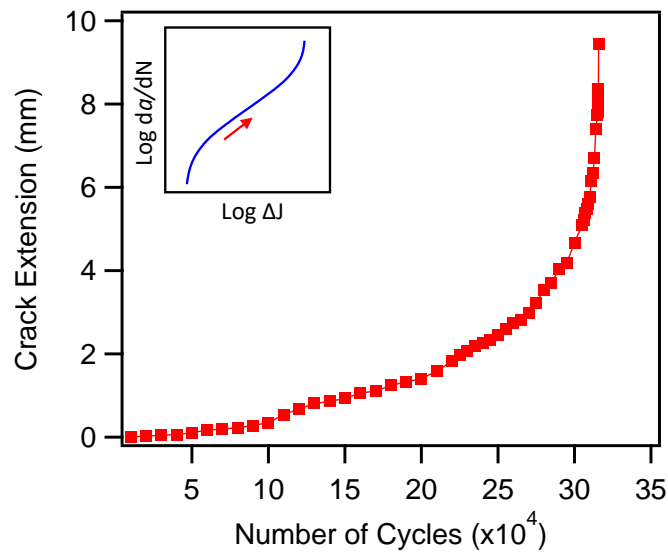
(b)

Figure 6.6: Evolution of the crack size, a, with respect to the number of cycles, N, during the mechanical fatigue experiment at 180°C: (a) load shedding scheme; (b) constant load scheme.

were calculated and compared using Eqs. (6.5) and (6.3), i.e. using the area under the load–displacement curve, and through the stress intensity factor range, respectively. For the former, the measured crack mouth displacement was converted to load line displacement following the procedure in Ref [80], and then was used together with the measured load values to find ΔJ from the elastic and inelastic areas under the load–displacement curves (Eqs. (6.6) and (6.7)). For the latter, $E' = E$ is assumed, and ΔK is calculated using $\Delta P = P_{max} - P_{min}$ as follows [30]

$$\Delta K = \frac{\Delta P}{B\sqrt{W}} \ f\left(\frac{a}{W}\right),$$
(6.10)

where $f(a/W)$ is a geometry-dependent shape function. For a DCT specimen

$$f\left(\frac{a}{W}\right) = \frac{2 + \left(\frac{a}{W}\right)\left[0.76 + 4.8\left(\frac{a}{W}\right) - 11.58\left(\frac{a}{W}\right)^2 + 11.43\left(\frac{a}{W}\right)^3 - 4.08\left(\frac{a}{W}\right)^4\right]}{\left(1 - \frac{a}{W}\right)^{\frac{3}{2}}}.$$
(6.11)

The results obtained from both methods are plotted in Figure 6.8. It can bee seen that by increasing the nonlinearity in the load–displacement response, the ΔJ values start deviating. However, since this deviation is insignificant, the variation between ΔJ values are very small (4-7 %).

Considering the insignificant nonlinearity in the load–displacement response, one may question the necessity of using ΔJ instead of ΔK as the correlating fracture parameter. First, this is the case for the material in this study. In general, SMAs can show significant nonlinearity in their load–displacement response [70]. Consequently, it is good practice to adopt a rigorous methodology that spans a wide range of material behavior, and is capable of taking into account the possible nonlinear effects. This is of great importance in SMAs for which the material response is extremely sensitive to the small variations in the composition and processing history [104]. Second, in the case of a linear response ΔJ is a modulus-normalized ΔK (Equation (6.3)). It has been shown [31, 105, 106] that the fatigue crack growth rates of a wide range of materials fall on a common curve when plotted against the modulus-normalised ΔK. Again, this is important in SMAs for which the elastic modulus assumes different values for austenite, self-accommodated, and ori-
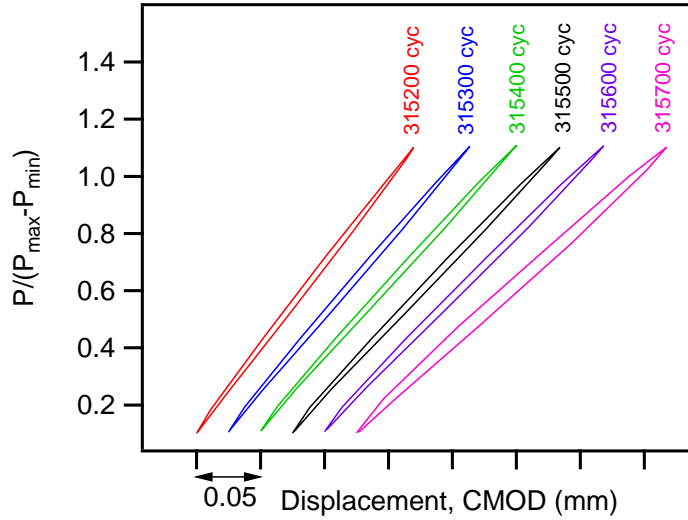
Figure 6.7: Load–displacement (CMOD) curves during constant load scheme of cyclic mechanical loading for NiTiHf DCT specimen at $180°$C, corresponding to the last cycle of six completed 100-cycle intervals before failure.

ented martensite. Finally, and more importantly, given that ΔK depends only on the applied load and crack configuration, as will be shown later in this chapter, using it as the correlating fracture parameter fails to interpreted the data from actuation crack growth experiments where the applied load is constant.

The mechanical fatigue crack growth behavior for NiTiHf DCT specimen at $180°$C with a frequency of 10 Hz and a load ration $R = 0.1$ is shown in Figure 6.9. The figure plots fatigue crack growth rate, da/dN, vs. the applied J-integral range, ΔJ, on the conventional log-log plot showing three typical stages of crack growth; Stage I: near threshold, Stage II: stable crack growth, and Stage III: unstable crack growth. The threshold J-integral range, ΔJ_{th}, was obtained from the the operational definition as ΔJ which corresponds to a fatigue crack growth rate of 10^{-10} m/cycle to be ~ 0.14 kJ/m^2. The steady-state regime of the mechanical fatigue crack growth was fitted with the Paris Equation (Equation (6.2)), and the coefficients, C and m, were measured to be 1×10^{-7} (m/cycle)/(kJ/m^2)^m and 2.2, respectively.

105
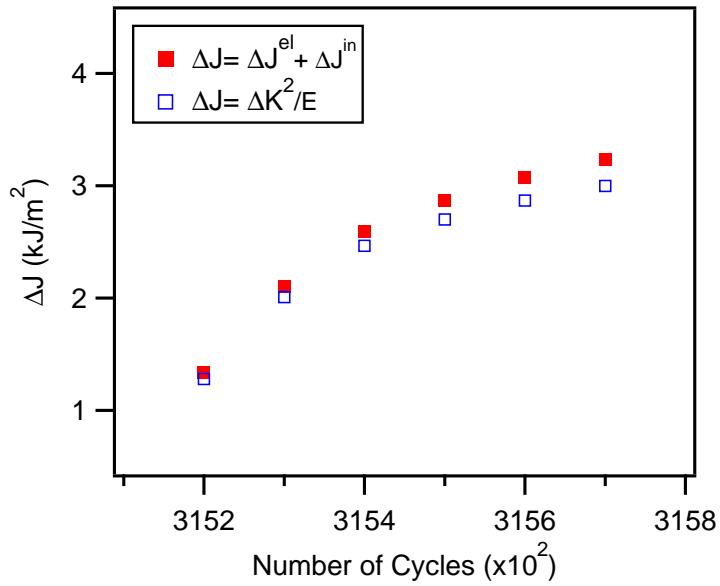
Figure 6.8: Comparison of the ΔJ values for the cycles in Figure. 6.7 obtained using the area under the load–displacement curve, and through ΔK.
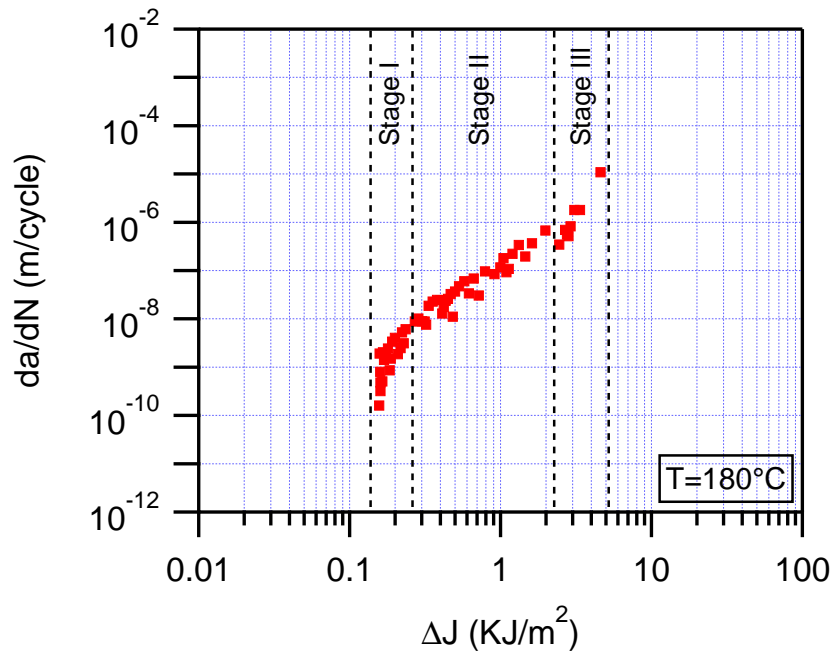
Figure 6.9: Crack growth rate, da/dN, vs. J-integral range, ΔJ, plot for mechanical fatigue crack growth of NiTiHf DCT specimen at $180°C$.
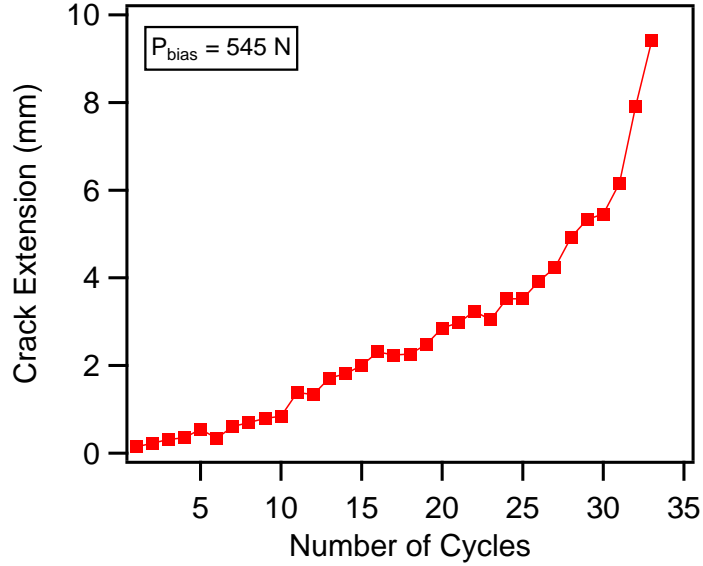
Figure 6.10: Evolution of the crack size, a, with respect to the number of cycles, N, during the actuation fatigue experiment ($P_{bias} = 545$ N).

6.3.3 Actuation Fatigue Experiment

The evolution of the crack size, a, with respect to the number of thermal cycles, N, during the actuation fatigue experiment of the NiTiHf DCT specimen at $P_{bias} = 545$ N is presented in Figure 6.10, showing a exponential-like crack growth trend similar to that of a constant load mechanical fatigue experiment. Crack growth was always occurred during cooling, i.e. during forward phase transformation, in agreement with previous observations [38,40]. As in the mechanical fatigue, the crack growth rates, da/dN were determined from the a vs. N data using the secant method.

Figure 6.11a shows the load–displacement curve for NiTiHf DCT specimen under actuation loading. Under an applied bias load, the displacement was increased during cooling, i.e. during forward phase transformation, giving rise to the area under the load–displacement curve, and hence ΔJ^*. This explains why the crack growth was observed during cooling. At the second half of the thermal cycle, the displacement was decreased during the subsequent heating when the reverse

phase transformation took place. The partial unload/reload sequence at the end of each half cycle was used to measure the specimen compliance, necessary to distinguish elastic and inelastic parts of the area under the load–displacement curve. To observe the evolution of the load–displacement curves with the number of cycles, the curves corresponding to the last six complete thermal cycles before failure are plotted in Figure 6.11b. It can be seen that as the number of cycles was increased, under the same applied load, crack growth resulted in an increase in the measured displacement values at both UCT and LCT. However, because the corresponding increase at LCT was larger compared to that of UCT, the overall area under the load–displacement curve was increased.

Figure 6.12a presents the displacement–temperature curve during 30th actuation cycle. According to the figure, upon cooling down from UCT, the displacement was almost constant with a very small decrease associated with the thermal expansion of austenite. Initiation of forward transformation resulted in a sudden increase in the measured displacement, and crack growth occurred. Subsequently, the displacement remained almost constant again without any further crack growth, however, this time it was slightly increased by cooling to LCT due to the negative thermal expansion of martensite. Upon heating, the reverse transformation took place and the displacement generated during forward transformation was mostly recovered. The displacement that was not recovered at the end of thermal cycle was mostly due to the crack extension, since TRIP was not observed in the uniaxial experiment (Figure 6.5b). The displacement–temperature plots corresponding to the last six complete thermal cycles before failure are shown in Figure 6.12b. As mentioned earlier, the measured displacement was increased with number of cycles. Moreover, the "transformation temperatures" was shifted to higher values as the number of cycles was increased. This can be attributed to a larger initial crack size from crack growth during previous cycle, and consequently higher stresses at the crack tip.

The actuation fatigue crack growth behavior for NiTiHf DCT specimen under both mechanical and actuation loading is shown in Figure 6.13. The figure plots crack growth rate, da/dN, versus ΔJ^*, on the conventional log-log plot. As mentioned previously because the cycling frequency in an actuation crack growth experiments is much lower than that of a mechanical experiment, it is
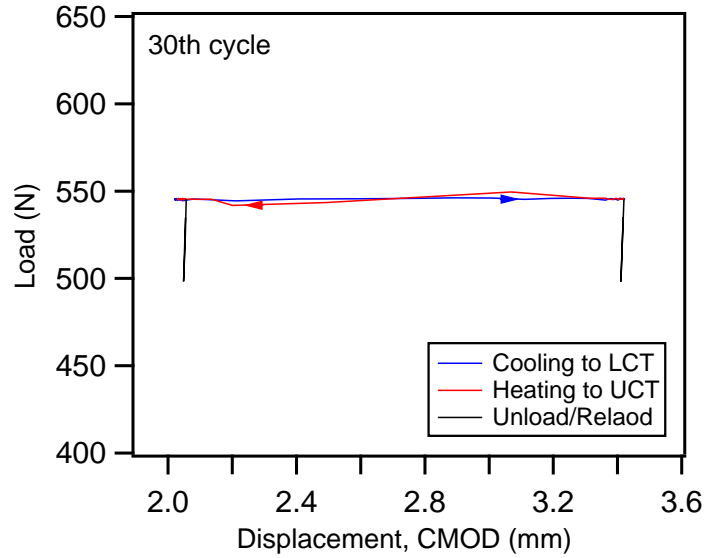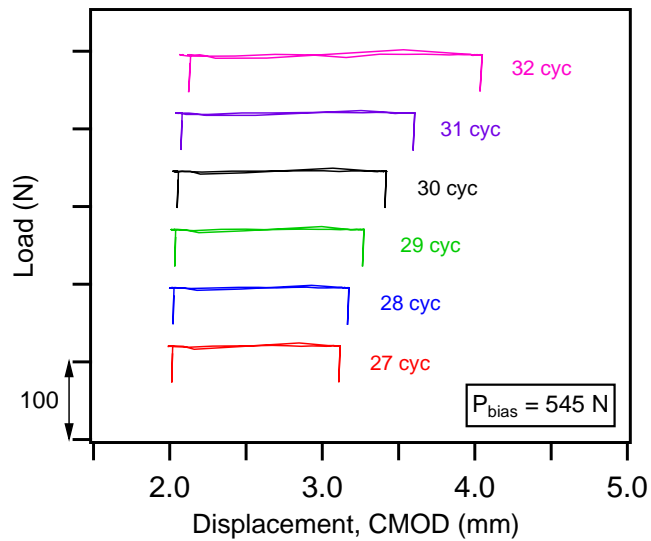
Figure 6.11: Load–displacement (CMOD) behavior during actuation fatigue crack growth experiment ($P_{bias} = 545$ N): (a) the 30th cycle showing the cooling, heating, and unload/reload sequences; (b) last six complete thermal cycles before failure.
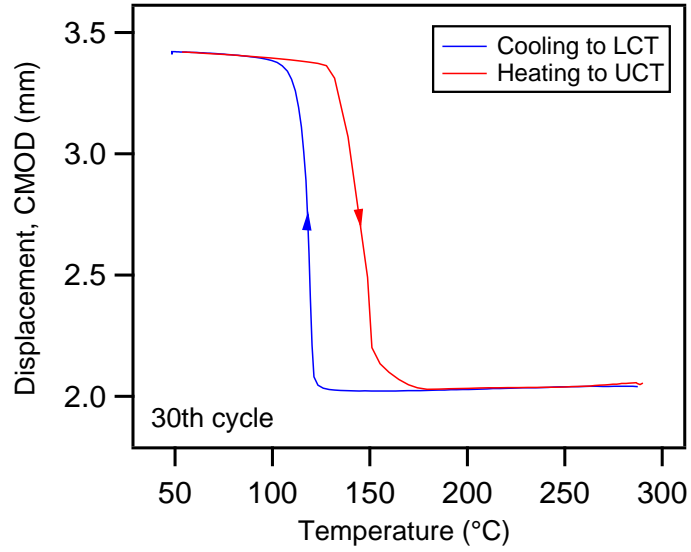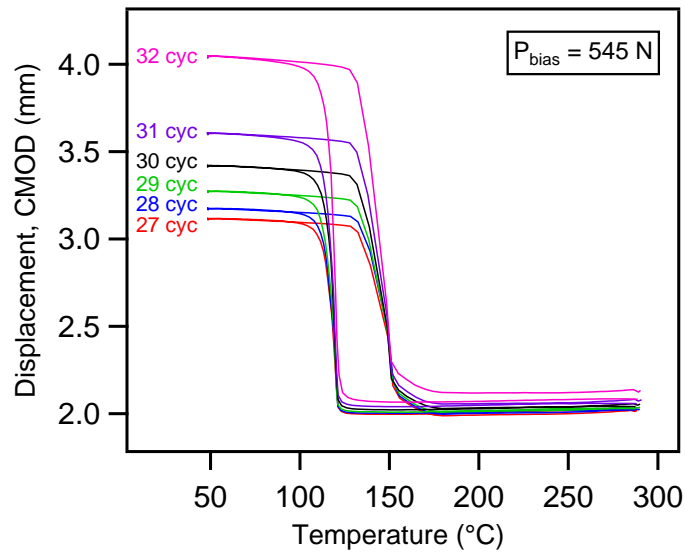
Figure 6.12: Displacement–temperature behavior during actuation fatigue crack growth experiment ($P_{bias} = 545$ N): (a) the 30th cycle showing the cooling to LCT and subsequent heating to UCT ; (b) last six complete thermal cycles before failure.

virtually impossible to run actuation experiments at loads that correspond to mechanically achievable ΔJ^* values, which emphasizes the importance and necessity of having a unified theory that can relate the two. Nevertheless, although limited in the applied ΔJ^*, the existing actuation crack growth results provide invaluable information. One important observation is that the actuation crack growth rates correlate well with the rates from steady-state regime of the mechanical crack growth. This is significant because as far as growth rate is concerned, this correlation could potentially eliminate the need to run actuation fatigue experiments since one may measure growth rates under mechanical loading instead. It should be noted that the crack growth rates under actuation loading seems to be slightly higher than those of mechanical loading in the steady-state regime. One possible explanation is that the crack growth rates under actuation loading does not correspond to the steady-state regime. Therefore, actuation crack growth data obtained at lower applied ΔJ^* values would be helpful in drawing a more detailed conclusion. Moreover, the selection of the testing temperature for the mechanical loading is important, and could be another reason for the crack growth rates being slightly different under actuation loading. As show in previous studies on mechanical fatigue crack growth of NiTi SMAs [20, 33, 37], the testing temperature can effect the growth rates considerably. In this study, the testing temperature was selected based on the transformation temperatures such that the material experiences forward and reverse transformation upon loading and unloading, respectively.

Another important observation from these results is that under actuation loading, the material can reach ΔJ^* values that are not achievable under mechanical loading. In other words, the material can actuate under ΔJ^* values that are higher than what the material can undergo without failure during mechanical cycling. One possible explanation is the effect of thermal expansion. Other than phase transformation, thermal expansion contributes to the displacement generated during thermal cycling. Given that in calculating ΔJ^* the area under the load–displacement curve is obtained using the displacement range, $\Delta v = v_{max} - v_{min}$, the displacement from thermal expansion is included but most probably doesn't contribute to the crack growth. However, the displacement from thermal expansion is very small compared to the displacement from the phase transforma-

tion, and hence the effect of thermal expansion, if any, can not be the main reason for the larger ΔJ^* values under actuation. The second reason is the possible difference in the temperature at which the crack growth occurs during mechanical and actuation loading. In the mechanical loading, the temperature is constant at $180°C$, i.e. above A_f. During actuation loading, the temperature varies, however, we know that the crack grows during forward phase transformation, which means at a temperature between M_s and M_f. Note that, the phase transformation temperatures depend on the applied stress, and because of the non-uniform stress distribution in a cracked specimen especially close to the crack tip, different material points will transform at different temperatures. Nevertheless, the temperature at which crack growth occurs may be different under mechanical and actuation loading, and therefore, resulting in different transformation toughening behavior. Finally, and more importantly, the reason is the effect of large scale phase transformation. Although in both mechanical and actuation experiments the material experiences forward and reverse transformation, the extent of phase transformation zone in the mechanical case is limited to the crack tip while in the actuation case the entire specimen undergoes phase transformation. Consequently, the specimen has the capacity to dissipate more energy through large-scale phase transformation.

For comparison purposes, and to emphasize the necessity of using a correlating parameter like ΔJ^* that accounts for transformation induced crack growth, the crack growth rates versus stress intensity factor range, ΔK, under mechanical and actuation loading paths are plotted in Figure 6.14. For the mechanical loading, ΔK values are calculated using Equation (6.10) while for the actuation loading, because the applied load is constant, ΔK values are calculated through the evolution of crack size. It can be seen that using ΔK as the correlating fracture parameter fails to interpreted the data from actuation crack growth experiment.

6.3.4 Crack Closure

The load–displacement curves in Figure 6.7 suggest little or no crack closure effect, indicated by a change in the slope of unloading curve, under mechanical fatigue crack growth at least for the testing temperature considered in this study. This is in agreement with the observation of Holtz et al. [20] where no crack closure effects were reported for NiTi SMA in the stress-induced
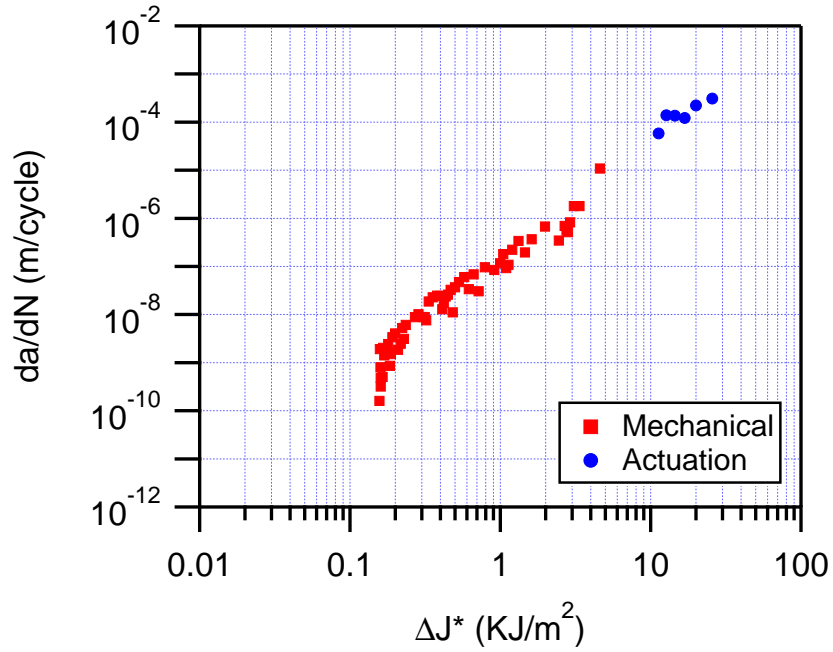
Figure 6.13: Crack growth rate, da/dN, versus ΔJ^*, plot for mechanical and actuation fatigue crack growth of NiTiHf DCT specimen.
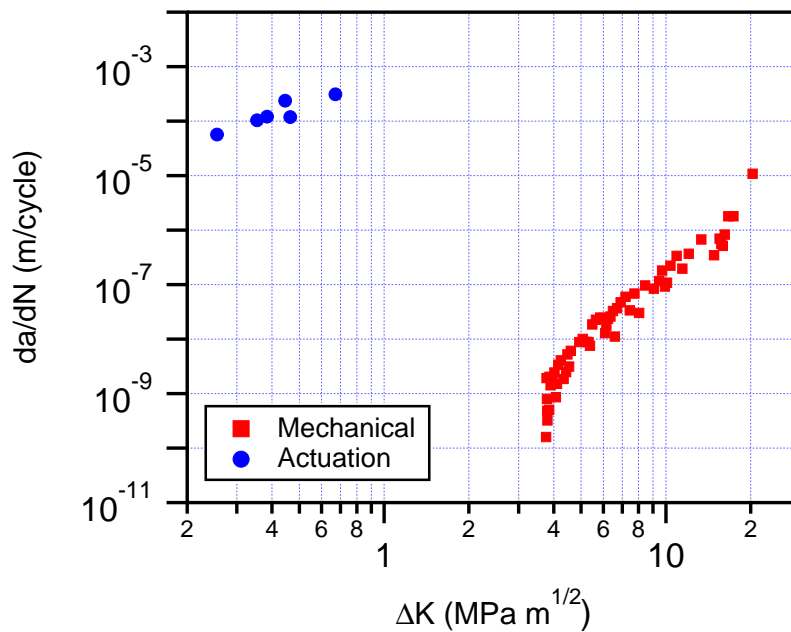
Figure 6.14: Crack growth rate, da/dN, versus ΔK, plot for mechanical and actuation fatigue crack growth of NiTiHf DCT specimen.

113

martensite regime. Assessing crack closure effects based on the load–displacement response is not feasible in the case of actuation crack growth experiment because the unload sequences were partial, and therefore could not give an indication of the presence of closure effects, if any. More rigorous methods such as compliance offset method [101] is required to investigate crack closure and determine the opening load and displacement, which is outside of the scope of this study.

6.4 Summary

A unified methodology is proposed for fatigue crack growth in SMAs under thermomechanical loading employing the range of J-integral as the driving force for crack growth. The methodology is applied to investigate crack growth in the presence of temperature and stress induced phase transformation in a Ni-rich NiTiHf high-temperature SMA under mode-I loading. For the mechanical crack growth, the specimen was subjected to cyclic loading at a constant temperature while for actuation crack growth, the specimen was subjected to thermal cycling under constant load. The resistance of the material to crack growth under both loading paths is characterized. Under mechanical loading, the threshold J-integral range, ΔJ_{th}, was obtained to be $\sim 0.14 \, \text{kJ/m}^2$, and the Paris exponent, m, was measured from steady-state regime to be ~ 2.2. The actuation crack growth rates correlated well with the rates of the mechanical crack growth. Moreover, under actuation loading, the material reached ΔJ^* values that were higher than those under mechanical loading. This is because the extent of phase transformation zone in the mechanical case was limited to the crack tip while in the actuation case the entire specimen underwent phase transformation, and consequently, the specimen had the capacity to dissipate more energy through large-scale phase transformation.

7. SUMMARY AND FUTURE WORK

7.1 Summary

Fracture toughness and crack growth behavior in NiTi and NiTiHf shape memory alloys (SMAs) were studied under various thermomechanical loading conditions. The developed methodologies alongside experimental measurements and finite element simulations enabled shedding light on some unanswered question regarding the transformation-induced complexities in fracture toughness measurement and crack growth evaluation of SMAs. Following provides a summary of key findings.

- The fracture toughness of a near-equiatomic NiTi was measured experimentally via a mechanics-aided test method using the J-integral as the fracture criterion. Isothermal fracture experiments were carried out on compact tension specimens at three distinct temperatures, below the martensite-finish temperature, between the martensite-start temperature and the martensite desist temperature, M_d, and above M_d. At these temperatures the material either remains in the martensite state throughout the loading (martensitic material) or transforms from austenite to martensite close to the crack tip (transforming material) or remains always in the austenite state (austenitic material), respectively. The fracture toughness values obtained result in extrapolated stress intensity factors that are about three times greater than the ones reported in literature. This discrepancy is due to the fact that the previously reported values were based on the assumption that the specimen response could be described by linear elasticity despite the fact that the zone of nonlinearity in those experiments was substantial. Moreover, according to the obtained results, the fracture toughness of martensitic and transforming materials was found to be approximately the same, most probably because in both cases the fracture toughness value measured corresponds to the fracture toughness of martensite close to the crack tip. The fracture toughness of stable austenite was found to be considerably higher.

- Crack growth behavior under mode-I isothermal loading and in the presence of stress-induced martensitic phase transformation is investigated in a compact tension model via 3D finite element analysis on the basis of a developed constitutive law. The virtual crack closure technique is implemented and crack is assumed to extend when the energy release rate at the crack tip reaches the material specific critical value. It is shown that the characterization of the material response from uniaxial experiments and the experimentally measured J_{Ic} fracture toughness result in simulations of the fracture response that agree quite well with the experimental data in terms of the load–displacement curve, near-tip strain distribution, and the size and shape of the stress-induced phase transformation zone at different stages of loading.

- Fracture behavior of a Ni-rich $Ni_{50.3}Ti_{29.7}Hf_{20}$ high-temperature shape memory alloy under mode-I isothermal loading was examined at three temperatures: $25°C$, $145°C$, and $180°C$. At these temperatures, self-accommodated martensite undergoes detwinning upon loading (martensitic material), austenite transforms to martensite during loading with no reverse transformation upon unloading (transforming materials), and austenite transforms to martensite during loading and transforms back to austenite upon unloading (superelastic material), respectively. Unstable crack growth was observed at all testing temperatures. The load–displacement curves were obtained and the critical J-integral values (J_c) were calculated. The specimens tested at $145°C$ showed the highest resistance to crack growth. This is because at this temperature the material at the crack-tip can transform at a relatively low stress value and therefore dissipate more energy through phase transformation compared to the specimens tested at $180°C$ where the transformation starts at a much higher stress value. The strain field on the surface and near the crack-tip was measured using DIC. Strain contour plots showed limited extent of dissipation mechanisms acting near the crack-tip at all testing temperatures.

- Crack growth under actuation loading, i.e. thermal cycling under an applied bias load, is

116

investigated in a disk-shaped compact tension model via 3D finite element analysis. The SMA model parameters are calibrated using uniaxial tensile experiments from a NiTiHf dog bone specimens. The virtual crack closure technique is implemented and crack is assumed to extend when the energy release rate reaches its critical value. It is shown that the choice of experimentally measured J_c fracture toughness results in simulations of the fracture response that agree quite well with the experimental data in terms of crack growth per actuation cycle and overall cycles to failure. In agreement with experimental observations, the crack is found to grow during cooling, when the material undergoes transformation from austenite to martensite. This is because of the increase in the crack tip energy release rate that has roots in the generated displacement associated with phase transformation. Evolution of transformation during actuation cycle revels that the forward transformation during cooling occurs first in front of the crack tip, while the reverse transformation during heating starts from behind the crack tip.

- A unified methodology is proposed for fatigue crack growth in SMAs under thermomechanical loading employing the range of J-integral as the driving force for crack growth. The methodology is applied to investigate crack growth in the presence of temperature and stress induced phase transformation in a Ni-rich NiTiHf high-temperature SMA under mode-I loading. For the mechanical crack growth, the specimen was subjected to cyclic loading at a constant temperature while for actuation crack growth, the specimen was subjected to thermal cycling under constant load. The resistance of the material to crack growth under both loading paths is characterized by measuring the crack growth rates, da/dN corresponding to the applied ΔJ^*. Under mechanical loading, the threshold J-integral range was obtained and the Paris exponent, m, was measured from steady-state regime. The actuation crack growth rates correlated well with the rates of the mechanical crack growth. Moreover, under actuation loading, the material reached ΔJ^* values that were higher than those under mechanical loading. This is because the extent of phase transformation zone in the mechanical case was limited to the crack tip while in the actuation case the entire specimen underwent

117

phase transformation, and consequently, the specimen had the capacity to dissipate more energy through large-scale phase transformation. transformation transformation transformation transformation transformation transformation

7.2 Future Work

Future experimental studies and modeling efforts that can expand the knowledge and understanding of fatigue and fracture in SMAs are discussed below.

- The results presented in this study focus on mode-I crack loading. This is the most common mode and hence very important in structural design and failure analysis. However, in SMA applications, e.g. torque tubes, the SMA component may experience a rather complex loading condition. Therefore, investigating other modes of loading, or even a combination of two or three modes (mixed-mode), remains to be implemented as a future work.

- The methods developed in this work use engineering fracture mechanics theories which are based on continuum mechanics. These theories are appropriate in situations where the crack size is large compared to the microstructural features. In smaller length scales, where the material cannot be considered to be a continuum domain, conventional driving forces based on LEFM or EPFM cannot be implemented to characterize the small cracks. Hence, developing micromechanics methods to investigate crack growth at the scale where individual grains and defects are considered is required.

- Although the effect of microstructure on constitutive response and phase transformation metrics is well established, its impact on crack growth characteristics and fracture properties of SMAs is yet to be systematically examined. Therefore, fracture of SMA material systems with the same composition but different microstructures resulting from various processing routes and heat treatments should be investigated.

- The effect of loading rate (mechanical or thermal) and the associated latent heat on crack growth behavior of SMAs should be examined. Latent heat generation/absorption has been

118

shown to alter the deformation response of SMAs, however, its influence on their fatigue and fracture properties is yet to be fully understood.

- Examining the fracture surfaces of SMAs suggests much less sensitivity of their fracture toughness to the specimen thickness. Therefore, the stringent thickness requirement for the materials that fail by void coalescence may be relaxed for SMAs where cleavage fracture prevails. The effect of thickness on fracture toughness of SMAs that aims to relax such requirements is currently under investigation.

REFERENCES

[1] D. Lagoudas, *Shape Memory Alloys: Modeling and Engineering Applications*. Springer US, 2008.

[2] K. Otsuka and C. M. Wayman, *Shape memory materials*. Cambridge university press, 1999.

[3] J. Cui, Y. S. Chu, O. O. Famodu, Y. Furuya, J. Hattrick-Simpers, R. D. James, A. Ludwig, S. Thienhaus, M. Wuttig, Z. Zhang, *et al.*, "Combinatorial search of thermoelastic shape-memory alloys with extremely small hysteresis width," *Nature materials*, vol. 5, no. 4, pp. 286–290, 2006.

[4] K. Melton and O. Mercier, "The mechanical properties of niti-based shape memory alloys," *Acta Metallurgica*, vol. 29, no. 2, pp. 393–398, 1981.

[5] S. A. Shabalovskaya, "On the nature of the biocompatibility and on medical applications of niti shape memory and superelastic alloys," *Bio-medical materials and engineering*, vol. 6, no. 4, pp. 267–289, 1996.

[6] M. Mohajeri, R. Case, B. Haghgouyan, D. C. Lagoudas, and H. Castaneda, "Loading influence on the corrosion assessment during stress-induced martensite reorientation in nickel-titanium sma," *Smart Materials and Structures*, vol. 29, no. 3, p. 035013, 2020.

[7] W. J. Buehler, J. Gilfrich, and R. Wiley, "Effect of low-temperature phase changes on the mechanical properties of alloys near composition tini," *Journal of applied physics*, vol. 34, no. 5, pp. 1475–1477, 1963.

[8] D. C. Lagoudas, O. K. Rediniotis, and M. M. Khan, "Applications of shape memory alloys to bioengineering and biomedical technology," in *Scattering Theory and Biomedical Engineering Modelling and Applications*, pp. 195–207, World Scientific, 2000.

[9] G. Song, N. Ma, and H.-N. Li, "Applications of shape memory alloys in civil structures," *Engineering structures*, vol. 28, no. 9, pp. 1266–1274, 2006.

[10] J. M. Jani, M. Leary, A. Subic, and M. A. Gibson, "A review of shape memory alloy research, applications and opportunities," *Materials & Design (1980-2015)*, vol. 56, pp. 1078–1113, 2014.

[11] D. J. Hartl and D. C. Lagoudas, "Aerospace applications of shape memory alloys," *Proceedings of the Institution of Mechanical Engineers, Part G: Journal of Aerospace Engineering*, vol. 221, no. 4, pp. 535–552, 2007.

[12] J. Ma, I. Karaman, and R. D. Noebe, "High temperature shape memory alloys," *International Materials Reviews*, vol. 55, no. 5, pp. 257–315, 2010.

[13] S. Robertson, A. Mehta, A. Pelton, and R. Ritchie, "Evolution of Crack-Tip Transformation Zones in Superelastic Nitinol Subjected to in situ Fatigue: A Fracture Mechanics and Synchrotron X-ray Microdiffraction Analysis," *Acta Materialia*, vol. 55, no. 18, pp. 6198–6207, 2007.

[14] S. Gollerthan, M. Young, A. Baruj, J. Frenzel, W. W. Schmahl, and G. Eggeler, "Fracture Mechanics and Microstructure in NiTi Shape Memory Alloys," *Acta Materialia*, vol. 57, no. 4, pp. 1015–1025, 2009.

[15] S. Gollerthan, M. Young, K. Neuking, U. Ramamurty, and G. Eggeler, "Direct Physical Evidence for the Back-Transformation of Stress-Induced Martensite in the Vicinity of Cracks in Pseudoelastic NiTi Shape Memory Alloys," *Acta Materialia*, vol. 57, no. 19, pp. 5892–5897, 2009.

[16] S. Daly, A. Miller, G. Ravichandran, and K. Bhattacharya, "An Experimental Investigation of Crack Initiation in Thin Sheets of Nitinol," *Acta Materialia*, vol. 55, no. 18, pp. 6322–6330, 2007.

[17] A. Creuziger, L. Bartol, K. Gall, and W. Crone, "Fracture in Single Crystal NiTi," *Journal of the Mechanics and Physics of Solids*, vol. 56, no. 9, pp. 2896–2905, 2008.

[18] T. Baxevanis and D. Lagoudas, "Fracture Mechanics of Shape Memory Alloys: Review and Perspectives," *International Journal of Fracture*, vol. 191, no. 1-2, pp. 191–213, 2015.

[19] S. Robertson, A. Pelton, and R. Ritchie, "Mechanical fatigue and fracture of nitinol," *International Materials Reviews*, vol. 57, no. 1, pp. 1–37, 2012.

[20] R. Holtz, K. Sadananda, and M. Imam, "Fatigue Thresholds of Ni-Ti Alloy Near the Shape Memory Transition Temperature," *International Journal of Fatigue*, vol. 21, pp. S137–S145, 1999.

[21] S. W. Robertson and R. O. Ritchie, "In Vitro Fatigue–Crack Growth and Fracture Toughness Behavior of Thin-Walled Superelastic Nitinol Tube for Endovascular Stents: A Basis for Defining the Effect of Crack-Like Defects," *Biomaterials*, vol. 28, no. 4, pp. 700–709, 2007.

[22] S. Robertson and R. Ritchie, "A fracture-mechanics-based approach to fracture control in biomedical devices manufactured from superelastic nitinol tube," *Journal of Biomedical Materials Research Part B: Applied Biomaterials*, vol. 84, no. 1, pp. 26–33, 2008.

[23] C. Maletta, E. Sgambitterra, and F. Furgiuele, "Crack tip Stress Distribution and Stress Intensity Factor in Shape Memory Alloys," *Fatigue & Fracture of Engineering Materials & Structures*, vol. 36, no. 9, pp. 903–912, 2013.

[24] C. Maletta, E. Sgambitterra, and F. Niccoli, "Temperature dependent fracture properties of shape memory alloys: novel findings and a comprehensive model," *Scientific reports*, vol. 6, no. 1, p. 17, 2016.

[25] B. Haghgouyan, N. Shafaghi, C. C. Aydıner, and G. Anlas, "Experimental and Computational Investigation of the Effect of Phase Transformation on Fracture Parameters of an SMA," *Smart Materials and Structures*, vol. 25, no. 7, p. 075010, 2016.

[26] J. Luo, J. He, X. Wan, T. Dong, Y. Cui, and X. Xiong, "Fracture properties of polycrystalline niti shape memory alloy," *Materials Science and Engineering: A*, vol. 653, pp. 122–128, 2016.

[27] B. Katanchi, N. Choupani, J. Khalil-Allafi, R. Tavangar, and M. Baghani, "Mixed-mode fracture of a superelastic niti alloy: Experimental and numerical investigations," *Engineering Fracture Mechanics*, 2017.

[28] R. Vaidyanathan, D. Dunand, and U. Ramamurty, "Fatigue crack-growth in shape-memory niti and niti–tic composites," *Materials Science and Engineering: A*, vol. 289, no. 1-2, pp. 208–216, 2000.

[29] A. Ahadi and Q. Sun, "Grain Size Dependence of Fracture Toughness and Crack-Growth Resistance of Superelastic NiTi," *Scripta Materialia*, vol. 113, pp. 171–175, 2016.

[30] ASTM-E399, "Standard Test Method for Linear-Elastic Plane-Strain Fracture Toughness K_{Ic} of Metallic Materials," tech. rep., ASTM International, West Conshohocken, PA, 2013.

[31] K. Melton and O. Mercier, "Fatigue of niti thermoelastic martensites," *Acta Metallurgica*, vol. 27, no. 1, pp. 137–144, 1979.

[32] A. McKelvey and R. Ritchie, "Fatigue-crack propagation in nitinol, a shape-memory and superelastic endovascular stent material," *Journal of Biomedical Materials Research: An Official Journal of The Society for Biomaterials, The Japanese Society for Biomaterials, and The Australian Society for Biomaterials and the Korean Society for Biomaterials*, vol. 47, no. 3, pp. 301–308, 1999.

[33] A. McKelvey and R. Ritchie, "Fatigue-crack growth behavior in the superelastic and shape-memory alloy nitinol," *Metallurgical and Materials Transactions A*, vol. 32, no. 3, pp. 731–743, 2001.

[34] K. Gall, J. Tyber, G. Wilkesanders, S. W. Robertson, R. O. Ritchie, and H. J. Maier, "Effect of microstructure on the fatigue of hot-rolled and cold-drawn niti shape memory alloys," *Materials Science and Engineering: A*, vol. 486, no. 1-2, pp. 389–403, 2008.

[35] W. S. LePage, A. Ahadi, W. C. Lenthe, Q.-P. Sun, T. M. Pollock, J. A. Shaw, and S. H. Daly, "Grain size effects on niti shape memory alloy fatigue crack growth," *Journal of Materials Research*, vol. 33, no. 2, pp. 91–107, 2018.

[36] E. Sgambitterra, C. Maletta, F. Furgiuele, and H. Sehitoglu, "Fatigue crack propagation in [0 1 2] niti single crystal alloy," *International Journal of Fatigue*, vol. 112, pp. 9–20, 2018.

[37] E. Sgambitterra, C. Maletta, P. Magarò, D. Renzo, F. Furgiuele, and H. Sehitoglu, "Effects of temperature on fatigue crack propagation in pseudoelastic niti shape memory alloys," *Shape Memory and Superelasticity*, vol. 5, no. 3, pp. 278–291, 2019.

[38] A. Iliopoulos, J. Steuben, T. Kirk, T. Baxevanis, J. Michopoulos, and D. Lagoudas, "Thermomechanical Failure Response of Notched NiTi Coupons," *International Journal of Solids and Structures*, vol. 125, pp. 265–275, 2017.

[39] C. Hayrettin, *Actuation fatigue and fracture of shape memory alloys*. PhD thesis, 2017.

[40] S. Jape, C. Hayrettin, , B. Young, B. Haghgouyan, T. Baxevanis, I. Karaman, and D. C. Lagoudas, "Actuation-induced stable crack growth in near-equiatomic nickel-titanium shape memory alloys: Experimental and numerical analysis," *Submitted*.

[41] S. Yi and S. Gao, "Fracture toughening mechanism of shape memory alloys due to martensite transformation," *International journal of solids and structures*, vol. 37, no. 38, pp. 5315–5327, 2000.

[42] S. Yi, S. Gao, and L. Shen, "Fracture toughening mechanism of shape memory alloys under mixed-mode loading due to martensite transformation," *International Journal of Solids and Structures*, vol. 38, no. 24-25, pp. 4463–4476, 2001.

[43] W. Yan, C. H. Wang, X. P. Zhang, and Y.-W. Mai, "Theoretical modelling of the effect of plasticity on reverse transformation in superelastic shape memory alloys," *Materials Science and Engineering: A*, vol. 354, no. 1-2, pp. 146–157, 2003.

[44] X. Wang, B. Xu, Z. Yue, and X. Tong, "Fracture behavior of the compact tension specimens in niti shape memory alloys," *Materials Science and Engineering: A*, vol. 485, no. 1-2, pp. 14–19, 2008.

[45] C. Maletta and F. Furgiuele, "Analytical modeling of stress-induced martensitic transformation in the crack tip region of nickel–titanium alloys," *Acta Materialia*, vol. 58, no. 1, pp. 92–101, 2010.

[46] C. Maletta and F. Furgiuele, "Fracture control parameters for niti based shape memory alloys," *International journal of solids and structures*, vol. 48, no. 11-12, pp. 1658–1664, 2011.

[47] C. Lexcellent, M. Laydi, and V. Taillebot, "Analytical prediction of the phase transformation onset zone at a crack tip of a shape memory alloy exhibiting asymmetry between tension and compression," *International journal of fracture*, vol. 169, no. 1, pp. 1–13, 2011.

[48] C. Maletta, "A novel fracture mechanics approach for shape memory alloys with trilinear stress–strain behavior," *International journal of fracture*, vol. 177, no. 1, pp. 39–51, 2012.

[49] T. Baxevanis, Y. Chemisky, and D. Lagoudas, "Finite Element Analysis of The Plane Strain Crack-tip Mechanical Fields in Pseudoelastic Shape Memory Alloys," *Smart Materials and Structures*, vol. 21, no. 9, p. 094012, 2012.

[50] T. Baxevanis and D. Lagoudas, "A Mode I Fracture Analysis of a Center-Cracked Infinite Shape Memory Alloy Plate Under Plane Stress," *International Journal of Fracture*, pp. 1–16, 2012.

[51] X. Wang, Y. Wang, A. Baruj, G. Eggeler, and Z. Yue, "On the Formation of Martensite in Front of Cracks in Pseudoelastic Shape Memory Alloys," *Materials Science and Engineering: A*, vol. 394, no. 1, pp. 393–398, 2005.

[52] A. Falvo, F. Furgiuele, A. Leonardi, and C. Maletta, "Stress-induced martensitic transformation in the crack tip region of a niti alloy," *Journal of materials engineering and performance*, vol. 18, no. 5-6, pp. 679–685, 2009.

[53] S. H. Ardakani, A. Afshar, and S. Mohammadi, "Numerical study of thermo-mechanical coupling effects on crack tip fields of mixed-mode fracture in pseudoelastic shape memory alloys," *International Journal of Solids and Structures*, vol. 81, pp. 160–178, 2016.

[54] T. Baxevanis, A. Parrinello, and D. Lagoudas, "On the Fracture Toughness Enhancement Due to Stress-Induced Phase Transformation in Shape Memory Alloys," *International Journal of Plasticity*, vol. 50, pp. 158–169, 2013.

[55] T. Baxevanis, C. M. Landis, and D. C. Lagoudas, "On the Effect of Latent Heat on the Fracture Toughness of Pseudoelastic Shape Memory Alloys," *Journal of Applied Mechanics*, vol. 81, no. 10, p. 101006, 2014.

[56] T. Baxevanis, A. Parrinello, and D. Lagoudas, "On the Driving Force for Crack Growth During Thermal Actuation of Shape Memory Alloys," *Journal of the Mechanics and Physics of Solids*, vol. 89, pp. 255–271, 2016.

[57] S. Jape, T. Baxevanis, and D. Lagoudas, "Stable Crack Growth During Thermal Actuation of Shape Memory Alloys," *Shape Memory and Superelasticity*, vol. 2, no. 1, pp. 104–113, 2016.

[58] S. Jape, T. Baxevanis, and D. Lagoudas, "On the Fracture Toughness and Stable Crack Growth in Shape Memory Alloy Actuators in the Presence of Transformation-Induced Plasticity," *International Journal of Fracture*, pp. 1–14, 2017.

[59] G. Stam and E. van der Giessen, "Effect of reversible phase transformations on crack growth," *Mechanics of materials*, vol. 21, no. 1, pp. 51–71, 1995.

[60] Y. Freed and L. Banks-Sills, "Crack Growth Resistance of Shape Memory Alloys by Means of a Cohesive Zone Model," *Journal of the Mechanics and Physics of Solids*, vol. 55, no. 10, pp. 2157–2180, 2007.

[61] T. Baxevanis, C. M. Landis, and D. C. Lagoudas, "On the Fracture Toughness of Pseudoelastic Shape Memory Alloys," *Journal of Applied Mechanics*, vol. 81, no. 4, p. 041005, 2014.

[62] S. Hazar, W. Zaki, Z. Moumni, and G. Anlas, "Modeling of Steady-State Crack Growth in Shape Memory Alloys Using a Stationary Method," *International Journal of Plasticity*, vol. 67, pp. 26–38, 2015.

[63] W. Yan, C. H. Wang, X. P. Zhang, and Y.-W. Mai, "Effect of transformation volume contraction on the toughness of superelastic shape memory alloys," *Smart materials and structures*, vol. 11, no. 6, p. 947, 2002.

[64] S. H. Ardakani, H. Ahmadian, and S. Mohammadi, "Thermo-mechanically coupled fracture analysis of shape memory alloys using the extended finite element method," *Smart Materials and Structures*, vol. 24, no. 4, p. 045031, 2015.

[65] M. Lu, F. Wang, X. Zeng, W. Chen, and J. Zhang, "Cohesive zone modeling for crack propagation in polycrystalline niti alloys using molecular dynamics," *Theoretical and Applied Fracture Mechanics*, vol. 105, p. 102402, 2020.

[66] F. Xiong and Y. Liu, "Effect of Stress-Induced Martensitic Transformation on the Crack Tip Stress-Intensity Factor in Ni–Mn–Ga Shape Memory Alloy," *Acta Materialia*, vol. 55, no. 16, pp. 5621–5629, 2007.

[67] C. Maletta and M. Young, "Stress-induced martensite in front of crack tips in niti shape memory alloys: modeling versus experiments," *Journal of materials engineering and performance*, vol. 20, no. 4-5, pp. 597–604, 2011.

[68] G. Özerim, G. Anlaş, and Z. Moumni, "On crack tip stress fields in pseudoelastic shape memory alloys," *International Journal of Fracture*, vol. 212, no. 2, pp. 205–217, 2018.

[69] Y. You, X. Gu, Y. Zhang, Z. Moumni, G. Anlaş, and W. Zhang, "Effect of thermomechanical coupling on stress-induced martensitic transformation around the crack tip of edge cracked shape memory alloy," *International Journal of Fracture*, pp. 1–11, 2019.

[70] B. Haghgouyan, C. Hayrettin, T. Baxevanis, I. Karaman, and D. C. Lagoudas, "Fracture toughness of niti–towards establishing standard test methods for phase transforming materials," *Acta Materialia*, vol. 162, pp. 226–238, 2019.

[71] ASTM-E1820, "Standard Test Method for Measurement of Fracture Toughness," tech. rep., ASTM International, West Conshohocken, PA, 2016.

[72] A. A. Griffith, "The Phenomena of Rupture and Flow in Solids," *Philosophical Transactions of the Royal Society of London. Series A, Containing Papers of a Mathematical or Physical Character*, vol. 221, pp. 163–198, 1921.

[73] G. R. Irwin, "Analysis of Stresses and Strains Near the End of a Crack Traversing a Plate," *Journal of Applied Mechanics*, vol. 24, no. 3, pp. 361–364, 1957.

[74] H. Ernst, P. Paris, and J. Landes, "Estimations on J-integral and Tearing Modulus T from a Single Specimen Test Record," in *Fracture Mechanics*, ASTM International, 1981.

[75] G. Clarke, W. Andrews, P. Paris, and D. Schmidt, "Single Specimen Tests for J_{Ic} Determination," in *Mechanics of Crack Growth*, ASTM International, 1976.

[76] J. Joyce and J. Gudas, "Computer Interactive J_{Ic} of Testing Navy Alloys," in *Elastic-Plastic Fracture*, ASTM International, 1979.

[77] ASTM-F2004, "Standard Test Method for Transformation Temperature of Nickel-Titanium Alloys by Thermal Analysis," tech. rep., ASTM International, West Conshohocken, PA, 2016.

[78] S. Miyazaki, K. Otsuka, and Y. Suzuki, "Transformation pseudoelasticity and deformation behavior in a ti-50.6 at% ni alloy," *Scripta Metallurgica*, vol. 15, no. 3, pp. 287–292, 1981.

[79] Y. Liu and S. Galvin, "Criteria for pseudoelasticity in near-equiatomic niti shape memory alloys," *Acta Materialia*, vol. 45, no. 11, pp. 4431–4439, 1997.

[80] J. Newman, "Stress-intensity factors and crack-opening displacements for round compact specimens," *International Journal of Fracture*, vol. 17, no. 6, pp. 567–578, 1981.

[81] H. Schreier, J. J. Orteu, and M. A. Sutton, *Image Correlation for Shape, Motion and Deformation Measurements*. Springer US, 2009.

[82] B. Haghgouyan, S. Jape, T. Baxevanis, I. Karaman, and D. C. Lagoudas, "Stable crack growth in niti shape memory alloys: 3d finite element modeling and experimental validation," *Smart Materials and Structures*, vol. 28, no. 6, p. 064001, 2019.

[83] D. Lagoudas, D. Hartl, Y. Chemisky, L. Machado, and P. Popov, "Constitutive model for the numerical analysis of phase transformation in polycrystalline shape memory alloys," *International Journal of Plasticity*, vol. 32, pp. 155–183, 2012.

[84] J. G. Boyd and D. C. Lagoudas, "A Thermodynamical Constitutive Model for Shape Memory Materials. Part I. The Monolithic Shape Memory Alloy," *International Journal of Plasticity*, vol. 12, no. 6, pp. 805–842, 1996.

[85] B. D. Coleman and W. Noll, "The thermodynamics of elastic materials with heat conduction and viscosity," *Archive for rational mechanics and analysis*, vol. 13, no. 1, pp. 167–178, 1963.

[86] J. R. Rice *et al.*, "A path Independent Integral and the Approximate Analysis of Strain Concentration by Notches and Cracks," ASME, 1968.

[87] O. Benafan, A. Garg, R. Noebe, G. Bigelow, S. Padula Ii, D. Gaydosh, N. Schell, J. Mabe, and R. Vaidyanathan, "Mechanical and functional behavior of a ni-rich ni50. 3ti29. 7hf20 high temperature shape memory alloy," *Intermetallics*, vol. 50, pp. 94–107, 2014.

[88] B. Young, B. Haghgouyan, D. Lagoudas, and I. Karaman, "Effect of temperature on the fracture toughness of a nitihf high temperature shape memory alloy," *Shape Memory and Superelasticity*, vol. 5, no. 4, pp. 362–373, 2019.

[89] K. Gall, N. Yang, H. Sehitoglu, and Y. I. Chumlyakov, "Fracture of precipitated niti shape memory alloys," *International journal of fracture*, vol. 109, no. 2, pp. 189–207, 2001.

[90] J. Makkar and T. Baxevanis, "Notes on the experimental measurement of fracture toughness of shape memory alloys," *Journal of Intelligent Material Systems and Structures*, p. 1045389X19888730, 2019.

[91] P. Paris and F. Erdogan, "A Critical Analysis of Crack Propagation Laws," *Journal of Basic Engineering*, vol. 85, pp. 528–533, 12 1963.

[92] H. Lamba, "The j-integral applied to cyclic loading," *Engineering Fracture Mechanics*, vol. 7, no. 4, pp. 693–703, 1975.

[93] C. Wüthrich, "The extension of the j-integral concept to fatigue cracks," *International Journal of fracture*, vol. 20, no. 2, pp. R35–R37, 1982.

[94] K. Tanaka, "The cyclicj-integral as a criterion for fatigue crack growth," *International Journal of Fracture*, vol. 22, no. 2, pp. 91–104, 1983.

[95] Y. Lambert, P. Saillard, and C. Bathias, "Application of the j concept to fatigue crack growth in large-scale yielding," in *Fracture mechanics: nineteenth symposium*, ASTM International, 1988.

[96] W. Ochensberger and O. Kolednik, "A new basis for the application of the j-integral for cyclically loaded cracks in elastic–plastic materials," *International Journal of Fracture*, vol. 189, no. 1, pp. 77–101, 2014.

[97] N. Dowling and J. Begley, "Fatigue crack growth during gross plasticity and the j-integral," in *Mechanics of crack growth*, ASTM International, 1976.

[98] N. E. Dowling, "Geometry effects and the j-integral approach to elastic-plastic fatigue crack growth," in *Cracks and fracture*, ASTM International, 1976.

[99] L. Banks-Sills and Y. Volpert, "Application of the cyclic j-integral to fatigue crack propagation of al 2024-t351," *Engineering fracture mechanics*, vol. 40, no. 2, pp. 355–370, 1991.

[100] D. Carka and C. M. Landis, "On the Path-Dependence of the J-integral Near a Stationary Crack in an Elastic-Plastic Material," *Journal of Applied Mechanics*, vol. 78, no. 1, p. 011006, 2011.

[101] ASTM-E647, "Standard Test Method for Measurement of Fatigue Crack Growth Rates," tech. rep., ASTM International, West Conshohocken, PA, 2015.

[102] J. Monroe, I. Karaman, D. Lagoudas, G. Bigelow, R. Noebe, and S. Padula II, "Determining recoverable and irrecoverable contributions to accumulated strain in a nitipd high-temperature shape memory alloy during thermomechanical cycling," *Scripta Materialia*, vol. 65, no. 2, pp. 123–126, 2011.

[103] A. Ahadi, Y. Matsushita, T. Sawaguchi, Q. Sun, and K. Tsuchiya, "Origin of zero and negative thermal expansion in severely-deformed superelastic niti alloy," *Acta Materialia*, vol. 124, pp. 79–92, 2017.

[104] O. Karakoc, C. Hayrettin, A. Evirgen, R. Santamarta, D. Canadinc, R. Wheeler, S. Wang, D. Lagoudas, and I. Karaman, "Role of microstructure on the actuation fatigue performance of ni-rich nitihf high temperature shape memory alloys," *Acta Materialia*, vol. 175, pp. 107–120, 2019.

[105] M. Speidel, "High temperature materials in gas turbines," *Elsevier Publishing Co., Amsterdam, New York and Oxford, 1974 p*, vol. 207, 1974.

[106] A. Ohta, N. Suzuki, and T. Mawari, "Effect of young's modulus on basic crack propagation properties near the fatigue threshold," *International journal of fatigue*, vol. 14, no. 4, pp. 224–226, 1992.

[107] H. Ernst, P. Paris, M. Rossow, and J. Hutchinson, "Analysis of Load-Displacement Relationship to Determine JR Curve and Tearing Instability Material Properties," in *Fracture Mechanics: Proceedings of the Eleventh National Symposium on Fracture Mechanics: Part I*, ASTM International, 1979.

[108] J. Merkle and H. Corten, "J integral Analysis for the Compact Specimen, Considering Axial Force as Well as Bending Effects," tech. rep., Oak Ridge National Lab., Tenn.(USA); Illinois Univ., Urbana (USA). Dept. of Theoretical and Applied Mechanics, 1973.

[109] P. C. Paris, H. Ernst, and C. Turner, "A J-integral Approach to Development of η-factors," in *Fracture Mechanics*, ASTM International, 1980.

[110] G. Clarke and J. Landes, "Evaluation of the J Integral for The Compact Specimen," *Journal of Testing and Evaluation*, vol. 7, no. 5, pp. 264–269, 1979.

[111] S. Kalidindi, A. Abusafieh, and E. El-Danaf, "Accurate characterization of machine compliance for simple compression testing," *Experimental mechanics*, vol. 37, no. 2, pp. 210–215, 1997.

[112] E. E. Gdoutos, *Fracture mechanics: an introduction*, vol. 123. Springer Science & Business Media, 2006.

[113] T. L. Anderson, *Fracture mechanics: fundamentals and applications*. CRC press, 2017.

[114] N. Louat, K. Sadananda, M. Duesbery, and A. Vasudevan, "A theoretical evaluation of crack closure," *Metallurgical Transactions A*, vol. 24, no. 10, pp. 2225–2232, 1993.

[115] D. Carka and C. M. Landis, "The analysis of crack tip fields in ferroelastic materials," *Smart materials and structures*, vol. 20, no. 9, p. 094005, 2011.

DETERMINATION OF THE GEOMETRY-DEPENDANT FACTORS*

For the following discussion, the alternative forms of the J-integral

$$J = \int_0^{P^*} \left(\frac{\partial \delta}{\partial a} \right)_{P^*} dP^* = - \int_0^{\delta} \left(\frac{\partial P^*}{\partial a} \right)_{\delta} d\delta \tag{A.1}$$

will be used, where P^* is the force per unit thickness and δ is the load point displacement. By dividing δ into an "elastic" and an "inelastic" part, $\delta = \delta^{el} + \delta^{in}$, the first form in Equation (A.1) yields

$$J = \underbrace{\int_0^{P^*} \left(\frac{\partial \delta^{el}}{\partial a} \right)_{P^*} dP^*}_{J^{el}} + \underbrace{\int_0^{P^*} \left(\frac{\partial \delta^{in}}{\partial a} \right)_{P^*} dP^*}_{J^{in}}. \tag{A.2}$$

A.1 η^{el} Factor

The elastic component of the load point displacement, δ_{el}, can be approximated as

$$\delta^{el} = C \cdot P^*, \tag{A.3}$$

where C is the elastic compliance of the fracture configuration during unloading and corresponds to a "frozen" microstructure with a mixture of phases. Thus,

$$J^{el} = - \int_0^{\delta^{el}} \left(\frac{\partial P^*}{\partial a} \right)_{\delta_{el}} d\delta^{el} = \frac{1}{C} \frac{\partial C}{\partial a} \frac{A^{el}}{B}, \tag{A.4}$$

where

$$\frac{A^{el}}{B} = \int_0^{\delta^{el}} P^* d\delta^{el}. \tag{A.5}$$

Thus,

$$J^{el} = \eta^{el} \frac{A^{el}}{Bb}, \tag{A.6}$$

where

$$\eta^{el} = \frac{b}{C} \frac{\partial C}{\partial a}. \tag{A.7}$$

Such an approximation of the elastic component of the J-integral essentially assumes that the part of the area under the load–displacement curve that corresponds to the change in the apparent elastic properties will be used in determining the inelastic component of the J-integral.

A.2 η^{in} Factor

Assuming that the transformation is confined to the remaining ligament, dimensional analysis [107] leads to

$$\frac{P^*}{W} = F^* \left(\frac{\delta^{in}}{W}, \frac{a}{W}, \frac{B}{W}, etc \right). \tag{A.8}$$

A more convenient for analysis equivalent form can be deduced using the unbroken ligament b and factoring out $(b/W)^2$

$$P^* = \frac{b^2}{W} F \left(\frac{\delta^{in}}{W}, \frac{a}{W}, \frac{B}{W}, etc \right). \tag{A.9}$$

Noting that $db = -da$ and using Eqs. (A.1) and (A.9)

$$J^{in} = \int_0^{P^*} \left(\frac{\partial \delta^{in}}{\partial a} \right)_{P^*} dP^* = -\int_0^{\delta^{in}} \left(\frac{\partial P^*}{\partial a} \right)_{\delta_{in}} d\delta^{in}$$

$$= \frac{2b}{W} \int_0^{\delta^{in}} F d\delta^{in} - \frac{b^2}{W^2} \int_0^{\delta^{in}} \frac{\partial F}{\partial \left(\frac{a}{W} \right)} d\delta^{in}. \tag{A.10}$$

Resubstituting for P^* from Equation (A.9)

$$J^{in} = \frac{2}{b} \int_0^{\delta^{in}} P^* d\delta^{in} - \frac{b^2}{W^2} \int_0^{\delta^{in}} \frac{\partial F}{\partial \left(\frac{a}{W} \right)} d\delta^{in}. \tag{A.11}$$

The first integral in the above equation is equal to A^{in}/B, and the second integral is the Merkle-Corten [108] term. Thus, there can be an η^{in} such that

$$J^{in} = \eta^{in} \frac{A^{in}}{Bb},$$

(A.12)

if and only if the Merkle-Corten term can be reduced to a A^{in} form. Such a requirement is fulfilled when the a/W and δ^{in}/W dependencies can be separated in F, *i.e.*,

$$F\left(\frac{\delta^{in}}{W}, \frac{a}{W}, etc\right) = G\left(\frac{\delta^{in}}{W}, etc\right) \cdot H\left(\frac{a}{W}, etc\right).$$

(A.13)

Under such conditions,

$$\int_0^{\delta^{in}} \frac{\partial F}{\partial \left(\frac{a}{W}\right)} d\delta^{in} = \frac{\partial H}{\partial \left(\frac{a}{W}\right)} \int_0^{\delta^{in}} G d\delta^{in} = \frac{\partial H}{\partial \left(\frac{a}{W}\right)} \frac{W}{b^2 H} \underbrace{\int_0^{\delta^{in}} P^* d\delta^{in}}_{A^{in}/B}.$$

(A.14)

Thus,

$$\eta^{in} = 2 - \frac{b}{W} \frac{\partial H}{\partial \left(\frac{a}{W}\right)} \frac{1}{H}.$$

(A.15)

It has been shown by Paris *et al.* [109] that a power hardening material, characterized by

$$\frac{\varepsilon}{\varepsilon_0} = \lambda \left(\frac{\sigma}{\sigma_0}\right)^N,$$

(A.16)

where λ is an arbitrary constant, satisfies the required condition for η^{in} existence. Since the phase transformation/orientation behavior is nearly linear, $N \to 1$, the method is practical for SMAs. The η^{in}-value for CT specimen is assumed to be given by the following expression

$$\eta^{in} = 2 + 0.522 \left(\frac{b}{W}\right).$$

(A.17)

This expression is the one proposed by Clarke and Landes [110] for the plastic η factor in the case of conventional ductile materials. Given that both transformation and plasticity are shear driven

135

processes and transformation contraction has a small influence on the overall fracture toughening enhancement in SMAs, such an approximation is considered to be valid. According to the theoretical analysis presented in [63], pure contraction of about 0.39%, a value that corresponds to NiTi [20], reduces the fracture toughness by 12% (with this value corresponding to steady state conditions), while numerical results under the assumption of volume preserving transformation predict fracture toughness enhancement order(s) of magnitude greater [54, 60, 61].

A.3 Determination of η^{el}

To calculate η^{el}, FEA is employed and the plane strain problem of a linear elastic CT specimen under isothermal mode-I loading is solved in Abaqus suite. The details of the calculation are briefly summarized below. The mesh consists of four-node bilinear plane strain quadrilateral elements (CPE4) and is refined as it approaches the crack tip where collapsed elements are used to account for the stress field singularity near the crack tip (Figure A.1). J-integral is evaluated using the integral method in Abaqus. To obtain a relation between η^{el} and specimen geometry, different crack sizes in the range $0.45 < a/W < 0.55$ were analyzed.

Figure A.2 shows the computational results for five different crack sizes. A linear relation is observed between J^{el} as computed from the domain integral technique and and A^{el}/Bb, where A^{el} is evaluated from the area under the load-displacement response for all crack sizes. The slope of the linear regression represents η^{el}. The values obtained for η^{el} for each crack size, plotted in Figure A.3 as a function of b/W, were used to derive the following equation

$$\eta^{el} = 1 + 3.25 \left(\frac{b}{W} \right). \tag{A.18}$$

A.4 Determination of γ^{el}

In view of Equation (A.3)

$$J^{el} = \eta^{el} \frac{1}{bC} \int_0^{\delta^{el}} \delta^{el} d\delta^{el}. \tag{A.19}$$
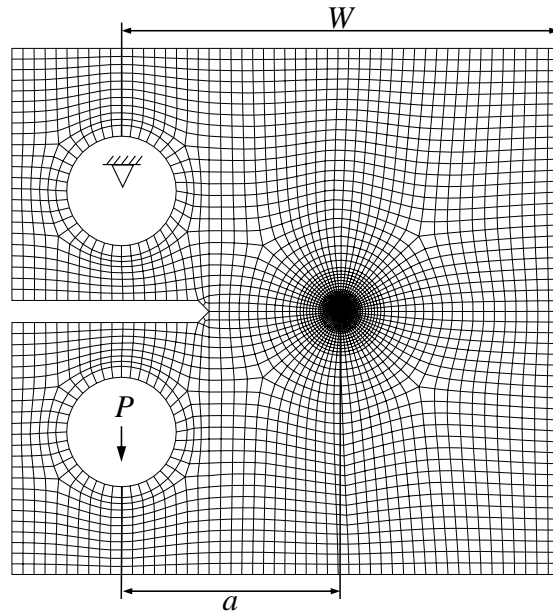
Figure A.1: Mesh geometry and boundary conditions of the CT model that is used for FEA.
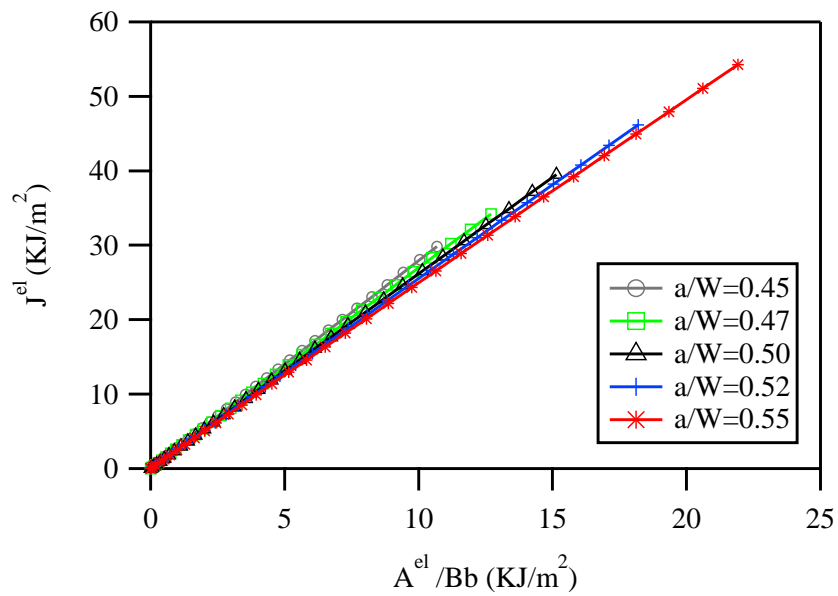
Figure A.2: J_{el} versus A_{el}/Bb plots for different crack sizes in the range $0.45 \leq a/W \leq 0.55$. The results are independent of the Young's modulus.
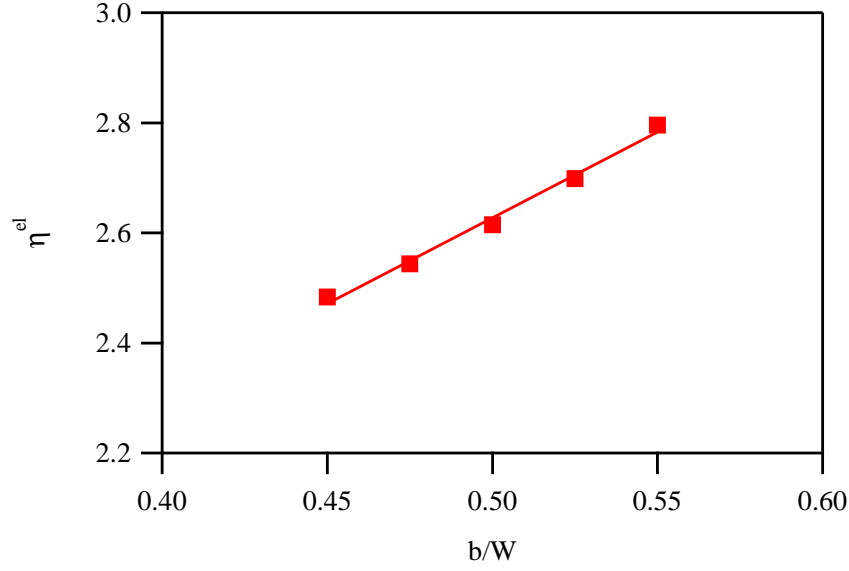
Figure A.3: η^{el} for crack sizes in the range $0.45 \leq a/W \leq 0.55$ ($b = W - a$).

Differentiation of Equation (A.19) yields

$$dJ^{el} = \left[-\left(\eta^{el} - 1 - \frac{b}{W} \frac{\left(\eta^{el}\right)'}{\eta^{el}} \right) \frac{\eta^{el}}{bC} \int_0^{\delta^{el}} G d\delta^{el} \right] da + \left(\eta_{el} \frac{1}{bC} \delta^{el} \right) d\delta^{el}, \qquad (A.20)$$

where $\left(\eta^{el}\right)' = d\eta^{el}/d(a/W)$. Reintegration results in

$$J^{el} = -\int_{a_0}^{a} \gamma^{el} \frac{J^{el}}{b} da + \int_0^{\delta^{el}} \eta^{el} \frac{1}{bC} \delta^{el} d\delta^{el}. \qquad (A.21)$$

Here γ^{el} is defined as

$$\gamma^{el} = \eta^{el} - 1 - \frac{b}{W} \frac{\left(\eta^{el}\right)'}{\eta^{el}}. \qquad (A.22)$$

Finally, plugging η^{el} from Equation (A.18) in Equation (A.22) gives

$$\gamma_i^{el} = 8.05 \left(\frac{b_i}{W} \right), \qquad (A.23)$$

138

Moreover, discretization of Equation (A.21) results in Equation (2.2).

A.5 Determination of γ^{in}

J^{in} can be written in view of Equation (A.13) as

$$J^{in} = \eta^{in} G \frac{b}{W} \int_0^{\delta^{in}} H d\delta^{in}. \tag{A.24}$$

Following the exact same procedure as for the determination of γ^{el}, the following expression can be obtained

$$J^{in} = -\int_{a_0}^{a} \gamma^{in} \frac{J^{in}}{b} da + \int_0^{\delta^{in}} \eta^{in} G \frac{b}{W} H d\delta^{in}, \tag{A.25}$$

where γ^{in} is defined as

$$\gamma^{in} = \eta^{in} - 1 - \frac{b}{W} \frac{(\eta^{in})'}{\eta^{in}}, \tag{A.26}$$

where $(\eta^{in})' = d\eta^{in}/d(a/W)$. In view of Equation (A.17), Equation (A.26) yields

$$\gamma_i^{in} = 1 + 0.76 \left(\frac{b_i}{W} \right), \tag{A.27}$$

and discretization of Equation (A.25) results in Equation (2.3).

APPENDIX B

CONVERSION OF DISPLACEMENT RECORDED BY THE ACTUATOR TO LOAD-LINE

DISPLACEMENT*

The displacement recorded from the actuator was converted to load-line displacement by first performing a correction for machine compliance to obtain the load-point displacement and then converting the load-point displacement to load-line displacement via the closed form expressions obtained by Newman [80].

The correction for machine compliance was based on the assumption that the specimen and the testing fixture can be modeled as a system in series, *i.e.*, the displacement recorded by the actuator was taken as the sum of the displacements in the sample and the loading system, while the load in both these components was assumed to be the same [111],

$$\delta_R = \delta_S^p + \delta_C, \tag{B.1}$$

where δ_R is the recorded displacement, δ_S^p is the specimen load-point displacement, and δ_C is the displacement in the loading system. If the machine compliance is idealized as a linear spring, then the above equation yields

$$C_m = \frac{\delta_R - \delta_S^p}{F}, \tag{B.2}$$

where $C_m = \frac{\delta_C}{F}$ is the machine compliance and F the applied load.

The machine compliance was measured from a single experiment by taking advantage of the above equation (Figure B.1). First, the load-line displacement as a function of applied load was measured by image processing using an in-house Matlab code. The load-line displacement was

---

	A_1	A_2	A_3	A_4	A_5
Load-point, A_i^p	1.905	-2.098	17.45	-25.66	16.55
Load-line, A_i^l	0.359	5.574	0.836	-8.271	9.521

Table B.1: Coefficients in the polynomial expressions of the load-point and load-line (crack surface) displacements for the rectangular CT geometry [80].

then converted to load-point displacement as follows

$$\delta_S^p = \delta_S^l \frac{\delta_S^p}{\delta_S^l} = \delta_S^l \, e^{\sum_{i=1}^{5} \left(A_i^p - A_i^l \right) (a/W)^{i-1}},$$
(B.3)

where δ_S^l is the specimen load-line displacement, A_i^p and A_i^l are the coefficients in the polynomial expressions of the load-point and load-line (crack surface) displacements, respectively, for the rectangular CT geometry obtained from the numerical simulations performed in [80], and are given in Table B.1.

Given the machine compliance C_m (Fig B.1), the displacement recorded by the actuator in all experiments performed is converted to the load-point displacement (Equation B.1) and subsequently to load-line displacement by inverting Equation B.2. Image processing to obtain the load-line for each load-displacement data point for all performed experiments could have been another but rather impractical option.
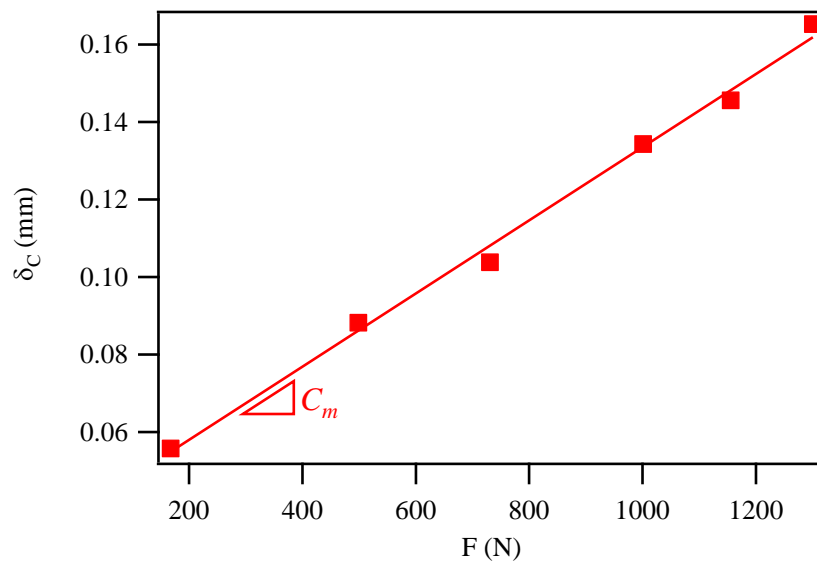
Figure B.1: Characterization of the machine compliance as a function of load.

APPENDIX C

EFFECT OF STRESS STATE IN 2D CRACKS

The boundary value problem is shown in Figure C.1, where displacement of the top hole is fixed (but rotation is allowed) while a vertical displacement is applied to the bottom hole to mimic the Mode-I experiment. Isothermal loading path is adopted at a temperature above M_s and below A_s. Due to the chosen initial temperature, the entire material only undergoes stress-induced forward phase transformation and no reverse transformation takes place at any material point. Consequently, the material is initially in austenitic state and upon isothermal loading will undergo forward transformation. A pre-crack represented by unbonded nodes is modeled that simulates the fatigue-induced pre-crack in a typical specimen. The ratio of the total crack size, a (notch-plus-pre-crack), to specimen width, W, is set to $a/W = 0.5$ and crack propagates along a predefined path. A finite element mesh of four-node, isoparametric, quadrilateral elements is used which is highly refined along the crack line to accurately capture the near-tip fields. Crack tip energy release rate is used as the driving force for crack growth and virtual crack closure technique (VCCT) is implemented. For the 2D four-node elements placed in the crack front, the energy release rate is computed as

$$G_I = -\frac{1}{2\Delta a}F_2^i(u_2^l - u_2^{l*}),\tag{C.1}$$

where F_2^i represent the nodal force at the crack tip and perpendicular to the crack plane, and u_2^l and u_2^{l*} indicate the opening displacement of the upper and lower crack surfaces, respectively.

Normalized von Mises equivalent stress, $\bar{\sigma}$, ahead of the crack-tip for plane strain and plane stress conditions prior to crack extension at an applied displacement of 0.5 mm is shown in Figure C.2. The stress is normalized by $E_A H_{sat}$, where E_A is the elastic modulus of austenite and H_{sat} is the maximum transformation strain, and the length parameter is normalized by initial length of the unbroken ligament, b_0. The stress distribution can be explained by considering three regions at the vicinity of crack-tip: a fully transformed region close to the tip, an untransformed region further
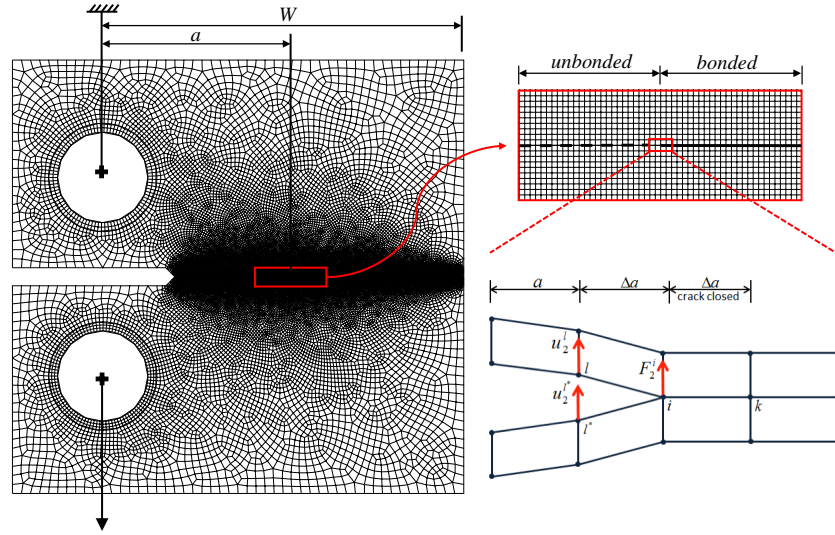
Figure C.1: FE boundary value problem, mesh geometry, and VCCT for four-node elements.

away from it, and a partially transformed region in between. Inside the untransformed austenite, stress increases as one approaches the crack tip. A plateau is observed in the partially transformed region which contains a mixture of the austenite and martensite phases. Stress increases abruptly within the fully transformed martensite in the region very close to the crack tip. The corresponding transformation zone boundaries are also included in the figure to better understand the role of stress-induced transformation. Although the overall variation of stress is similar, magnitude of the von Mises stress is higher under plane stress than that under plane strain.

The difference between plane strain and plane stress cases can be explained by the different maximum shear stress planes. Because the out of plane stress component is zero in plane stress, the maximum shear stress occurs in planes making $45°$ with the plane of the specimen (Figure C.3a). On the other hand, the maximum shear stress in plane strain occurs in planes normal to the plane of specimen making $45°$ with the crack plane (Figure C.3b). Consequently, the stress required to initiate transformation at a material point close to the crack-tip is higher in plane strain, giving rise to a smaller transformation zone than that in plane stress [112].
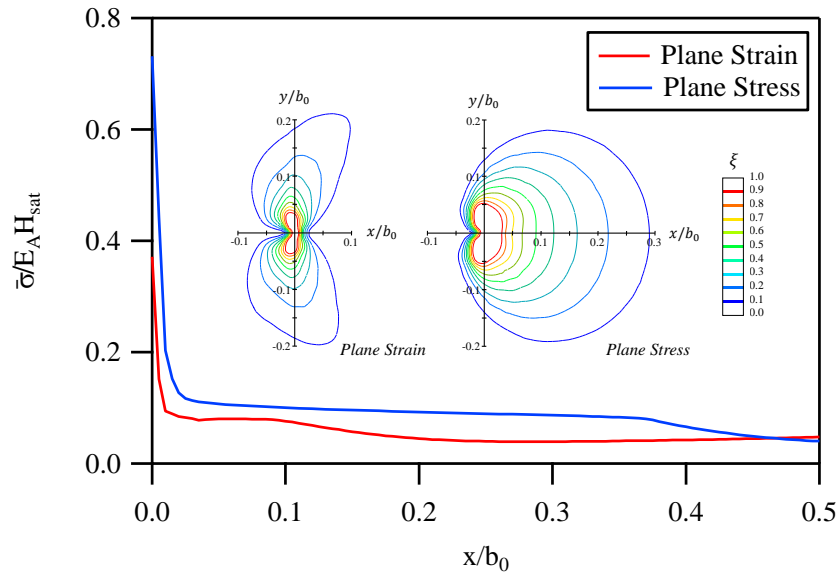
Figure C.2: Stress distribution near the crack tip of CT SMA model under plane strain and plane stress conditions at an applied displacement of 0.5 mm, along with the corresponding transformation zone boundaries.

(a)

(b)
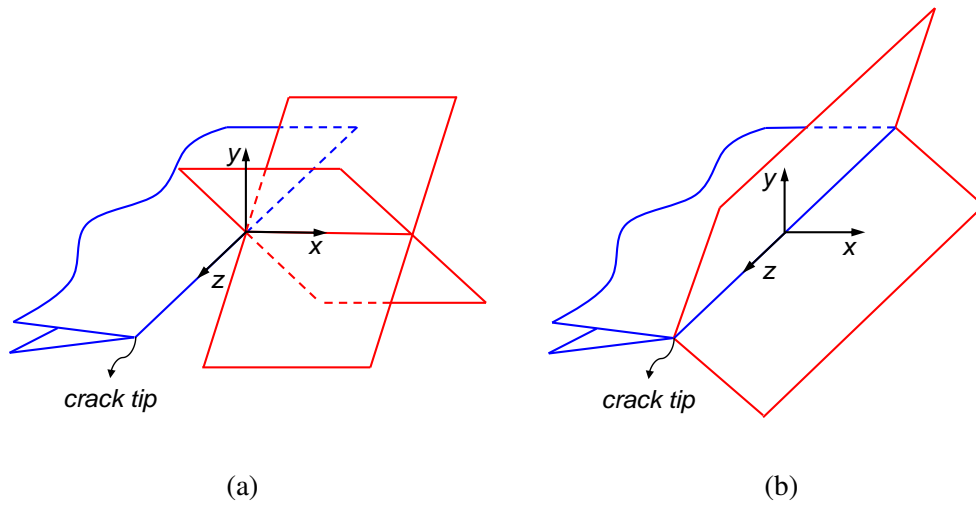
Figure C.3: Maximum shear stress planes in (a) plane stress, and (b) plane strain.

J-INTEGRAL RANGE

D.1 Variation of J-integral during Cyclic Loading

The J-integral under monotonic loading is defined as a path independent integral over an arbitrary contour surrounding the crack tip [86]

$$J = \int_{\Gamma} \left(w dy - T_i \frac{\partial u_i}{\partial x} ds \right),$$ (D.1)

where Γ is an arbitrary path around the crack tip, w is the strain energy density, T_i and u_i are the traction vector and the displacement vector, respectively, ds is the length increment along the contour, and x and y are the rectangular coordinates at the crack tip (see Figure D.1). The strain energy density is defined as

$$w = \int_0^{\varepsilon_{ij}} \sigma_{ij} d\varepsilon_{ij},$$ (D.2)

where σ_{ij} and ε_{ij} are the stress and strain tensors, respectively. The traction vector is given by

$$T_i = \sigma_{ij} n_j,$$ (D.3)

where n_j is the unit vector normal to Γ.

The ΔJ is an extension of the J-integral under cyclic loading. For the loading half of a fatigue cycle, ΔJ can be defined by [94]

$$\Delta J = \int_{\Gamma} \left[\Delta w dy - \Delta T_i \frac{\partial (\Delta u_i)}{\partial x} ds \right],$$ (D.4)

where $\Delta T_i = (T_i)_2 - (T_i)_1$, and $\Delta u_i = (u_i)_2 - (u_i)_1$ are the variations of T_i, and u_i between two loading states 1 and 2 corresponding to the beginning and end of a half cycle, respectively. Δw,
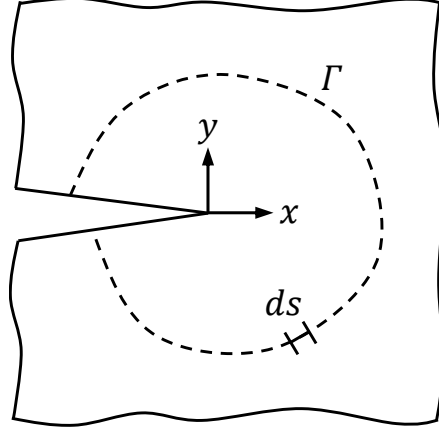
Figure D.1: Arbitrary contour around the tip of a crack used in the definition of J-integral.

the variation of stain energy density is defined as

$$\Delta w = \int_0^{\Delta\varepsilon_{ij}} \Delta\sigma_{ij}d(\Delta\varepsilon_{ij}), \tag{D.5}$$

where $\Delta\varepsilon_{ij} = (\varepsilon_{ij})_2 - (\varepsilon_{ij})_1$ and $\Delta\sigma_{ij} = (\sigma_{ij})_2 - (\sigma_{ij})_1$. Although ΔJ varies during cyclic loading, it is not equal to the variation, i.e. $\Delta J \neq J_2 - J_1$. This can be shown by developing Equation (D.6)

$$\Delta J = J_2 - J_1 - \int_\Gamma \left\{ (\sigma_{ij})_1\Delta\varepsilon_{ij}dy - (T_i)_2\frac{\partial(u_i)_1}{\partial x} + (T_i)_1\frac{\partial(u_i)_2}{\partial x} \right\} \tag{D.6}$$

D.2 Effective J-integral Range

Crack closure is a phenomenon where the faces of the crack contact during unloading part of a fatigue cycle at loads above the minimum applied load, causing the load to be transferred along the crack. During the subsequent loading, certain load needs to be applied to fully open the crack. This effect is more pronounced in crack growth under large-scale yielding conditions [113]. To take into account the effect of crack closure, an effective J-integral range, ΔJ_{eff}, can be defined
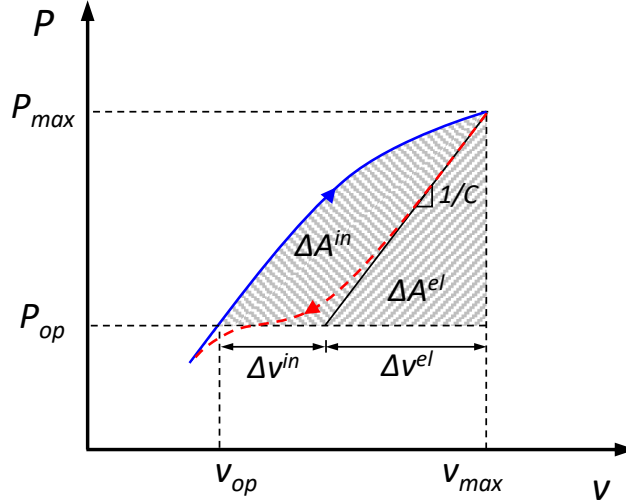
Figure D.2: Load–displacement schematic illustrating the areas used in definition of the effective J-integral range ΔJ_{eff} in the presence of crack closure effect.

as

$$\Delta J_{eff} = \frac{\eta^{el}\Delta A_{eff}^{el}}{Bb} + \frac{\eta^{in}\Delta A_{eff}^{in}}{Bb}, \tag{D.7}$$

where ΔA_{eff}^{el} and ΔA_{eff}^{in} are evaluated per Figure D.2 as

$$\Delta A_{eff}^{el} = \frac{1}{2}(P_{max} - P_{op})\Delta v^{el}, \tag{D.8}$$

and

$$\Delta A_{eff}^{in} = \int_{v_{op}}^{v_{max}} (P - P_{op})dv - \Delta A_{eff}^{el}, \tag{D.9}$$

where P_{op} and v_{op} are the minimum load and displacement values at which the crack is open during loading, respectively, and $\Delta v^{el} = C(P_{max} - P_{op})$. It is worth mentioning that the point at which the crack is closed during unloading is not necessarily equal to point at which it is open during loading [114]. Therefore, given that the closing load P_{cl} is less than the opening load P_{op}, determining ΔJ_{eff} from the closing point can result in an overestimation.

APPENDIX E

PATH-DEPENDENCE OF THE J-INTEGRAL

The path-dependence of the J-integral in shape memory alloys (SMAs) under mode-I loading is investigated using finite element analysis (FEA). To this aim, a two-dimensional (2D) disk-shaped compact tension (DCT) specimen with in plane dimensions identical to that of NiTiHf DCT specimens that was experimentally investigated in Chapter 4 is set up in Abaqus FEA suite. Displacement in the top pin hole is pinned (rotation is allowed) while load is applied in the vertical direction at the bottom pin hole. Figure E.1a shows the mesh geometry, in-plane dimensions, and applied boundary conditions. The material model described in Chapter 3 is implemented using a user-defined material subroutine (UMAT) while the model parameters given in Chapter 5 are adopted. Circular mesh is employed around a plane strain stationary crack as shown in Figure E.1b. J-integral values for 50 circular contours are computed using the domain integral method. Two thermomechanical loading paths are adopted: mechanical and actuation.

For the mechanical loading path, a load of $P = 500$ N is applied monotonically at $T = 180°$C, a temperature above A_f. For the specimen geometry considered here, this load approximates the maximum load that the NiTiHf DCT specimen investigated in Chapter 4 reached before the failure at the same temperature. The resulting load versus load point displacement response is shown in Figure E.2a. Five load levels are selected, as shown in the figure, for which the path-dependency of the J-integral is investigated. Figure E.2b shows the variation of the J-integral with different paths around the crack tip at the five different load levels. The J-integral values are normalized by the J value obtained from the outermost integral path, J_∞, while the radii of the circular paths, r, are normalized by the length of the remaining ligament, b. As shown in figure, the J-integral values are found to be contour dependent. Starting from the crack tip and moving outwards, the J-values first decrease and then increase to converge the far-field value. This behavior is consistent with previous studies on SMAs under mode-I mechanical loading [25,49]. For the contour approaching
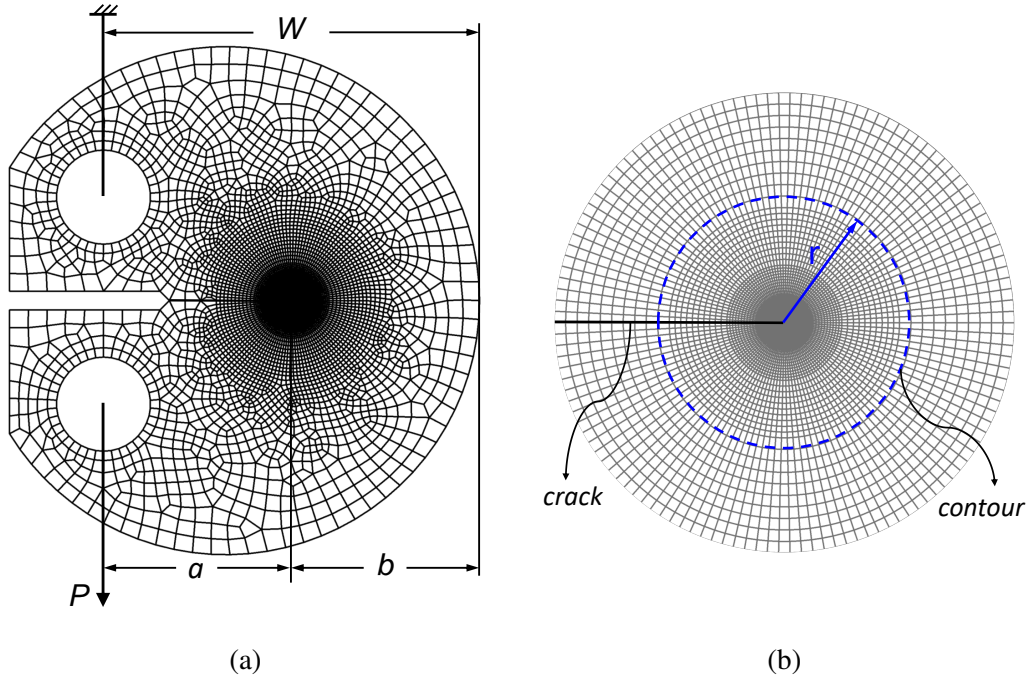
Figure E.1: Finite element boundary value problem and the mesh geometry of 2D DCT specimen with in plane dimensions: $W = 20$ mm, $a/W = 0.5$, $b/W = 0.5$. (b) Circular mesh around the stationary crack and the contours used to computed J values by domain integral method.

zero radius around the crack tip, J value is $\sim$10% higher than the far-field value at the highest applied load level. Considering the small difference between the crack-tip and far-field J-values, using J-integral as the fracture criterion can be justified for SMAs undergoing mechanical loading.

For the actuation loading path, a relatively lower load ($P = 200$ N) is applied at the same temperature, and then the temperature is decreased to $T = 80°$C, a temperature below M_f. The resulting load point displacement versus temperature response is shown in Figure E.2a. The path-dependency of the J-integral is investigated at five different points during cooling. These points correspond to the end of mechanical loading ($T = 180°$C), the beginning, half way through , and towards the end of phase transformation ($T = 135°$C, $T = 127°$C, and $T = 120°$C, respectively), and at the end of cooling ($T = 80°$C). Figure E.3b shows the variation of the J-integral with different paths around the crack tip at these five temperatures. Similar to the mechanical loading, the J-integral values are found to be contour dependent. Under actuation loading, however, the
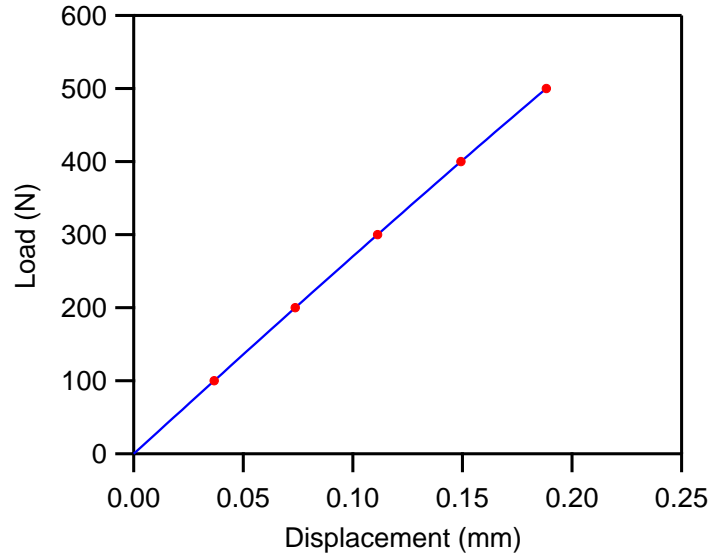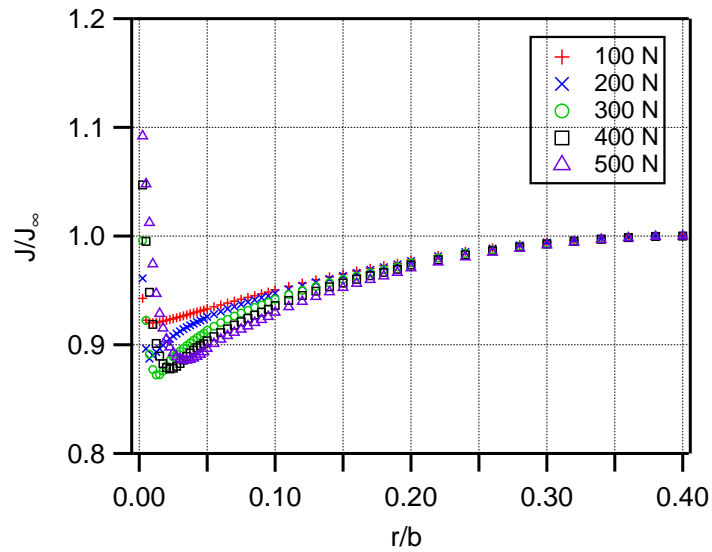
Figure E.2: (a) Load–displacement response for DCT model under mechanical loading. The selected data points correspond to different load levels for which the path-dependency of the J-integral is investigated. (b) Variation of the normalized J-integral with the normalized radius of the integration contour for different points along the load history.

initial drop in the J values before converging the far-field value is not evident. More importantly, the path-dependency is much more significant than the mechanical loading, i.e. the J values for the first contour around the crack tip are significantly larger than the far-field value. The increase in the near-tip J value is $\sim 50\%$ at the early stages of phase transformation ($T = 135°$C), and reaches as high as $\sim 270\%$ at the end of transformation.

As discussed in Refs. [100,115], the J-integral is expected to be path-dependent under in-plane loading and in situations where a significant amount of non-proportional loading occurs. In the case of SMAs, the heterogeneity of the material due to the phase transformation is also responsible. This explains the significant path-dependence observed under actuation loading where large scale transformation occurs compared to the mechanical loading where the transformation is limited to the crack tip.
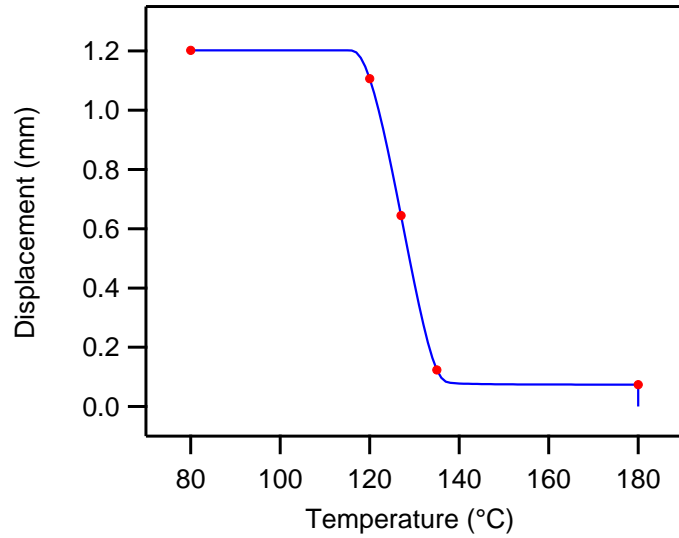
(a)
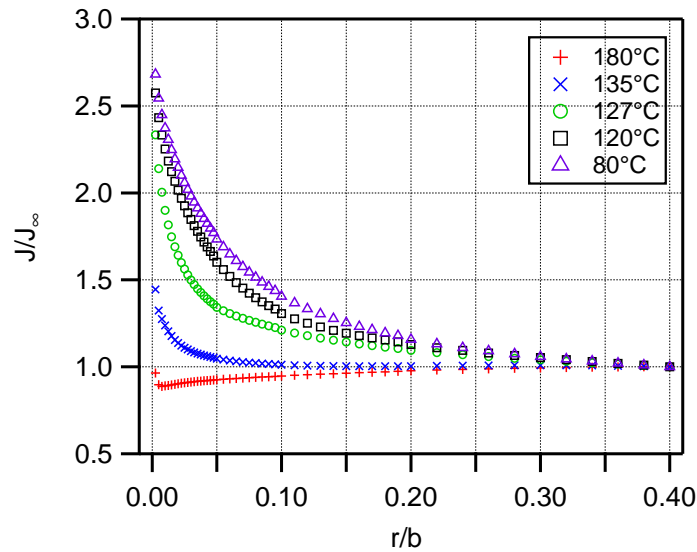
(b)

Figure E.3: (a) Displacement–temperature response for DCT model under actuation loading. The selected data points correspond to different temperatures for which the path-dependency of the J-integral is investigated. (b) Variation of the normalized J-integral with the normalized radius of the integration contour for different points along the load history.